Generalized Image Formation for Pulsed and

LFM-CW Synthetic Aperture Radar

Evan C. Zaugg

A dissertation submitted to the faculty of
Brigham Young University
in partial fulfillment of the requirements for the degree of

Doctor of Philosophy

David G. Long, Chair
Wynn C. Stirling
Karl F. Warnick
Dah-Jye Lee
Clark N. Taylor

Department of Electrical and Computer Engineering

Brigham Young University

April 2010

ABSTRACT

Generalized Image Formation for Pulsed and

LFM-CW Synthetic Aperture Radar

Evan C. Zaugg

Department of Electrical and Computer Engineering

Doctor of Philosophy

Approximations made in the traditional signal model for synthetic aperture radar (SAR) processing cause defocusing of the radar images when the system operates under conditions where the approximations lose validity. This dissertation investigates a number of these approximations and presents algorithmic improvements based on generalizations of the approxmations of the SAR signal model. These improvements result in better focused imagery from SAR systems with varied designs and parameters. Among the advancements presented is the development of a generalized chirp-scaling algorithm and a generalized frequency scaling algorithm to address the problems caused by approximations based on a Taylor series expansion of the SAR signal for both pulsed SAR and linear frequency modulated continuous wave (LFM-CW) SAR systems. These generalized algorithms extend the ability of frequency-domain algorithms to process SAR data from systems with a low frequency, a wide beamwidth, and a large bandwidth. Image formation algorithms are developed that account for the continuous platform motion and compensate for translational position errors due to the continuous non-ideal motion of real-world LFM-CW SAR systems, including a backprojection algorithm that does not rely upon the traditional stop-and-go approximation for platform motion.

ACKNOWLEDGMENTS

TABLE OF CONTENTS

LIST OF TABLES

LIST OF FIGURES

CHAPTER 1.   INTRODUCTION

Synthetic Aperture Radar (SAR) can produce high resolution imagery of a wide area using a small antenna and a large bandwidth. Taking advantage of the motion of the radar platform (usually an aircraft or spacecraft), a very large aperture is computationally synthesized using the data recorded from the radar echoes of a series of radar transmissions. This large synthetic aperture provides fine resolution in the direction of motion while a large bandwidth provides fine resolution in range.

SAR is a useful tool for a variety of civilian and military applications including terrain mapping, resource exploration, environmental monitoring, and intelligence, surveillance, and reconnaissance (ISR). To meet the needs of these different applications, a variety of SAR systems and processing methods have been developed. As SAR processing algorithms have been developed, certain assumptions and approximations have been made that match specific SAR scenarios (i.e., system parameters and/or requirements of the application). All SAR processing algorithms make approximations; the more general algorithms make fewer assumptions and are applicable in more circumstances, often at the cost of an increased processing load. For many SAR processing algorithms, the assumptions and approximations may be invalidated if the data is collected from a SAR system that is operating with very different parameters, such as frequency, bandwidth, beamwidth, squint, platform, or range. The approximations can also be invalidated if the data is collected on a different platform or if the data is intended to be used for a different application. Attempting to use a specialized algorithm when the approximations are not valid can result in degraded performance or even failure to produce an image.

In this dissertation, generalizations of existing SAR processing theory are developed for efficiently producing high-quality SAR imagery while reducing the harmful effects of algorithmic approximations. One common approximation is a low-order Taylor series expansion

of the SAR signal model in the frequency domain. This approximation is valid for a limited range of frequencies, beamwidths, and squint angles. Another common approximation is the stop-and-go platform motion model, which is invalid for continuous wave systems that are continuously transmitting and receiving. The research in this dissertation addresses these issues.

To better understand previous SAR processing developments, and how this research fits into the big picture, a short history of major processing milestones is given in this chapter. The first SAR processing was done optically. The processing system was precisely designed to work with a single SAR system operating at a single set of SAR parameters. During data collection, the radar signal returns modulated the intensity of a line-scan cathode-ray tube (CRT). The output of the CRT was imaged through a lens onto a moving filmstrip. After the flight, the film was developed and laser light was shone through the film and focused through a spherical lens, forming the focused image at the focal plane. The physical lens had to be manufactured matched to the radar and the flight parameters, including one particular along-track pulse spacing which is the velocity divided by the pulse repetion frequency (PRF). [1]

When digitally recording the data, the processing is more flexible, but algorithm development has continued to focus on specific radars or applications. The most commonly used SAR processing method is the range-Doppler algorithm (RDA) [2]. It was developed in the mid 1970's for processing data from JPL's SEASAT SAR. It efficiently focuses the data in both range and azimuth using frequency domain operations. One drawback is a computationally costly interpolation to correct the range-cell migration. Another limitation is the inability to handle squint-mode or wide-beam SAR. There is, however, a modification to the RDA that can help in these cases by introducing a secondary range-compression (SRC). The SRC accounts for an additional term of a Taylor series approximation, but only at a reference range [2].

The chirp scaling algorithm (CSA) was developed to eliminate the interpolation used for range-cell migration correction (RCMC) in the RDA [2]. The CSA employs a two step scaling process to shift the target trajectories (a differential shift and a bulk shift), removing the RCM. Like the RDA, the CSA neglects the range-dependence of the SRC and all the

higher order terms from the Taylor series approximation, limiting its utility for high squint and wide beamwidth SARs. The frequency scaling algorithm (FSA) is related to the CSA, but it works with dechirped SAR data. The FSA has the same limitations as the CSA.

A third processing method has its origins in seismic processing and is known as the omega-K algorithm (ωKA) [2] or range migration algorithm (RMA) [1]. The ωKA directly processes the data in the two-dimensional frequency domain (wavenumber domain) without approximations in the signal model. The SAR data is compensated for a single reference range, then a Stolt interpolation (which is computationally costly) compensates for the other ranges in the image. Because there are no approximations in deriving the signal model, the algorithm is suitable for very wide beamwidths or high squint. The drawback is that with all the processing done in the wavenumber domain, there is no opportunity for implementing range-dependent compensation for non-ideal platform motion.

The most general, and most computationally taxing algorithm is known as backprojection, or tomographic processing [3]. In backprojection, each pulse is range compressed and the distance to each pixel in the final image is determined for each pulse location. The portion of each range compressed pulse that corresponds to the range to a given pixel is multiplied by the expected phase for that range and is summed across the entire collection. In this way any beamwidth, squint, frequency, or motion can be exactly compensated (to the limits of the precision of the motion measurement unit).

Other algorithms have been developed for specific applications. The polar format algorithm [1] is an older method for compensating for the range cell migration in spotlight SAR imaging. The SPECAN algorithm is designed to provide quick-look SAR imagery of lower quality with less processing time. Also, the SPECAN algorithm can be used together with an imaging mode called ScanSAR, where the antenna beam scans outward during each pulse to increase the swath width. Another older algorithm for SAR processing is called Doppler beam sharpening, in which signal returns are placed in individual Doppler bins, and then processed to form an image.

While this variety of SAR processing algorithms can seem overwhelming, each algorithm is in reality a different approximation of a mythical exact SAR reconstruction. This connection between algorithms is illustrated by conflicting reports of the origins of the CSA.

In [2], Cumming and Wong state that the CSA grew out of the desire to eliminate the interpolation in the RDA. In [1] Carrara, Goodman, and Majewski claim that the CSA was developed as an approximation to the Stolt-interpolation of the RMA. Because of the underlying connection between algorithms, both views of the CSA are appropriate.

The more efficient precision algorithms, the RDA, CSA, and ωKA, are know as frequency domain algorithms because they rely on performing the SAR processing in the frequency domain. They each have their limitations, but are all much faster than backprojection. It is desireable to extend the utility of frequency domain algorithms by overcoming their limitations. The main work of this dissertation answers the question, "What improvements to SAR processing algorithms can be made to give better results when existing algorithms suffer image degradation due to algorithmic approximations?"

1.1 Contributions

Through my research, I have been able to make unique contributions. This section summarizes the contributions of this dissertation to the body of knowledge related to synthetic aperture radar processing theory.

In this dissertation, I show that for SAR systems with lower center frequencies, larger bandwidths, and wider beamwidths, the approximations used in common frequency-domain SAR processing algorithms are inadequate. I develop an expression for the phase error due to the Taylor series expansion approximation of the SAR signal in the wavenumber domain and a visualization of the error over the two-dimensional frequency support band. I analyze the effects of varying the SAR parameters for a given approximation. I develop a generalized algorithm and a set of guidelines to determine the approximation order of the Taylor approximation required for proper image processing for a given set of SAR parameters. This efficient frequency-domain algorithm is built upon the CSA framework. Accounting for higher order terms increases the precision over the existing CSA variations.

In the emerging technology of LFM-CW SAR, I have contributed various processing methods and system design innovations as detailed in this dissertation. One of the key differences between LFM-CW SAR and pulsed SAR is that in LFM-CW SAR the stop-and-go approximation used for pulsed processing is not valid. Also, LFM-CW SAR uses

an analog dechirp before sampling the signal returns (this is sometimes done in spotlight SAR and is called de-ramping or stretch mode). Taking these into account, as part of this dissertation, I develop an LFM-CW backprojection algorithm for both exactly and approximately compensating for the continuous platform motion. For more efficient processing, frequency domain processing algorithms can be used. I derive the LFM-CW SAR signal in the dechirped Doppler domain and show the effect of using a Taylor series expansion as an approximate model for the SAR signal. I develop a generalized frequency scaling algorithm (GFSA) that uses an arbitrary number of terms of the the Taylor series approximation to process LFM-CW SAR data.

For LFM-CW SAR, the continuous platform motion must also be taken into account when correcting for the non-ideal translational motion of the platform (the deviation from the ideal straight line path). I develop the theory for expressing the effects of translational motion on the LFM-CW SAR signal, and develop compensation algorithms that exactly and approximately correct for the non-ideal platform motion.

Treating the SAR signals in the generalized way has led to a secondary set of contributions. In the appendices I develop a pair of interesting and useful processing enhancements. First, I use some of the tools developed for correcting the non-ideal motion of LFM-CW SAR and apply them to the motion compensation problem of pulsed SAR. I develop a motion compensation algorithm that avoids a computationally taxing interpolation for differential motion correction.

Next, I develop the theory for coherently combining the returns from the separate frequency bands of a multi-frequency-band SAR system to improve the range resolution. I also develop a practical algorithm for accomplishing this task. The resolution improvement is achieved by combining the bandwiths to form a larger single bandwidth. This method can be used to increase the bandwidth given hardware constraints (each band can have its own RF hardware) and as an alternative to common notched-chirp approaches to avoid transmitting in keep-out bands. Also, I have contributed to the design, hardware assembly, system testing, and processing software development for four different SAR systems during the course of my research.

1.2 Outline

This dissertation is organized as follows. In Chapter 2, the background information necessary for understanding the development of the research in the remainder of the dissertation is given. This includes the basics of synthetic aperture radar operation, the hardware subsystems, system parameters, and operating modes, including pulsed and LFM-CW SAR. Next, we discuss the formation of the large synthetic aperture, which is necessary for fine resolution imaging. This synthetic aperture is generated by the movement of the radar platform. Then, the basic steps in SAR processing are given.

Chapter 3 describes the development of a generalized frequency-domain processing method for pulsed SAR. The general SAR signal is presented, and the approximations made in traditional processing algorithms are discussed. The effects of the approximations are shown to degrade the SAR focusing under certain conditions. A generalized processing algorithm is developed which includes an arbitrary number of terms of the Taylor series approximation. A series of simulations are used to demonstrate the enhanced performace of the generalized method. Including higher order terms in the processing improves the focusing when traditional algorithms suffer from approximation-induced image degradation. This work is published in [4].

In Chapter 4, the LFM-CW SAR signal is carefully derived, including the continuous motion of the platform. New backprojection algorithms are developed that handle the continuous motion both exactly and approximately. The signal in the dechirped-Doppler domain is derived and the approximations used in traditional processing algorithms are discussed. As with pulsed SAR, these approximations lead to degradation of image quality under certain circumstances. A generalized frequency-scaling algorithm is developed which uses an arbitrary number of terms from the Taylor expansion approximation. It is shown through simulations that including higher order terms improves the image focusing under the conditions that traditionally result in image degradation. This work has been submitted for publication in [5]

Chapter 5 further explores the continuous motion problem of LFM-CW SAR. The assumption that the platform is traveling in a straight line and at a constant speed is used in processing algorithm derivations (with the exception of backprojection), but is invalid for

6

any real data collection. While traditional motion compensation algorithms use a stop-and-go approximation in correcting the non-ideal motion, this chapter formulates the LFM-CW non-ideal motion problem and shows that the continuous motion requires continuous correction. The non-ideal motion errors are analyzed and a motion compensation scheme is developed including a theoretical exact compensation and a usable approximate correction. The performace of the new algorithm compared to traditional methods is shown with simulated data, and the results of applying it to real SAR data are also shown. This work is published in [6].

Chapter 6 summarizes and concludes the work of the dissertation. Possible avenues of future research are suggested and my contributions are reviewed. Additional work is contained in the appendices. Appendix A describes the development of a new motion compensation algorithm for pulsed SAR that performs differential correction without the use of an interpolator, improving the processing efficiency. Appendix B shows the development of an algorithm for coherently combining SAR data from multiple frequency bands in order to improve the range resolution. The theory is developed and the performance is demonstrated with an algorithm developed to perform the combinations with simulated and real SAR data. Appendix C describes the designs of four different SAR systems which I have worked with in the course of my research. I have contributed to these SAR systems with system design, processing development, hardware assembly, and testing.

CHAPTER 2.   BACKGROUND

This chapter presents the fundamentals of synthetic aperture radar system design and theory that are necessary for the development of the research central to this dissertation. An overview is given of the radar operation, introducing hardware components and system parameters crucial to any SAR processing theory. Two SAR operating modes, pulsed SAR and continuous wave SAR, are compared and contrasted. The importance of platform motion is discussed, including the SAR imaging geometry, and the motion-induced signal phase history. Finally, basic SAR processing is discussed including range compression, range cell migration correction, and azimuth compression.

2.1   Radar Operation

SAR is an active microwave remote sensing technique that produces wide-area images of high resolution. While passing by a target, the SAR illuminates the area with a series of coherent pulses. The series of radar echoes from the target area are digitized and processed to form the image. SAR compliments optical imagery in a variety of applications and has a number of advantages. The radar is its own illumination source, thus it can operate equally well day or night. The choice of frequencies in the microwave band allows imaging through clouds, precipitation, dust, and smoke, and at the low-frequency end of the microwave spectrum, foliage and dry ground penetration are possible. The choices of SAR system parameters and hardware components are often driven by specific applications. The parameters used for a SAR data collection determine the processing methods that can be used.

2.1.1 SAR Systems and Hardware

A basic SAR system consists of five main subsections, as seen in Fig. 2.1. The subsections are: timing and control, signal generation and transmission, signal reception and data recording, motion measurement and estimation, and image formation. The separate subsystems must work closely together for the SAR to operate correctly.

Basic SAR System

```
┌──────────────┐      ┌──────────────┐
│ Timing and   │─────▶│   Motion     │
│  Control     │      │ Measurement  │
└──────────────┘      └──────────────┘
        │                    │
        ▼                    ▼
┌──────────────┐      ┌──────────────┐
│   Signal     │      │   Signal     │
│ Generation   │─────▶│ Reception and│
│ and Transmit │      │Data Recording│
│              │      │              │        ┌──────────┐
│        ┌─DDS┐│      │┌ADC┐  ┌Memory┐│──────▶│  Image   │
│        └────┘│      │└───┘──└──────┘│        │Formation │
│ Up-Mixer ⊗   │      │  ⊗  Down-Mixer│        └──────────┘
│              │      │              │
│  Power    ▽  │      │  △    LNA     │
│ Amplifier    │      │              │
└──────────────┘      └──────────────┘
  Antenna  △            △   Antenna
```
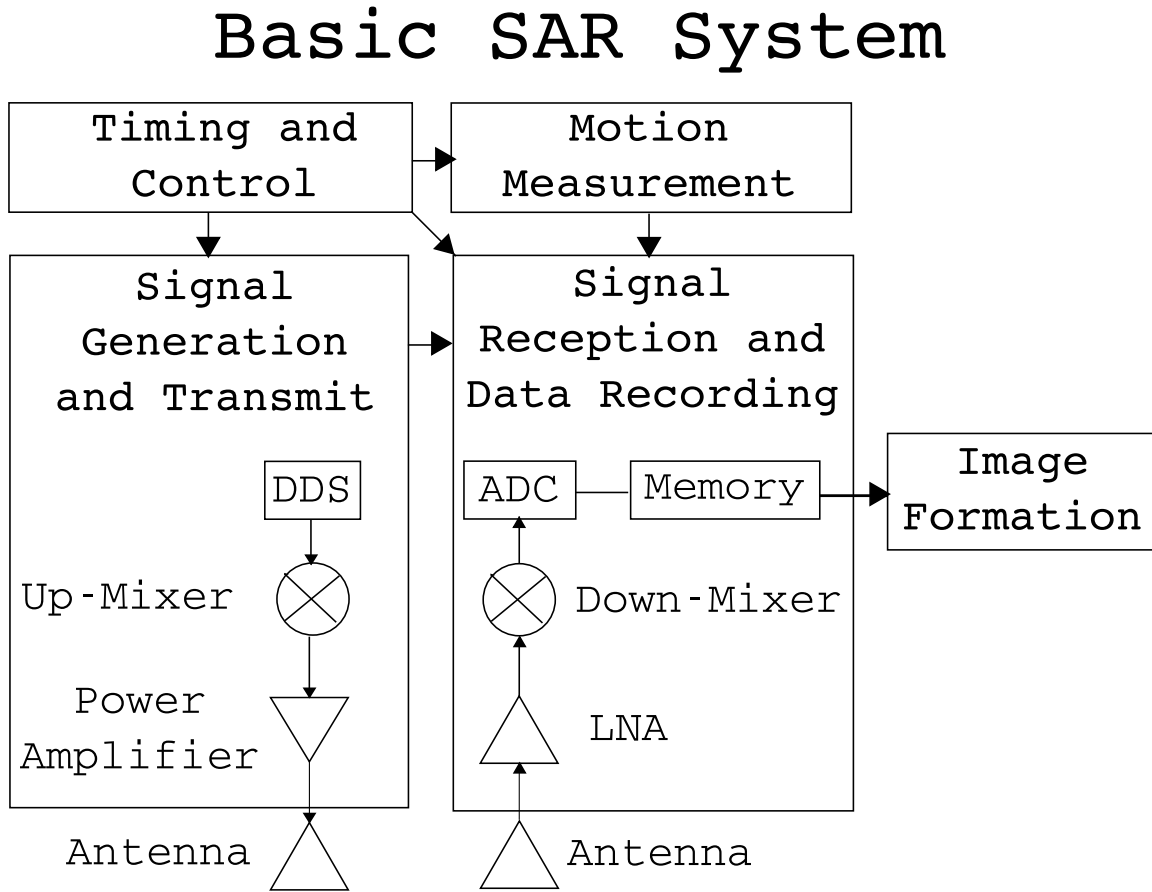
Figure 2.1: Basic SAR System Block Diagram

Timing and Control

To form an image, the SAR signal must be coherent over the entire series of pulses that make up a data collection. An important part of that is maintaining coherence and consistent timing between the separate subsystems that make up the SAR. The timing

and control system maintains coherence from pulse to pulse and between subsystems and determines the timing for turning the radar on and off and for switching between transmit and receive.

Signal Generation and Transmit

Before the SAR signal is generated, a number of important system parameters are determined, including center frequency, bandwidth, pulse length, and pulse repetition frequency (PRF). The signal can be generated using a direct digital synthesizer (DDS) or a voltage controlled oscillator (VCO). A DDS allows a specific waveform to be generated from programmed digital controls. The most common SAR signal is a linear frequency modulated (LFM) chirp, where the signal spans the bandwidth over the pulse length, changing in frequency at a linear rate. This cycle is repeated at the PRF.

The SAR signal is usually generated at or near baseband and then mixed up to the desired operating frequency before transmission. A linear frequency modulated (LFM) transmit signal can be expressed

$$s_t(t) = A(t) \exp\left(j\left(2\pi f_0 t + \pi k_r t^2 + \phi\right)\right) \tag{2.1}$$

where $A(t)$ is the signal amplitude and, as a function of t, defines the pulse length with a rect function, f_0 is the frequency at the beginning of the chirp, k_r is the chirp rate, and ϕ is the starting phase which can usually be neglected. In the transmission chain, a power amplifier increases the transmit power to a specified level. The transmitted signal needs to have enough power so that the signal to noise ratio (SNR) is large enough to generate a quality image. SNR also depends on the specific imaging parameters, especially range to target and antenna beamwidth.

The antenna is designed with certain beamwidths in azimuth and elevation and can be pointed in different directions for different SAR imaging modes. A fixed antenna pointing orthogonal to the motion of the platform is used in stripmap mode, as seen in Fig. 2.2; the antenna is pointed slightly forward or backward for squint mode. In spotlight mode the antenna moves (mechanically using a gimbal or electronically using a phased array) to stay
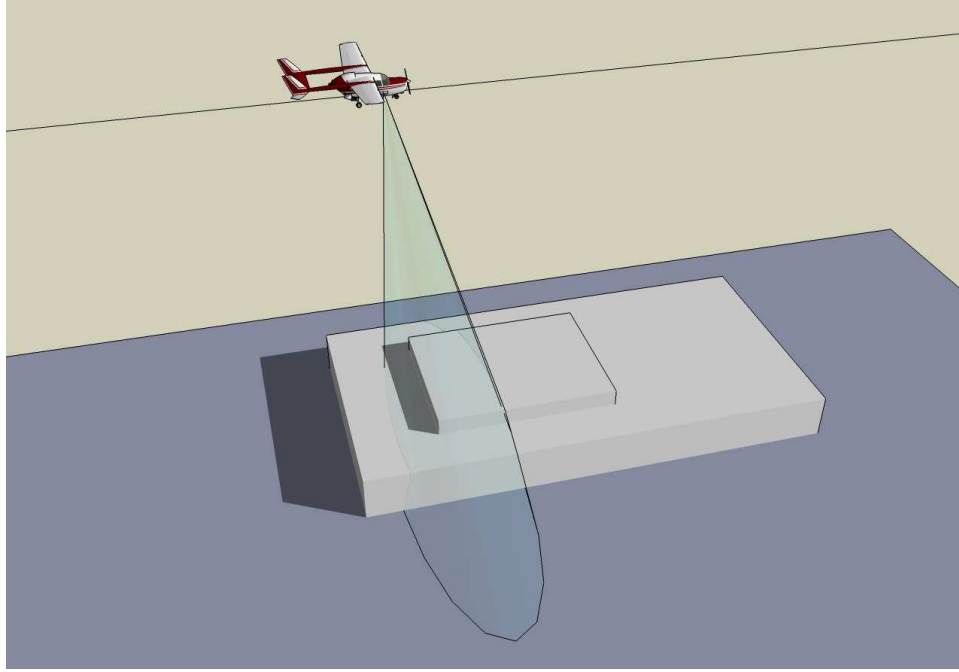
Figure 2.2: Stripmap SAR Imaging Geometry

pointed at the center of the target area, as seen in Fig. 2.3 [7]. The beamwidth and antenna pointing determine the illuminated footprint on the ground.

The platform motion, the antenna pointing, and the antenna beamwidth determine the Doppler frequencies of the return signals from the targets in the illuminated area (the Doppler bandwidth). The maximum Doppler frequency cannot be greater than the Doppler bandwidth of the system, defined by the PRF, or else Doppler aliasing occurs.

Signal Reception and Data Recording

The amplified signal transmitted through the antenna propagates to the target area. The propagation environment consists of the layers of atmosphere, usually approximated as free space (with the notable exception of ionospheric induced distortions such as Faraday rotation for orbital SAR), and the distributed scatterers that make up the target scene. A very small portion of the transmit signal is reflected back to the radar. The reflected signal from a point target can be expressed as

$$s_r(t) = A'(t) \exp\left(j\left(2\pi f_0\left(t - \tau\right) + \pi k_r\left(t - \tau\right)^2 + \phi\right)\right) \tag{2.2}$$
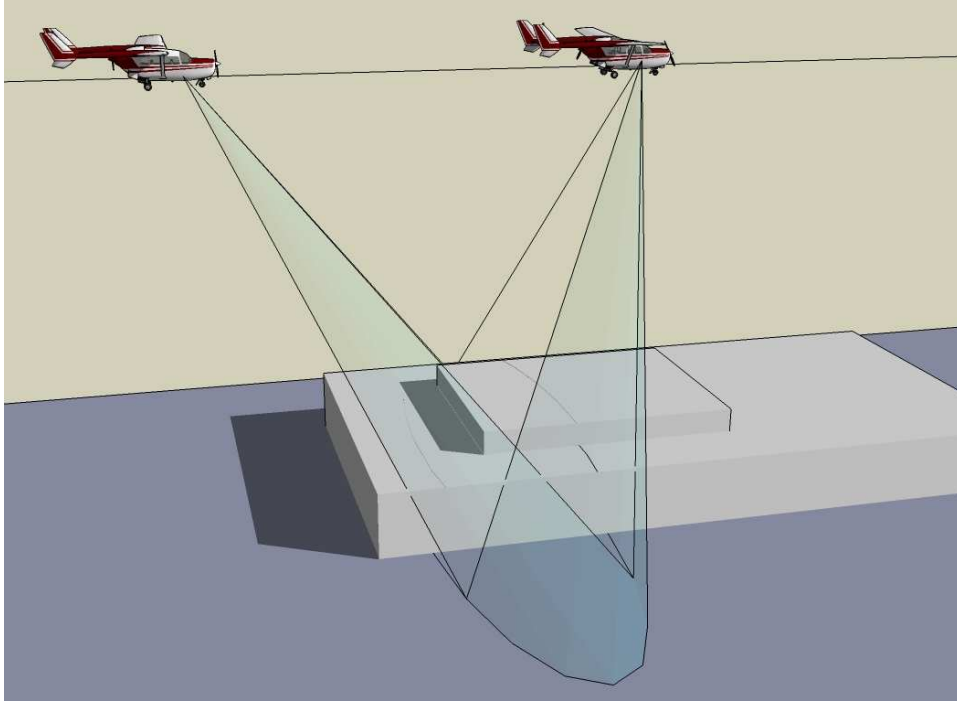
Figure 2.3: Spotlight SAR Imaging Geometry

where $A'(t)$ is an attenuated version of $A(t)$ and τ is the two-way time of flight to the target at range R,

$$\tau = \frac{2R}{c_0}. \tag{2.3}$$

For monostatic operation the radar echoes are received through the transmit antenna, isolated from the transmit path by a circulator. For bistatic operation, separate transmit and receive antennas are used, with the receive antenna separated from the transmit antenna by a known baseline.

The receiver is very sensitive in order to detect the return echoes and is protected in many systems from the powerful transmit signal by being shut off during signal transmission. Additionally, a technique called range gating is used to limit the collected data to a narrow set of ranges. This can reduce the data volume by only collecting data reflected from the area we are interested in imaging. This is often done by careful timing of when the receiver is turned on.

The received signal is amplified with a low-noise amplifier (LNA) and mixed down to an appropriate band for sampling. One option for sampling is offset video with a single

channel at a rate at least twice the bandwidth of the signal. Another option is quadrature demodulation to baseband with two channel IQ sampling. After the signal from Eq. (2.2) is mixed down by a frequency, f_{md}, the signal ready to be recorded is

$$
\begin{aligned}
s_{rmd}(t) &= A''(t) \exp\left(j\left(2\pi f_0\left(t - \tau\right) - 2\pi f_{md}t + \pi k_r\left(t - \tau\right)^2 + \phi\right)\right) \\
&= A''(t) \exp\left(j\left(2\pi\left(f_0 - f_{md}\right)t - 2\pi f_0\tau + \pi k_r\left(t - \tau\right)^2 + \phi\right)\right).
\end{aligned}
\tag{2.4}
$$

The first SAR systems recorded the data optically on film and used analog optical processing to produce the image. Modern SAR systems digitize the data and either store it on board, transmit it to a ground station, or process it on-board.

Motion Measurement

An important part of SAR data collection and processing that isn't directly part of the radar is the motion measurement system [1]. SAR processing requires knowledge of the flight path during data collection, or at least an estimation of the flight path. Motion measurement systems used with the SAR systems developed at BYU have employed a variety of methods including manually recording the velocity readings from the aircraft instrumentation during data collection, utilizing a low rate GPS solution inserted into the SAR data, and employing a high rate inertial measurement unit (IMU) coupled with GPS and carefully time-tagged and aligned with the collected SAR data. The better the motion measurements, the more accurately the SAR data can be processed to form a well focused image. The important process of image formation is documented in Section 2.3.

2.1.2 Pulsed SAR

The most common type of SAR transmits short pulses. This allows ample time to switch off the transmitter, turn on the receiver and reuse the transmit antenna as the receive antenna. For pulsed SAR there are several important factors to be considered in processing the data: the pulse length, the range resolution, and the method of range compression.

Pulse Length

The length of time that the SAR is transmitting is known as the pulse length, t_p. For a LFM chirp, t_p is related to the bandwith and the chirp rate by

$$BW = t_p \cdot k_r. \tag{2.5}$$

For a given transmit power, a longer pulse produces a better SNR after range compression, but the cost is increased data volume. There are other factors that limit the pulse length, such as the maximum duty cycle of the power amplifier. The transmit duty cycle, expressed as the fraction of time that the power amplifier is on, is

$$DutyCycle = t_p \cdot PRF. \tag{2.6}$$

The two-way time of flight to the nearest point of the area we desire to image also limits the pulse length. Before the return echo from this nearest point begins to arrive at the radar, we must allow time for the power down transient of the power amplifier and the power on transient of the receiver to stabilize. For very large ranges, such as imaging from a satellite, carefully timing the transmit and receive periods allows for multiple pulses to be in transit to and from the target area at the same time.

Range Resolution & Compression

Range compression is performed via matched filtering the received signal with expected return signal (a copy of the transmit signal). This process is detailed in Section 2.3.1. Using this method, the return from a point target is compressed from a signal with length t_p to a focused point with a width equal to the range resolution. Range resolution is defined by the minimum distance separating targets for which the radar echoes can be separated. For a single frequency pulse of length Δt the spatial resolution is expressed as

$$\Delta R = \frac{c_0 \Delta t}{2}. \tag{2.7}$$

Spatial resolution can also be expressed in terms of the signal bandwidth. The bandwidth of an interupted continuous-wave (ICW), or a single frequency pulse, is approximated $BW = 1/\Delta t$. The bandwidth for a modulated signal (such as the LFM signal in our example) is the transmitted bandwidth. Typically, range resolution is expressed as

$$\Delta R = \frac{c_0}{2BW}. \tag{2.8}$$

2.1.3 Continuous Wave SAR

The pulse length is maximized when the SAR is continuously transmitting, or equivalently when a single pulse fills the entire pulse repetition interval (PRI). Maximizing the pulse length maximizes the SNR for a given transmit power. This requires bistatic operation, one antenna to continuously transmit and another antenna to continuously receive. One problem with this is that the direct feedthrough from the transmitter to the receiver can have much higher power than the radar echoes from the target area. This feedthrough must be managed to prevent it from drowning out the desired signal. Various methods have been developed for accomplishing this task. One method involves an analog dechirp in the receive chain. This dechirp converts the feedthrough to a single frequency that can be filtered out in hardware. The analog dechirp also offers some other advantages particularly useful for CW SAR: a reduced sampling bandwidth and a simplified range compression computation. Other considerations will be discussed later, including the range resolution calculation and compensation for the continuous platform motion that occurs during each chirp.

Analog Dechirp

With an analog dechirp, the received signal is mixed with a copy of the transmit signal. The dechirp signal can be a synchronous copy of the transmit signal (for direct dechirp) or a delayed version. In either case, the result is a frequency difference between the signals. For direct dechirp, this frequency difference, Δf, corresponds directly to the

distance from the target (the target range),

$$\Delta f = \frac{2Rk_r}{c_0}.$$ (2.9)

Or for a delayed dechirp, with delay d,

$$\Delta f = \left(\frac{2R}{c_0} - d\right) \cdot k_r.$$ (2.10)

The feedthrough generates a frequency difference corresponding to a range near zero, which is very different from the frequencies that correspond to the ranges in the target area. A bandpass filter with high out-of-band rejection can be used to attenuate the feedthrough power while passing the desired signal.

The dechirping operation also reduces the signal bandwidth from the full transmit bandwidth to a dechirped bandwidth determined by the maximum range of interest, or the width of the bandpass filter. This dechirped bandwidth is

$$BW_{dc} = \frac{2R_{max}k_r}{c_0}$$ (2.11)

for a direct dechirp, or for a delayed dechirp,

$$BW_{dc} = \frac{2R_{max}k_r}{c_0} - d \cdot k_r = \frac{2R_{max}k_r}{c_0} - \frac{2R_{min}k_r}{c_0},$$ (2.12)

where R_{max} is the maximum range that can be imaged and R_{min} is the minimum range.

The sampling and data storage requirements are reduced by using the analog dechirp. Rather than continuously sampling at a rate sufficient to digitize the transmit bandwidth, the data is continuously collected at a much lower rate, sufficient for the bandwidth of the dechirped signal.

If the copy of the transmit signal used for dechirping is delayed, then the bandpass filter acts as a range gate, filtering out the signal returns from ranges outside our desired imaging area and maximizing the usage of the data storage space.

Range Resolution & Compression

For the dechirped data, range compression can be accomplished with a range Fourier transform, which separates the frequencies (and the ranges). The range resolution is determined by the frequency resolution of the Fourier transform,

$$\Delta f_r = \frac{1}{t_p} = \frac{f_s}{N}, \tag{2.13}$$

where f_s is the sample rate of the analog to digital converter (ADC) and N is the number of samples collected for a single chirp. For dechirped SAR data, frequencies correspond to ranges; thus this frequency resolution corresponds to a spatial range resolution, ΔR, calculated as

$$\Delta R = \Delta f_r \cdot \frac{c_0}{2 \cdot k_r} = \frac{c_0 \cdot f_s}{2 \cdot N \cdot k_r}. \tag{2.14}$$

For CW SAR $N/f_s = t_p$ and $t_p \cdot k_r = BW$ (the transmit bandwidth), so that Eq. (2.14) simplifies to

$$\Delta R = \frac{c_0}{2 \cdot BW} \tag{2.15}$$

which is equivalent to Eq. (2.8), the range resolution calculation for pulsed SAR. The details of range compression for CW SAR are given in Chapter 4.

2.2 Moving Platform

Essential to all types of SAR operation is the motion of the platform, which also introduces complications. As the authors of [1] state, "In SAR, *motion* is the *solution* and the *problem*." Without motion, or without using synthetic aperture techniques, the azimuth resolution of a radar is dependent on the beamwidth of the antenna, the resulting azimuth spatial resolution is highly dependent on range,

$$\Delta z_{ra} = 2R \tan\left(\frac{\theta_a}{2}\right). \tag{2.16}$$

The imaging geometry of SAR allows for the motion necessary to generate a target phase history that is due to the changing range between target and platform.
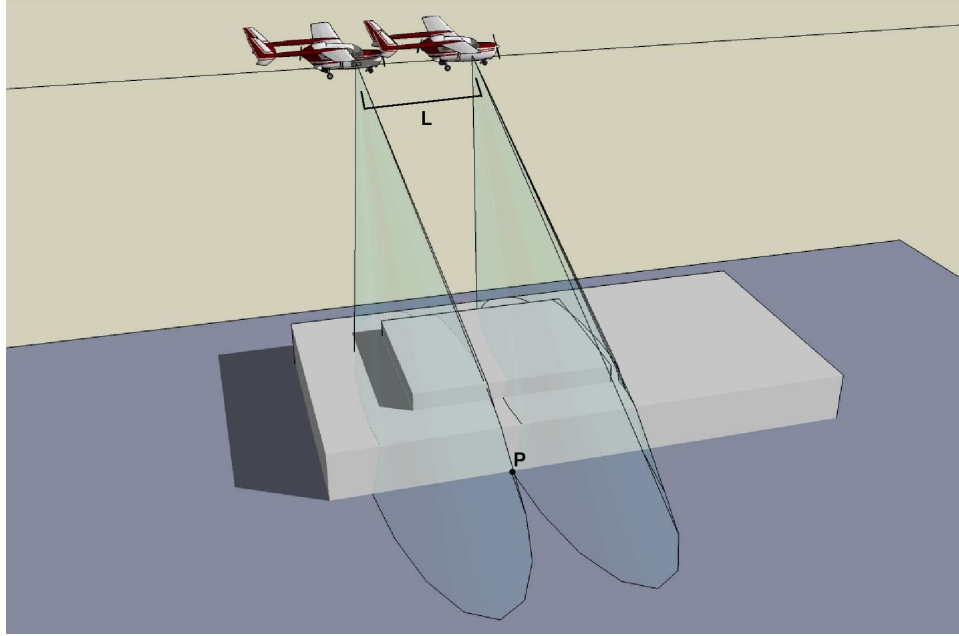
Figure 2.4: Stripmap SAR Imaging Geometry. The length of the synthetic aperture, L, is seen as the distance between the two aircraft positions. The target at point P is illuminated by the antenna beam for the length of the synthetic aperture.

2.2.1 SAR Imaging Geometry and Azimuth Resolution

In Fig. 2.4 the SAR platform moves along the flight path illuminating a target area off to one side. For airborne SAR, the flight path is ideally linear with a constant velocity (though in the real world there are always deviations from this ideal). The flight path for spaceborne SAR follows an orbital ephemeris. Nonlinear flight paths such as a circular path around a target can also be used, provided that the motion is precisely recorded and the data is processed with an appropriate algorithm that does not rely upon a linear flight path assumption.

For stripmap mode the antenna is fixed and pointed broadside (orthogonal to the direction of travel) as in Fig. 2.2. For squint mode it may be pointed forward or backward from broadside. In these cases, the Doppler bandwidth is fixed by the antenna beamwidth and the velocity of the platform, and the azimuth resolution is limited by the beamwidth. In spotlight mode the antenna pointing is controlled in order to maintain the center of the target area in the center of the antenna beam, as seen in Fig. 2.3, in this way the Doppler

bandwidth can be increased, or in other words the antenna beamwidth is increased, resulting in finer azimuth resolution.

The Doppler frequency of a target at the farthest extent of the antenna beam in azimuth is

$$f_d = \frac{2 \cdot v}{\lambda} \sin \frac{\theta_a}{2} \tag{2.17}$$

where θ_a is the azimuth beamwidth and λ is the wavelength of the center frequency. The Doppler bandwidth is $2 \cdot f_a$. The azimuth resolution in time is the reciprocal of the Doppler bandwidth. This time resolution becomes the azimuth spatial resolution when multiplied by the velocity of the platform

$$\Delta z = \frac{v}{2 \cdot f_a} = \frac{\lambda}{4 \sin \frac{\theta_a}{2}}. \tag{2.18}$$

Using the small angle approximation to estimate $\sin(\theta_a/2) \approx \theta_a/2$, then estimating the beamwidth from the physical length of the antenna in azimuth, L_{az}, we see that $\theta_a \approx \lambda/L_{az}$ and

$$\Delta z = \frac{\lambda}{4 \sin \frac{\theta_a}{2}} \approx \frac{\lambda}{2\theta_a} \approx \frac{L_{az}}{2}. \tag{2.19}$$

An important and useful characteristic of SAR imaging is evident in these expressions for the azimuth resolution: the resolution is independent of range.

2.2.2 Change in Range and Signal Phase History

With the platform moving during data collection, the range to a target changes slightly from one chirp to the next. While this change in range is much less than the resolution of the system, it is a measurable fraction of a wavelength and results in a change in the phase of the return echo. Tracking this phase history over the length of time that the target is in the illuminated antenna beam footprint (the length of the synthetic aperture, as seen in Fig. 2.4) allows us to compress the target, focusing it in azimuth.

If we were to transmit a single frequency,

$$s_{t1} = 2\pi f_0 t, \tag{2.20}$$

and receive the echo at

$$\tau = \frac{2R(\eta)}{c_0} \qquad (2.21)$$

where $R(\eta)$ is the range to target that changes from pulse to pulse, or in other words is dependant on "slow time" η, then the received signal is

$$s_{r1} = 2\pi f_0 \left(t - \tau\right) = 2\pi f_0 \left(t - \frac{2R(\eta)}{c_0}\right) = 2\pi f_0 t - \frac{4\pi f_0 R(\eta)}{c_0}. \qquad (2.22)$$

Thus the "expected phase" for a SAR signal is often expressed as

$$\Phi_{ex} = \frac{4\pi R(\eta)}{\lambda}. \qquad (2.23)$$

For a linear flight path, an expression for R is

$$R(\eta) = \sqrt{R_0^2 + (v \cdot \eta)^2} \qquad (2.24)$$

where R_0 is the range of closest approach and v is the velocity. Most traditional SAR processing algorithms are derived using this expression (or a parabolic approximation of it) for $R(\eta)$. When real world deviations from this ideal flight path result in defocusing, motion compensation can be applied to adjust the signal phase to match the ideal expression. Also, algorithms that are more precise and more computationally taxing can be employed to process SAR data with an arbitrary change in range, inherently correcting for non-ideal motion and allowing for a variety of nonlinear flight paths (e.g. circular).

In any case, the basic idea behind SAR processing involves matching the expected phase of the signal form a target in order to compress, or focus, the energy from that target. The remainder of this dissertation is focused on the details of this processing.

2.3   Processing

In modern digital SAR processing, there are three main steps to properly focusing the data: range compression, range cell migration correction, and azimuth compression. These steps are illustrated in Fig. 2.5. While different algorithms perform these operations
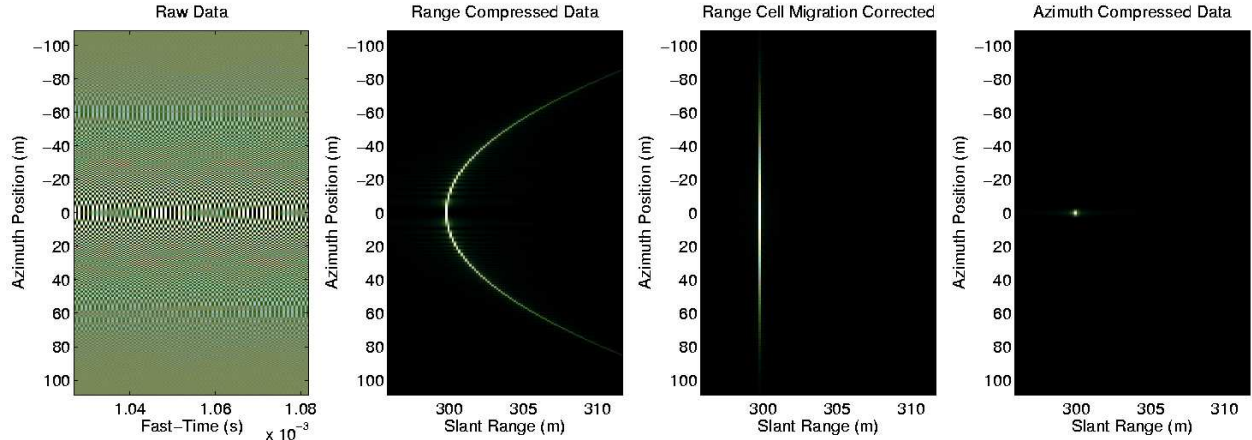
Figure 2.5: Simulated SAR data for a point target. From left to right the SAR data is shown for each main processing step. In the raw SAR data, the azimuth modulation is visible in the way the signal changes from pulse to pulse. The range compressed data shows how the range to target changes as the platform moves past the target (it is this change in range that creates the azimuth modulation visible in the raw data). After range cell migration correction, all the radar signal energy returned by the point target is contained within the range bin at the range of closest approach. After azimuth compression, the signal return from the point target is fully focused, as seen in the final image.

in different ways, the basic concepts are the same. This section uses examples from a pulsed SAR processed with the range-Doppler algorithm (RDA) [8].

2.3.1 Range Compression

The received signal from a point target is an attenuated copy of the transmit signal delayed by the two-way time of flight to the target, τ, expressed as

$$ s_r = A''(t) \exp\left(j\left(-2\pi f_0\tau + 2\pi\left(f_0 - f_{md}\right)t + \pi k_r\left(t - \tau\right)^2 + \phi\right)\right). \qquad (2.25) $$

The return echo is an attenuated copy of the transmit signal, so we define a reference chirp equal to the transmit signal. When the received signal is convolved with the reference chirp, the result is a peak where the signals line up. This peak corresponds to the target range. In processing, this is efficiently done with an FFT, a complex-phase multiply, and an inverse-FFT. In other words, a matched filter for the transmitted chirp. For simplification let $f_0 = f_{md}$. Mathematically we express the Fourier transform of the received signal, Eq. (2.25),

22

as

$$S_r = \int_\tau^{\tau+t_p} s_r \cdot \exp\left(-j2\pi f_r t\right) dt = B(f_r) \cdot \exp\left(-j \cdot \frac{2\pi\tau k_r f_0 + 2\pi\tau k_r f_r + \pi f_r^2}{k_r}\right) \quad (2.26)$$

where $B(f_r)$ is a complex function which principally limits values of S_r to within the bandwidth of the chirp. $B(f_r)$ can be approximated by a rect function.

The Fourier transform of the time reversed conjugate of the reference chirp is

$$H_{rc} = \int_0^{t_p} \exp\left(-j\pi k_r(-t)^2\right) \cdot \exp\left(-j2\pi f_r t\right) dt = B'(f_r) \cdot \exp\left(j\frac{\pi f_r^2}{k_r}\right) \quad (2.27)$$

where $B'(f_r)$ is approximately the same as $B(f_r)$, and is approximated by the same rect function.

S_r and H_{rc} are multiplied together

$$S_r \cdot H_{rc} = B(f_r) \cdot B'(f_r) \cdot \exp\left(-j2\pi\tau\left(f_0 + f_r\right)\right) \quad (2.28)$$

and the inverse Fourier transform is taken

$$
\begin{aligned}
s_{rc} &= \int_0^{t_p \cdot k_r} S_r \cdot H_{rc} \cdot \exp\left(j2\pi f_r t\right) df_r \\
&= -j\frac{\left(\exp\left[j2\pi k_r t_p\left(t - \tau\right)\right] - 1\right)\exp\left(-j2\pi f_0 \tau\right)}{2\pi k_r\left(t - \tau\right)} \\
&= -j\frac{\left(\exp\left[j\pi k_r t_p\left(t - \tau\right)\right] - \exp\left[j\pi k_r t_p\left(\tau - t\right)\right]\right)\exp\left(j\pi k_r t_p\left(t - \tau\right) - j2\pi f_0 \tau\right)}{2\pi k_r\left(t - \tau\right)} \\
&= \frac{\sin\left(t_p\pi k_r\left(t - \tau\right)\right)\exp\left(j\pi k_r t_p\left(t - \tau\right) - j2\pi f_0 \tau\right)}{\pi k_r\left(t - \tau\right)} \\
&= t_p \cdot \operatorname{sinc}(t_p\pi k_r\left(t - \tau\right)) \cdot \exp\left(j\pi k_r t_p\left(t - \tau\right) - j2\pi f_0 \tau\right) \\
&\approx t_p \cdot \operatorname{sinc}(t_p\pi k_r\left(t - \tau\right)) \cdot \exp\left(-j2\pi f_0 \tau\right). \quad (2.29)
\end{aligned}
$$

The result shows the peak of the sinc function at the range to the target. We can also see that the peak is higher when the pulse length is longer. The simplification that gives the last line of Eq. (2.29) is due to the fact that the exponential term dependent on $(t - \tau)$ is unity when the sinc function is at a maximum. The phase of the range compressed signal is identical to the expected phase from Eq. (2.23).

2.3.2 Range Cell Migration Correction

When a series of range compressed pulses are stacked together, the change in range from one pulse to the next (the target trajectory) is clearly visible, as in Fig. 2.5. Using an antenna with a wide enough azimuth beamwidth results in targets moving through multiple range bins (range resolution elements) across the length of the synthetic aperture; this is called range cell migration. To properly focus a target in azimuth, the data along the entire target trajectory is used, but doing so is complicated by the range cell migration. One solution is to shift the trajectories such that the returns from a single target remain in the same range bin for the duration of the synthetic aperture. This allows us to use an FFT based matched filter along each range bin to focus all the energy form a target. The RDA performs range cell migration correction (RCMC) by employing an interpolation as described below, while the CSA uses chirp scaling functions to perform this operation without a computationally costly interpolation [8].

The derivation of the SAR signal after an azimuth Fourier transform (i.e., the signal in the range-Doppler domain) is given in Chapter 3. The signal returns from targets with equal range-of-closest-approach are co-located in the range-Doppler domain with the same trajectory shape. A migration factor, $D(f_\eta)$, can be used to calculate target trajectories in the range-Doppler domain,

$$D(f_\eta) = \sqrt{1 - \frac{c_0^2 f_\eta^2}{4v^2 f_0^2}}. \tag{2.30}$$

The curved trajectory of all targets with range of closest approach R_0 is expressed

$$R_{rd}(f_\eta) = \frac{R_0}{D(f_\eta)}. \tag{2.31}$$

To straighten the curved trajectories so that all the energy returned form a target is contained in the single range bin R_0, an azimuth frequency dependent interpolation can be used, shifting the trajectories by $R_{rd}(f_\eta) - R_0$. The results of range cell migration correction are illustrated in Fig. 2.5.

2.3.3 Azimuth Compression

While range compression is performed using a matched filter with the range chirp, azimuth compression uses a matched filter of the Doppler chirp. With the SAR signal range compressed and the range cell migration removed, the signal can be expressed in the range-Doppler domain as

$$s_{rd} = C(\tau, f_\eta) \cdot \exp\left(-j\frac{4\pi f_0 R_0 D(f_\eta)}{c_0}\right) \tag{2.32}$$

where $C(\tau, f_\eta)$ is a complex function which includes the signal limits in range and azimuth. The azimuth chirp is range dependent, so the matched filter is recalculated for each range bin. The filter is applied by multiplying the signal by

$$H_{az} = \exp\left(j\frac{4\pi R_0 D(f_\eta)}{\lambda}\right). \tag{2.33}$$

An inverse azimuth Fourier transform returns the signal to the time domain where the targets are now fully compressed. The quality of the focused image depends on how well the processing algorithm performs each step in forming the image. Approximations in deriving the signal model and other variations from the ideal signal can cause degradation in image quality. The main work of this dissertation is in defining the degradations due to algorithmic approximations and non-ideal platform motion and in developing a generalized approach to improve image focusing under such degrading conditions.

In Fig. 2.6, X-band SAR data from BYU's NuSAR-B is shown at different steps in the image formation process. The fully compressed image was formed using the CSA.
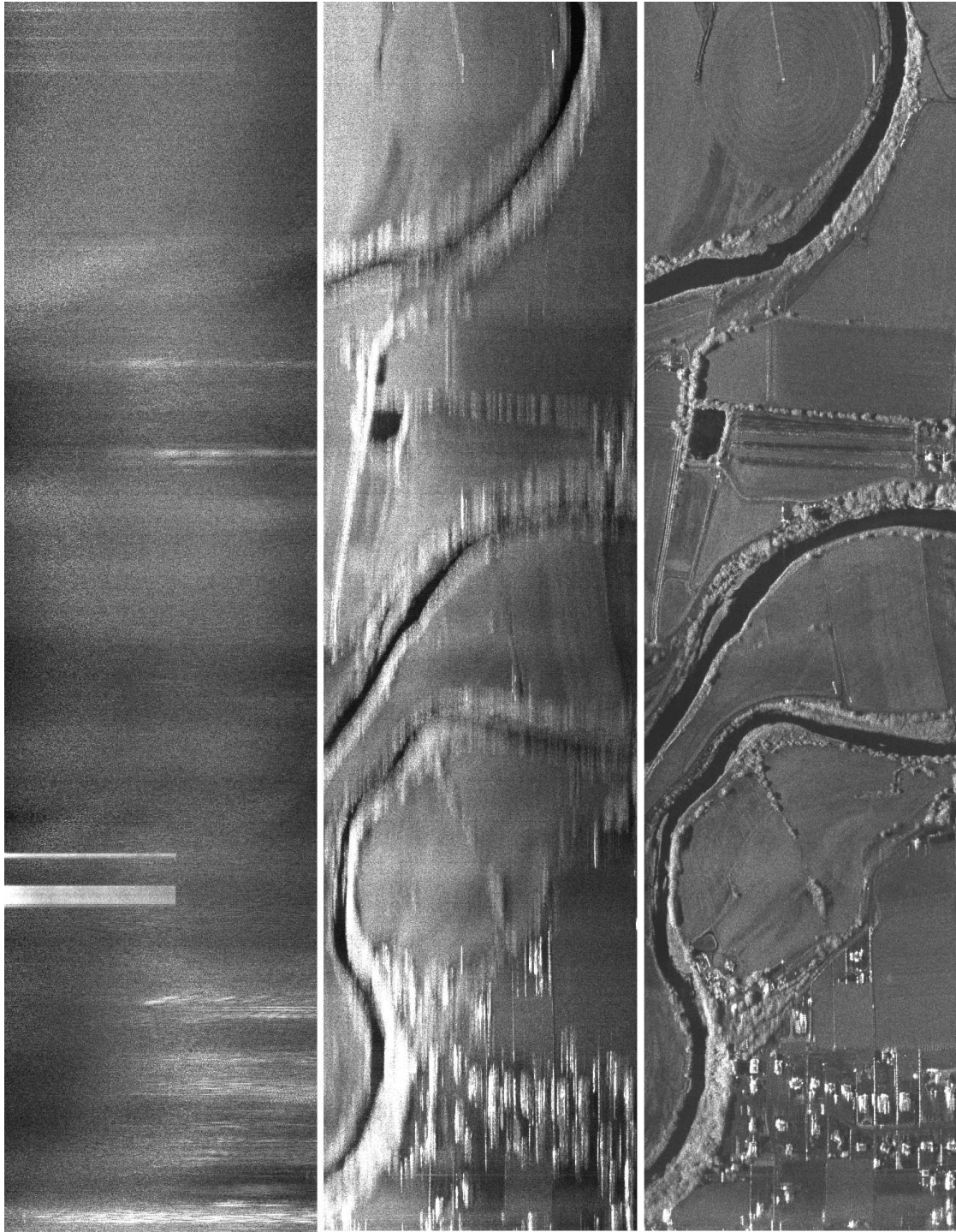
Figure 2.6: NuSAR-B X-band data collected over agricultural areas and the Bear River near Elwood and Honeyville, Utah. From left to right the images show the magnitude of the raw data, the magnitude of the range compressed data, and the magnitude of the azimuth compressed data, respectively.

26

CHAPTER 3.   GENERALIZED FREQUENCY DOMAIN PROCESSING FOR PULSED SAR

New synthetic aperture radar systems operating with wide bandwidths at low frequencies [9, 10, 11, 12] attract attention due to the potential for improving the data quality of existing applications and investigating new uses [13, 14, 15, 16, 17, 18]. At low frequencies the approximations made in formulating a number of SAR processing algorithms, such as the Range-Doppler Algorithm (RDA) and the Chirp Scaling Algorithm (CSA), are no longer valid [19, 20]. Some of the errors caused by many of these approximations have been addressed, together with suggested remedies, in previous work:

In [21], the need for compensating for neglected higher order terms is recognized and a third-order chirp-scaling term is introduced. In [22] the SAR signal model is derived to include a third-order term. A range-scaling term is included in [23] which controls the bandwidth increase associated with chirp-scaling. The quartic-phase algorithm of [24] extends these concepts by including a fourth-order term. The approximation errors are handled with the backprojection algorithm in [25] while in [26] the result of errors is treated with a modified filter after azimuth compression. Each of these papers improves the processing methods, extending their utility by providing the ability to process data with a specific set of parameters which extend beyond the capacity of previously existing methods, but none of the methods are generally applicable.

There is also another issue at low frequencies. The wider beamwidth required for high azimuth resolution causes problems with the center beam approximation used in motion compensation [26, 27] and in the chirp scaling process used in the CSA [28]. More advanced methods are thus required for processing low-frequency, wide beamwidth SAR data.

Processing for low frequency SAR has typically been approached with inversion methods such as the Fourier-Hankel [29] and the wavenumber domain Omega-K (ω-k) [30, 31, 32] algorithm or time-domain processing methods [33, 34, 35]. These methods avoid the approx-

imations that make RDA and CSA problematic at low frequencies and wide beamwidths, but unfortunately, they are more complex and computationally burdensome. The ω-k processing requires a costly interpolation to perform the Stolt mapping, and the algorithm makes it difficult to implement range-dependent motion compensation. Time-domain methods can be very precise for all SAR configurations, but are even more inefficient. Specialized hardware, such as graphics processing units (GPUs), has been shown to accelerate time-domain SAR and tomographic SAR processing [36]. While efforts have been made to modify the CSA to efficiently handle the effects of wide aperture [26], to extend the ω-k algorithm to handle range-dependent motion compensation [30, 37, 38], and to streamline the time-domain methods [34, 35], the common frequency-domain methods (RDA and CSA) are still widely used, despite their limitations, because of their simplicity and processing efficiency.

It is desireable to have an efficient general processing method usable with a wide variety of SAR data collected in a variety of circumstances. Such a method is developed in this chapter. Building on previous work, the limits of valid processing for frequency-domain methods are explored, and a generalized chirp-scaling SAR processing algorithm (the GCSA) that efficiently extends the utility of frequency-domain processing for SAR systems with wide beamwidths, large bandwidths, and low frequencies is proposed. The developed method is a new advancement in SAR processing theory and has the benefits of being straightforward and efficient with the capacity to form high quality images from a wide variety of SAR data. It fills the gap in image quality and processing time between the approximate and efficient algorithms and the precise but computationally taxing methods.

In Section 3.1, the general SAR signal in the two-dimensional frequency domain is derived. In Section 3.2, the approximations made to this signal are analyzed. For approximations of an arbitrary number of terms, an expression is derived for the phase error at any point in the frequency support band. Simulated data is used to analyze the effects that these phase errors have on image focusing with different order approximations and varying SAR parameters. Section 3.3 provides a guideline for determining the number of terms in the approximation required for properly focusing the SAR image. Finally, a generalized chirp-scaling SAR processing algorithm is derived that includes the appropriate number of terms.

3.1 The General SAR Signal

For our analysis, we consider only the phase functions of the SAR signal, ignoring the initial phase. As in the development presented in [8], we can describe the phase of the demodulated baseband SAR signal as

$$\Phi_0 = -4\pi f_0 R(\eta)/c + \pi K_r (\tau - 2R(\eta)/c)^2 \tag{3.1}$$

where f_0 is the carrier frequency. $R(\eta)$ is the range to a given target at slow time η. K_r is the range, or fast time, chirp rate and τ is fast time.

The first term describes the azimuth modulation: it consists of the phase left over after demodulation. It is purely a function of the carrier frequency and the changing range to a target. The second term in Eq. (3.1) is the transmit chirp delayed by the two-way travel time to the target. If we were to reduce the bandwidth to a single frequency, the second term would go to zero, but we would still have the same azimuth modulation.

The approximations made in many SAR processing algorithms are calculated in the wavenumber, or two-dimensional frequency domain. The derivation of the general SAR signal in the wavenumber domain, as found in subsection 3.1.1, results in

$$\Phi_{1RA} = -\frac{4\pi R_0 f_0}{c} \sqrt{D^2(f_\eta) + \frac{2f_\tau}{f_0} + \frac{f_\tau^2}{f_0^2}} - \frac{\pi f_\tau^2}{K_r} \tag{3.2}$$

where

$$D(f_\eta) = \sqrt{1 - \frac{c^2 f_\eta^2}{4v^2 f_0^2}}, \tag{3.3}$$

R_0 is the range of closest approach, f_τ is range frequency, and f_η is azimuth frequency.

Eq. (3.2) is the phase of the SAR signal in the wavenumber domain. For a target at a given range R_{ref}, the target can be ideally focused with the reference function multiply

$$H_{RFM} = \frac{4\pi R_{ref} f_0}{c} \sqrt{D^2(f_\eta) + \frac{2f_\tau}{f_0} + \frac{f_\tau^2}{f_0^2}} + \frac{\pi f_\tau^2}{K_r}. \tag{3.4}$$

This works regardless of squint, beamwidth, and chirp bandwidth.

3.1.1 Derivation of General SAR Signal in the Wavenumber Domain

For completeness, a summary of the derivation of the SAR signal in the wavenumber domain that is presented by Cumming and Wong in [8] is included in this subsection. The derivation consists of taking the range and azimuth Fourier transforms of Eq. (3.1). We approximate the Fourier transforms using the principle of stationary phase (POSP), which is valid except in the extreme case of having radar frequencies very close to zero.

An expression for the signal phase after the range Fourier transform is computed by adding the phase term $-2\pi f_\tau \tau$ to Eq. (3.1), where f_τ is range frequency:

$$\Phi_{0r} = \frac{-4\pi f_0 R(\eta)}{c} + \pi K_r \left[\tau - \frac{2R(\eta)}{c} \right]^2 - 2\pi f_\tau \tau. \tag{3.5}$$

Take the derivative of the phase with respect to τ, and solve for τ at the point where the phase is stationary (i.e. where $d\Phi_{0r}/d\tau = 0$).

$$\frac{d\Phi_{0r}}{d\tau} = 2\pi K_r \left[\tau - \frac{2R(\eta)}{c} \right] - 2\pi f_\tau = 0, \tag{3.6}$$

$$\tau = \frac{f_\tau}{K_r} + \frac{2R(\eta)}{c}. \tag{3.7}$$

Substitute into Eq. (3.5) and simplify to obtain the signal phase after the range Fourier transform of the signal.

$$
\begin{aligned}
\Phi_{1R} &= \frac{-4\pi f_0 R(\eta)}{c} + \frac{\pi f_\tau^2}{K_r} - 2\pi f_\tau \left(\frac{2R(\eta)}{c} + \frac{f_\tau}{K_r} \right) \\
&= \frac{-4\pi f_0 R(\eta)}{c} - \frac{\pi f_\tau^2}{K_r} + \frac{-4\pi f_\tau R(\eta)}{c} \\
&= \frac{-4\pi (f_0 + f_\tau) R(\eta)}{c} - \frac{\pi f_\tau^2}{K_r}.
\end{aligned} \tag{3.8}
$$

We now expand the range to the target $R(\eta)$

$$R(\eta) = \sqrt{R_0^2 + v^2 \eta^2} \tag{3.9}$$

where R_0 is the range of closest approach, and v is the velocity.

$$\Phi_{1R} = \frac{-4\pi(f_0 + f_\tau)\sqrt{R_0^2 + v^2\eta^2}}{c} - \frac{\pi f_\tau^2}{K_r}. \tag{3.10}$$

In order to evaluate the phase signal after the azimuth Fourier transform, again the POSP is used. Building the azimuth Fourier transform adds the term $-2\pi f_\eta \eta$ to the signal phase. Then the first derivative with respect to η is set to zero and solved for η.

$$\Phi_{1Ra} = \frac{-4\pi(f_0 + f_\tau)\sqrt{R_0^2 + v^2\eta^2}}{c} - \frac{\pi f_\tau^2}{K_r} - 2\pi f_\eta \eta, \tag{3.11}$$

$$\frac{d\Phi_{1Ra}}{d\eta} = \frac{-4\pi f_0 v^2 \eta}{c\sqrt{R_0^2 + v^2\eta^2}} + \frac{-4\pi f_\tau v^2 \eta}{c\sqrt{R_0^2 + v^2\eta^2}} - 2\pi f_\eta = 0, \tag{3.12}$$

$$
\begin{aligned}
\eta &= -\frac{c f_\eta R_0}{v\sqrt{-f_\eta^2 c^2 + 4v^2 f_0^2 + 8v^2 f_0 f_\tau + 4v^2 f_\tau^2}} \\
&= -\frac{c f_\eta R_0}{2(f_0 + f_\tau)v^2\sqrt{1 - \frac{c^2 f_\eta^2}{4v^2(f_0 + f_\tau)^2}}}.
\end{aligned}
\tag{3.13}
$$

Substitute this into Eq. (3.11) and simplify with some algebraic manipulation to get the phase of the SAR signal in the wavenumber domain.

$$
\begin{aligned}
\Phi_{1RA} &= -\frac{4\pi(f_0 + f_\tau)\sqrt{R_0^2 + \frac{v^2 c^2 R_0^2 f_\eta^2}{(f_0+f_\tau)^2 v^4 \; 4 - \frac{f_\eta^2 c^2}{v^2(f_0+f_\tau)^2}}}}{c} + \frac{\pi c R_0 f_\eta^2}{(f_0 + f_\tau)v^2\sqrt{1 - \frac{c^2 f_\eta^2}{4v^2(f_0+f_\tau)^2}}} - \frac{\pi f_\tau^2}{K_r} \\
&= -\frac{4\pi R_0(f_0 + f_\tau)}{c\sqrt{1 - \frac{c^2 f_\eta^2}{4v^2(f_0+f_\tau)^2}}} + \frac{\pi c R_0 f_\eta^2}{(f_0 + f_\tau)v^2\sqrt{1 - \frac{c^2 f_\eta^2}{4v^2(f_0+f_\tau)^2}}} - \frac{\pi f_\tau^2}{K_r} \\
&= -\frac{4\pi R_0(f_0 + f_\tau)}{c}\sqrt{1 - \frac{c^2 f_\eta^2}{4v^2(f_0 + f_\tau)^2}} - \frac{\pi f_\tau^2}{K_r} \\
&= -\frac{4\pi R_0 f_0}{c}\sqrt{D^2(f_\eta) + \frac{2f_\tau}{f_0} + \frac{f_\tau^2}{f_0^2}} - \frac{\pi f_\tau^2}{K_r}
\end{aligned}
\tag{3.14}
$$

where

$$D(f_\eta) = \sqrt{1 - \frac{c^2 f_\eta^2}{4v^2 f_0^2}}, \tag{3.15}$$

and f_η is azimuth frequency.

3.2 SAR Approximations

The CSA and RDA make approximations to Eq. (3.2) which break down at low-frequencies, large beamwidths, and large bandwidths. The ω-k algorithm can be a good choice in these situations because it uses the exact representation of Eq. (3.2) and applies Eq. (3.4) for a reference range while Stolt interpolation corrects for other ranges. This precision comes at the cost of increased complexity and for precise Stolt interpolation, the processing time increases compared to the CSA and RDA. Also, the ability to apply range-dependent motion compensation is hindered with the ω-k algorithm [30, 38].

The CSA and RDA approximations are formed using a Taylor series approximation of Eq. (3.2). The square root term can be expanded as

$$\Upsilon(f_\tau) = \sqrt{D^2(f_\eta) + \frac{2f_\tau}{f_0} + \frac{f_\tau^2}{f_0^2}} \approx \Upsilon(0) + \frac{\Upsilon'(0)}{1!}f_\tau + \frac{\Upsilon''(0)}{2!}f_\tau^2 + \frac{\Upsilon'''(0)}{3!}f_\tau^3 \cdots. \tag{3.16}$$

The RDA keeps only the 0th order term,

$$\Phi_{RDA} \approx -\frac{4\pi R_0 f_0}{c} \cdot [D(f_\eta)] - \frac{\pi f_\tau^2}{K_r}, \tag{3.17}$$

which makes the algorithm relatively simple. The first term of Eq. (3.17) is the azimuth modulation, corrected in the range-Doppler domain during azimuth compression. The second term is the chirp modulation corrected in the range compression step. Range-cell migration (RCM) correction is an interpolation that makes up for the neglected first order RCM term while the secondary range compression potentially compensates for neglected higher order terms.

32

The CSA keeps up to the second order term [8, 39],

$$\Phi_{CSA} \approx -\frac{\pi f_\tau^2}{K_r} - \frac{4\pi R_0 f_0}{c_0}\left[D(f_\eta) + \frac{f_\tau}{f_0 D(f_\eta)} + \frac{D^2(f_\eta) - 1}{2f_0^2 D^3(f_\eta)}f_\tau^2\right], \tag{3.18}$$

as shown inside the square brackets; the first term is the azimuth modulation, the second term is the range-cell migration, and the third term is cross-coupling between the range and azimuth frequencies. Important variations of the CSA have been introduced to address the limitations of this approximation. In the extended CSA of [21], a third-order chirp-scaling term is introduced for high squint with integrated motion compensation. Then in [22], the non-linear chirp-scaling algorithm is derived which includes a third-order SAR signal model, phase filter, and chirp-scaling parameter. The latter two are carefully chosen such that the range-dependence of the range-cell-migration (RCM) and secondary-range-compression (SRC) is eliminated. Another modification to the extended CSA in [23] is the inclusion of a range-scaling term which controls the bandwidth increase associated with chirp-scaling. Finally the quartic-phase algorithm [24] extends these concepts including a fourth-order phase filter and chirp-scaling parameter, a range-scaling term, and an improved model of range-dependence for SRC.

These algorithms are based on specific order approximations, but more generally, we can expand Eq. (3.16) to an arbitrary number of terms:

$$\begin{aligned}
\Upsilon(f_\tau) \approx\ & D(f_\eta) + \frac{f_\tau}{f_0 D(f_\eta)} + \frac{D^2(f_\eta) - 1}{2f_0^2 D^3(f_\eta)}f_\tau^2 - \frac{D^2(f_\eta) - 1}{2f_0^3 D^5(f_\eta)}f_\tau^3 \\
& -\frac{5 - 6D^2(f_\eta) + D^4(f_\eta)}{8f_0^4 D^7(f_\eta)}f_\tau^4 + \frac{7 - 10D^2(f_\eta) + 3D^4(f_\eta)}{8f_0^5 D^9(f_\eta)}f_\tau^5 \\
& +\frac{-21 + 35D^2(f_\eta) - 15D^4(f_\eta) + D^6(f_\eta)}{16f_0^6 D^{11}(f_\eta)}f_\tau^6 \\
& -\frac{-33 + 63D^2(f_\eta) - 35D^4(f_\eta) + 5D^6(f_\eta)}{16f_0^7 D^{13}(f_\eta)}f_\tau^7\dots
\end{aligned} \tag{3.19}$$

The phase error due to this approximation can be expressed

$$\begin{aligned}
\Phi_{Error} &= \Phi_{1RA} + \frac{\pi f_\tau^2}{K_r} + \frac{4\pi R_0 f_0}{c} \cdot \Upsilon(f_\tau) & (3.20) \\
&= -\frac{4\pi R_0 f_0}{c} \cdot \left(\sqrt{D^2(f_\eta) + \frac{2f_\tau}{f_0} + \frac{f_\tau^2}{f_0^2}} - \Upsilon(f_\tau) \right)
\end{aligned}$$

which is a function of four parameters:

1. range to target, R_0

2. center frequency, f_0

3. range frequency, f_τ, and

4. azimuth frequency, f_η.

The phase error gets larger when the range increases, the center frequency decreases, the maximum range frequency increases, and/or the maximum azimuth frequency increases.

The limits of f_τ are determined by the chirp bandwidth. For a chirp centered at zero after demodulation, the maximum and minimum f_τ are plus and minus half the bandwidth. For a chirp starting at zero, the maximum f_τ is the bandwidth. Thus as the bandwidth increases, the maximum f_τ increases. A larger f_τ means a larger approximation phase error in Eq. 3.20.

The maximum and minimum azimuth frequencies are a function of the beamwidth θ and squint ϑ,

$$\begin{aligned}
f_{\eta MAX} &= 2\frac{f_0}{c} v \sin\left(\frac{\theta}{2} + \vartheta\right), & (3.21) \\
f_{\eta MIN} &= 2\frac{f_0}{c} v \sin\left(-\frac{\theta}{2} + \vartheta\right). & (3.22)
\end{aligned}$$

f_η is only used in Eq. 3.20 as part of $D(f_\eta)$, which can be rewritten at maximum f_η as

$$D(f_{\eta MAX}) = \sqrt{1 - \sin^2\left(\frac{\theta}{2} + \vartheta\right)}, \qquad (3.23)$$

thus the azimuth frequency dependence of the phase error in Eq. 3.20 is dependent on the beamwidth and independent of velocity and PRF.

Simulated data are used to demonstrate how changing the radar parameters affects the azimuth focusing. A nominal choice of SAR parameters is chosen, with images created with no approximations and with the CSA approximations. The four parameters that affect the phase error are individually varied to demonstrate how the focusing changes with these parameters. The initial radar parameters are a center frequency of 1.75 GHz, a bandwidth of 500 MHz centered at zero, an altitude of 3050 meters, and a beamwidth 19.3° wide. An image of a single point target, ideally processed using Eq. 3.2 without approximations (ω-k algorithm), is shown in Fig. 3.1. The same data processed with the CSA (second order approximation) is shown in Fig. 3.2.

The CSA was used in producing Figs. 3.3-3.6, which show the results of changing, respectively, the range to target, the center frequency, the chirp bandwidth, and the antenna beamwidth. The azimuth resolution changes with center frequency and beamwidth, Fig. 3.7 shows two examples of changing the beamwidth and center frequency to keep the along-track resolution the same. The results from these figures are summarized in Table 3.1.

3.3 SAR Processing Generalization

For any given set of SAR system parameters, a generalized frequency-domain SAR processor must:

1. Determine the number of terms (order) from Eq. (3.19) that is required for proper focusing

2. Efficiently process the data taking into account those terms.

Table 3.1:
Summary of the simulation processing parameters and results for Figs.3.1-3.7. The "Defocus Factor" is the percent increase in measured azimuth resolution over the theoretical azimuth resolution. The theoretical azimuth resolution for an unweighted aperture is $(0.89 \cdot c/(4 f_0 sin(\theta/2)))$.

Fig.	Range to Target (m)	Center Frequency (GHz)	Chirp Bandwidth (MHz)	Antenna Beam-width (°)	Theoretical Azimuth Resolution (m)	Measured Azimuth Resolution (m)	Defocus Factor (%)	Percent of Phase Error Greater Than $\pi/10$ (%)
3.1	3053.2	1.75	500	19.3	22.6	22.6	0.0	0.0
3.2	3053.2	1.75	500	19.3	22.6	29.0	28.1	41.0
3.3	1531.4	1.75	500	19.3	22.6	24.5	8.3	31.2
	6101.6	1.75	500	19.3	22.6	32.0	41.5	50.1
3.4	3053.2	1.5	500	19.3	26.4	33.9	28.5	45.2
	3053.2	2	500	19.3	19.8	31.9	41.1	37.3
3.5	3053.2	1.75	250	19.3	22.6	23.7	4.6	11.4
	3053.2	1.75	500	19.3	22.6	31.2	37.9	67.0
3.6	3053.2	1.75	500	9.6	45.5	47.3	3.9	20.8
	3053.2	1.75	500	29.0	15.1	25.1469	66.4	51.7
3.7	3053.2	1.5	500	22.5	22.6	30.6	35.4	49.2
	3053.2	2	500	16.9	22.6	27.6	22.1	33.4

Figure 3.1: Simulated SAR data of a single point target at a range of 3053.2 m, a center frequency of 1.75 GHz, a chirp bandwidth of 500 MHz and an antenna beamwidth of 19.3°, ideally processed without approximations (ω-k, Eq. (3.4)). The left-most plot is a magnitude image of the focused target. The next figure is a contour plot with contours spaced 3dB apart. The next plot is a range slice through the center of the target, plotted in dB, the azimuth resolution is measured at the 3 dB point of this figure. The right-most image shows the phase error over the support band due as in Eq. (3.20). The parameters and results for this data are summarized in Table 3.1.

Figure 3.2: Simulated SAR data of a single point target at a range of 3053.2 m, a center frequency of 1.75 GHz, a chirp bandwidth of 500 MHz and an antenna beamwidth of 19.3°, processed using the CSA (2nd order approximation). The plots are arranged as in Fig. 3.1. Parameters and results are summarized in Table 3.1.

3.3.1 Required Order Determination

One approach to accomplishing the first step is by considering the phase error from Eq. (3.20). This error can be viewed and analyzed by computing the error for every point in the support band in the two-dimensional frequency domain. Phase errors greater than a few tenths of a radian indicate that a portion of the data is being processed incorrectly. We choose a threshold of $\pi/10$ to be excess error. The portion of the support band with phase errors greater than $\pi/10$ can be used to predict the focusing accuracy of a target. This percentage is calculated for each example in Table 3.1 and the results are shown in Fig. 3.8. From this graph we decide on a guideline: if less than 30% of the support band has a phase

Figure 3.3: Simulated SAR data of a single point target at ranges of 1531.4 m (top) and 6101.6 m (bottom), a center frequency of 1.75 GHz, a chirp bandwidth of 500 MHz and an antenna beamwidth of 19.3°, processed using the CSA. The plots are ordered as in Fig. 3.1. Compared to Fig. 3.2, the measured azimuth resolution improves at shorter range and worsens at longer range.

error greater than $\pi/10$, then one can predict less than a 20% loss in azimuth resolution defocusing. Depending on error tolerances of a given application, 20% loss of focus could be inadequate. In that case, processing the data with more of the higher order terms from Eq. (3.19) is advised.

If the third-order terms are included in processing the data from Fig. 3.2, the percentage of phase errors greater than $\pi/10$ drops to 10.6% and the focusing is indistinguishable from the the ideal (1.9% defocus), as shown in Fig. 3.9. Dropping the frequency to 1.25 GHz and increasing the beamwidth to 27.1° maintains the theoretic azimuth resolution of 22.6 cm, but the percentage of phase errors greater than $\pi/10$ increases to 31.2%, and Fig. 3.10 shows that the focusing decreases by 16.7%, which is expected based on the guidelines of Fig. 3.8.

As another example, data is simulated with a center frequency of 800 MHz, a bandwidth of 500 MHz, a beamwidth of 40.3°, and range to target 1755.6 m. The data is repeatedly processed with terms of increasing order. The results are shown in Fig. 3.13 and summarized in Table 3.2. Again we find that the defocusing is reduced to about 20% as the percent of phase error greater than $\pi/10$ drops to about 30%.

38

Figure 3.4: Simulated SAR data of a single point target at a range of 3053.2 m, a center frequency of 1.5 GHz (top) and 2.0 GHz (bottom), a chirp bandwidth of 500 MHz and an antenna beamwidth of 19.3°, processed using the CSA. The plots are arranged as in Fig. 3.1. Compared to Fig. 3.2, the different center frequencies cause a change in the theoretical azimuth resolution, with the higher frequency focusing more accurately.

The above guidelines give us an additional tool to be used in conjunction with simulations and other analysis techniques to suggest the order of the terms required for proper focusing. Efforts have been made to develop algorithms for efficiently processing data while keeping the higher order terms. As an example, from the algorithms mentioned in Section 3.2, the non-linear CSA algorithm of [22] keeps up to the 3rd order term of Eq. (3.19). Compared to the CSA, this method requires two additional range FFT's and a phase multiply. If terms higher than the 3rd order are needed for proper focusing, something more involved than the non-linear CSA is required. Such a method is derived below.

There is an upper bound for the number of approximation terms that can be used. An extreme situation is simulated with a center frequency of 350 MHz, a bandwidth of 500 MHz, an antenna beamwidth of 80°, and a range to target of 3003 m. Fig. 3.11 shows that the highest order approximation that yields the best results is the 6th order. Using terms higher than this are actually detrimental to the overall focusing. As seen in Fig. 3.12 and in Eq. (3.19), the higher order terms become increasingly important at the edges of the support band. The terms come in alternating positive and negative pairs which largely cancel each other out, and above the 6th order the terms are too unstable for practical use. With this
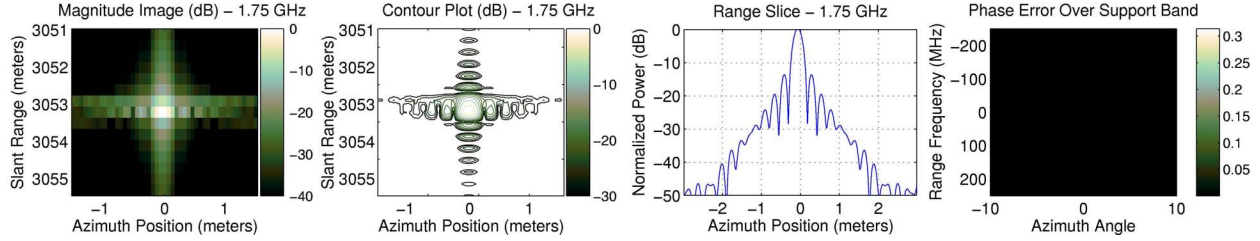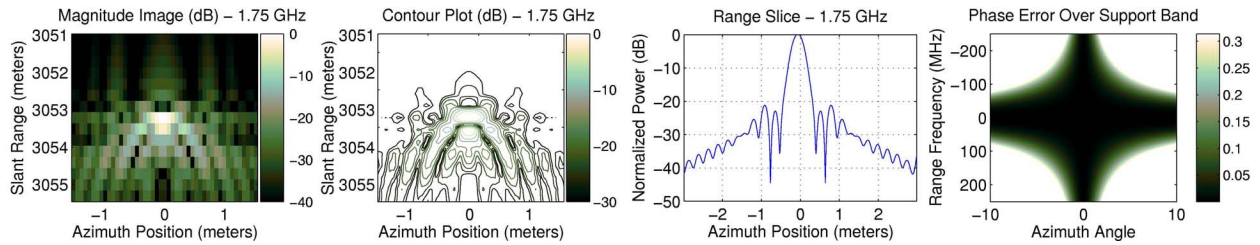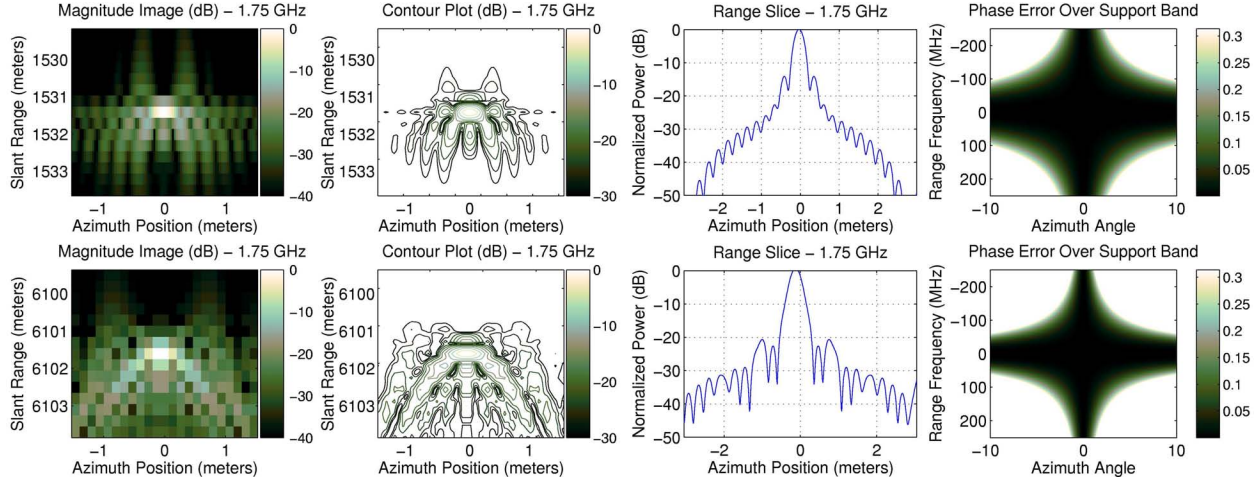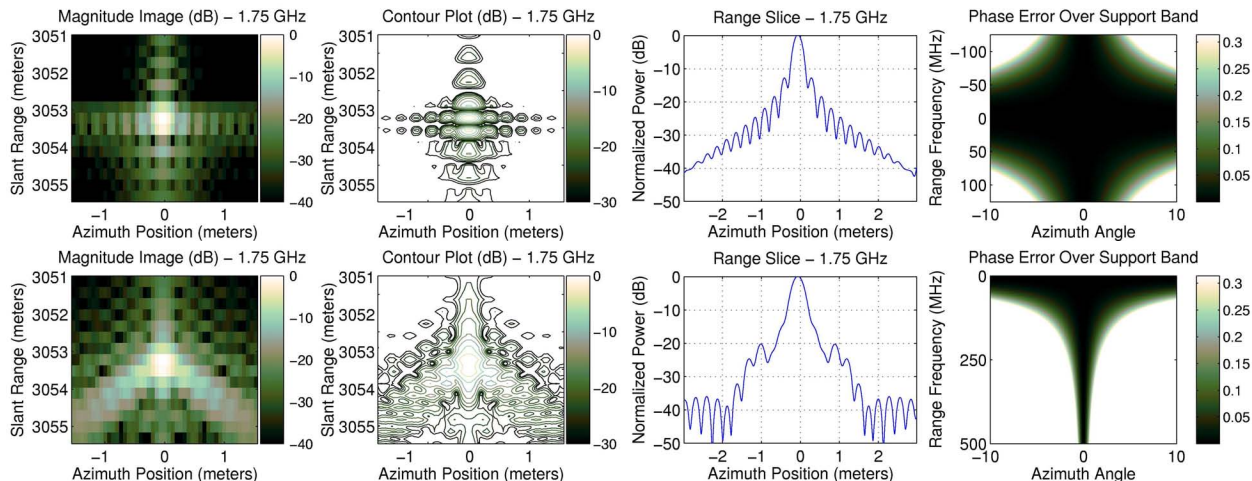
Figure 3.5: Simulated SAR data of a single point target at a range of 3053.2 m, a center frequency of 1.75 GHz, a chirp bandwidth of 250 MHz centered at zero (top) and 500 MHz centered at 250 MHz (bottom), and an antenna beamwidth of 19.3°, processed using the CSA. The plots are arranged as in Fig. 3.1. Compared to Fig. 3.2, the top figure shows an improvement in azimuth focusing with a loss in range resolution while the bottom image shows degraded azimuth focusing.

particular set of parameters, however, even when using the 6th order approximation, 61.6% of the support band has a phase error greater than $\pi/10$. Thus the generalized chirp-scaling approach is inadequate for focusing this data. This result suggests that there is a definite point at which SAR processing *requires* an ω-k or time-domain approach, in such cases, the generalized chirp-scaling approach should not be used.

3.3.2 Generalized SAR Processing Algorithm

The goal is to develop a new general processing scheme which efficiently accounts for as many higher order terms as dictated by the SAR parameters and the desired precision. Ideally, each additional term from Eq. (3.19) should add minimally to the computational burden. The algorithm derived below is summarized in Table 3.3. For order n, the high-order phase and chirp-scaling terms up to the n_{th} order are chosen such that the range dependence of the range-cell migration and range-frequency rate is reduced.
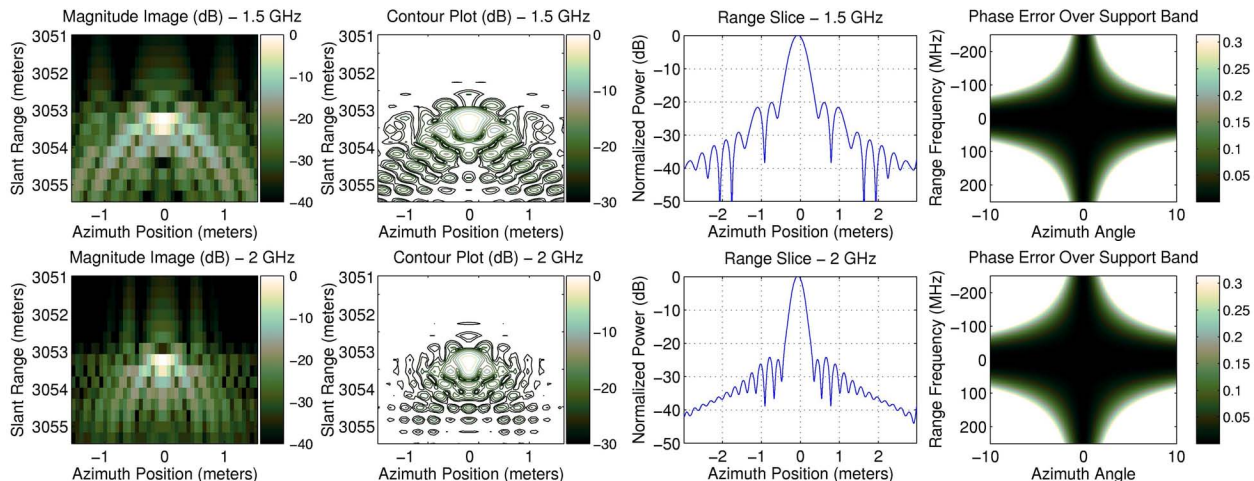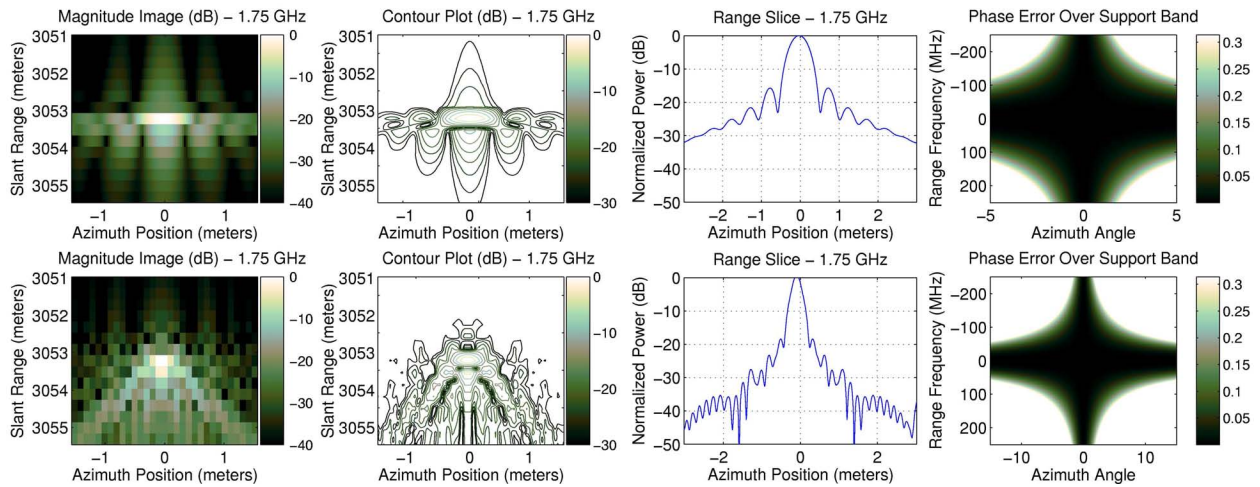
Figure 3.6: Simulated SAR data of a single point target at a range of 3053.2 m, a center frequency of 1.75 GHz, a chirp bandwidth of 500 MHz and an antenna beamwidth of 9.6° (top) and 29.0° (bottom), processed using the CSA. The plots are arranged as in Fig. 3.1. Compared to Fig. 3.2, the changing beamwidths cause a change in the theoretical azimuth resolution.
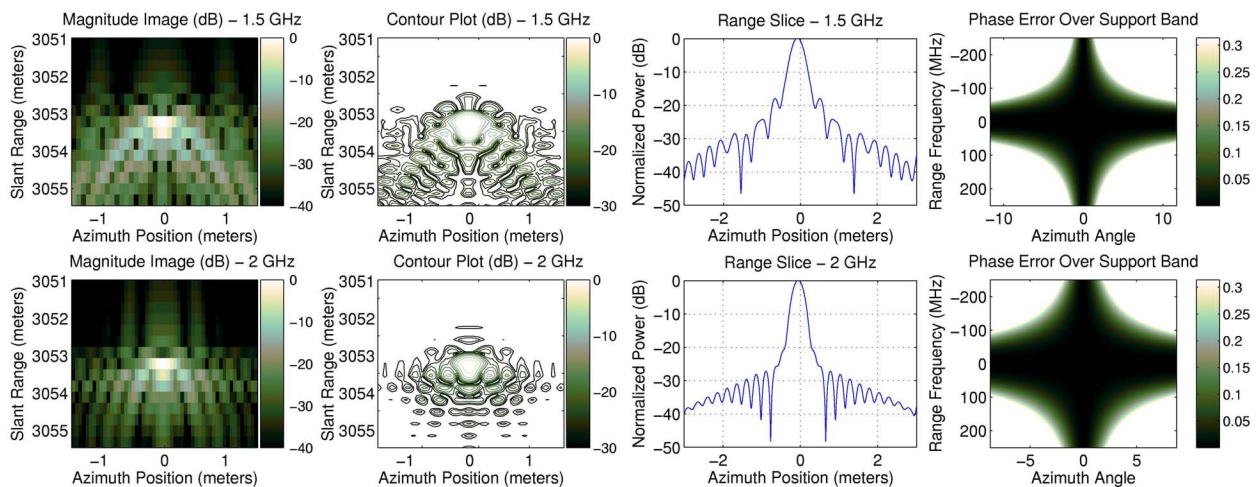
Figure 3.7: Simulated SAR data of a single point target at a range of 3053.2 m, and a chirp bandwidth of 500 MHz, processed using the CSA. The plots are arranged as in Fig. 3.1. To maintain the same theoretical azimuth resolution as Fig. 3.2, the center frequency and antenna beamwidth are both changed in these figures. The top row has a lower frequency (1.5 GHz) and larger beamwidth (22.5°) while the bottom row has a higher frequency (2.0 GHz) and smaller beamwidth (16.9°), with results in Table 3.1.
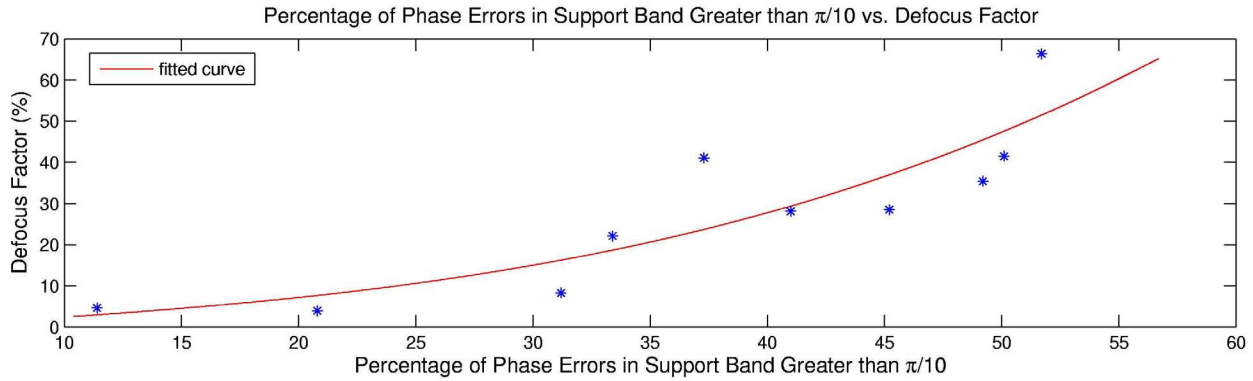
Figure 3.8: From the data in Table 3.1, the amount of defocusing is plotted versus the percentage of phase errors greater than $\pi/10$ in the support band. The general trend is emphasized with a fitted curve. From this we decide that in order to have less than a 20% loss in azimuth focus, the percentage of phase errors in the support band greater than $\pi/10$ should be less than 30%.
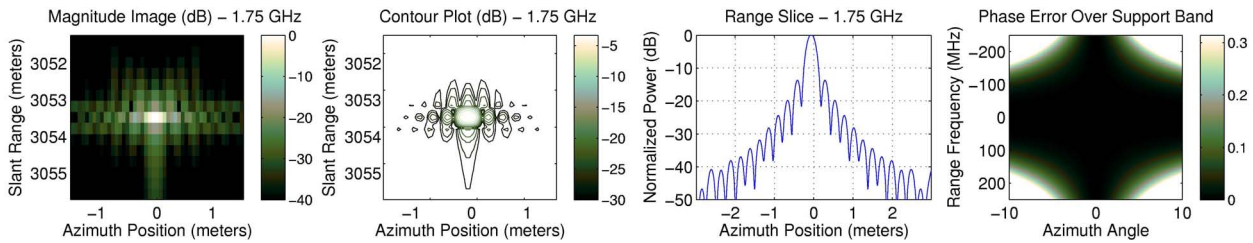
Figure 3.9: Simulated SAR data of a single point target identical to Fig. 3.2, processed including third order approximation terms. The measured azimuth resolution is 23.0 cm, essentially equivalent to the theoretic value of 22.6 cm.
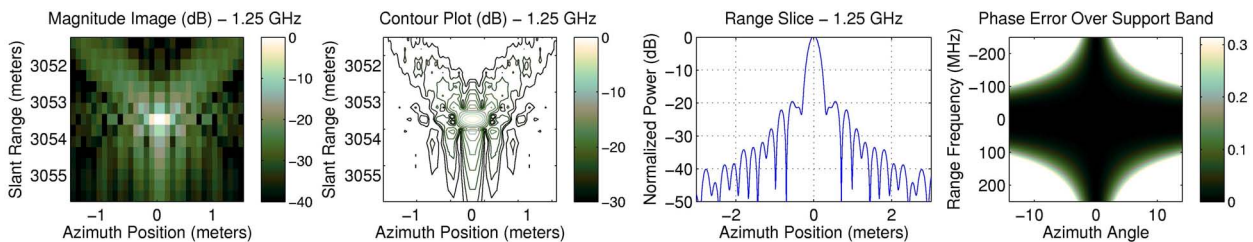
Figure 3.10: Simulated SAR data of a single point target with a center frequency of 1.25 GHz, a beamwidth of 27.1°, and a 500 MHz bandwidth, processed with third-order approximations. The percent of the support band with a phase error greater than $\pi/10$ is 31.2%, this results in a measured azimuth resolution of 26.8 cm, a 16.7% loss of focus.
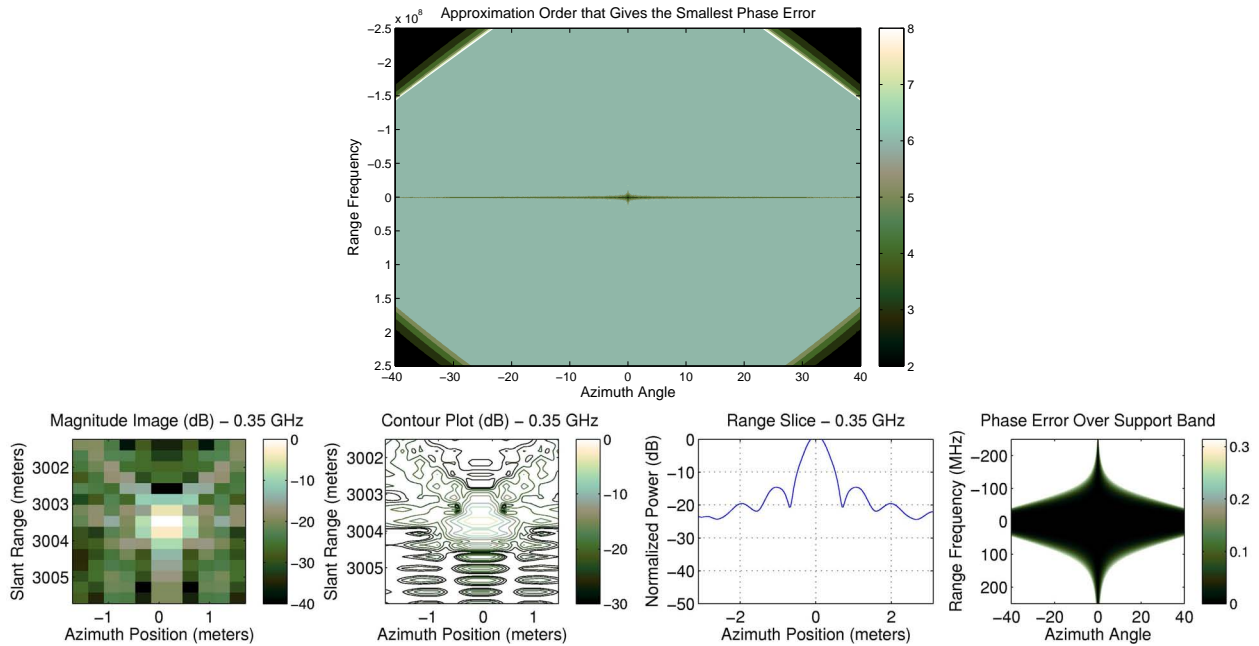
Figure 3.11: In an extreme SAR situation, with a center frequency of 350 MHz, a 500 MHz bandwidth, a 80° beamwidth, and a 3003 m range to target, the top plot shows the approximation order closest to ideal over the support band, or the approximation order with the smallest error at each point over the support band. Interestingly enough, the sixth-order approximation is the best over the usable area of the support band with higher-order approximations performing worse. The SAR data is processed using the 6th order approximation, but even so, 61.6% of the support band has a phase error greater than $\pi/10$, and the measured azimuth resolution is 59.6 cm, a 101.5% defocus from the theoretic resolution of 29.6 cm.
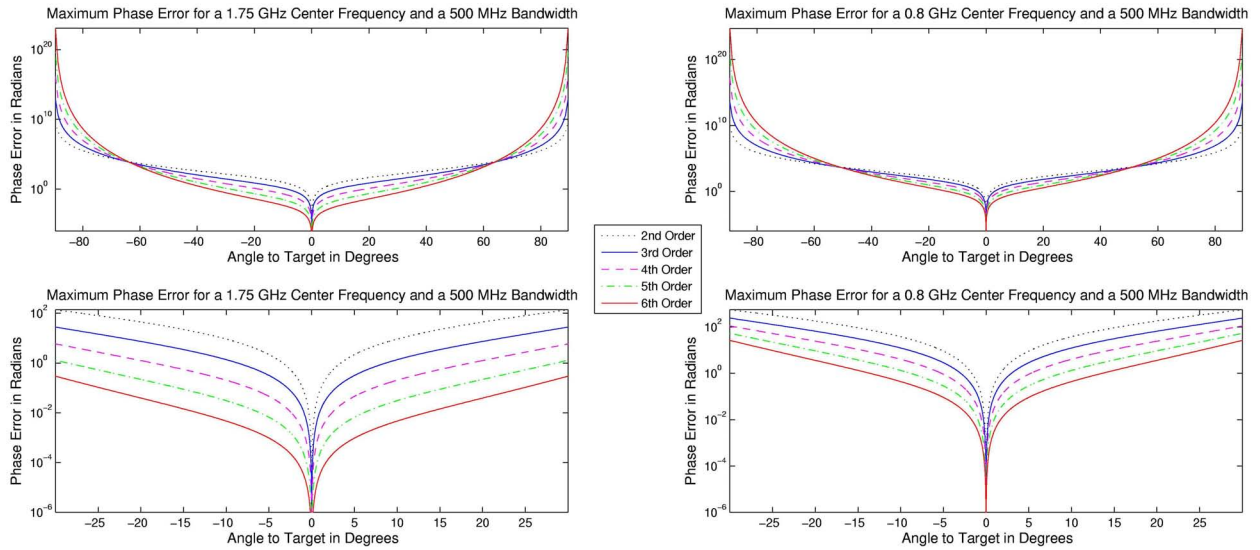
Figure 3.12: The maximum magnitude of the phase error for different order approximations, as given by Eq. (3.20) for a 500 MHz bandwidth at 1.75 GHz (left) and 800 MHz (right). The top row shows the errors out to the maximum beamwidth of 180° while the bottom row focuses on beamwidths up to 60°. As the center frequency decreases, higher order approximations are required, even at small beamwidths, to get small phase errors. In addition, at lower frequencies a much larger beamwidth is required to maintain the same azimuth resolution, making it doubly important to account for the higher order terms. At extreme values, the higher order terms become dominate, marking the boundary of utility for the generalized chirp-scaling approach.
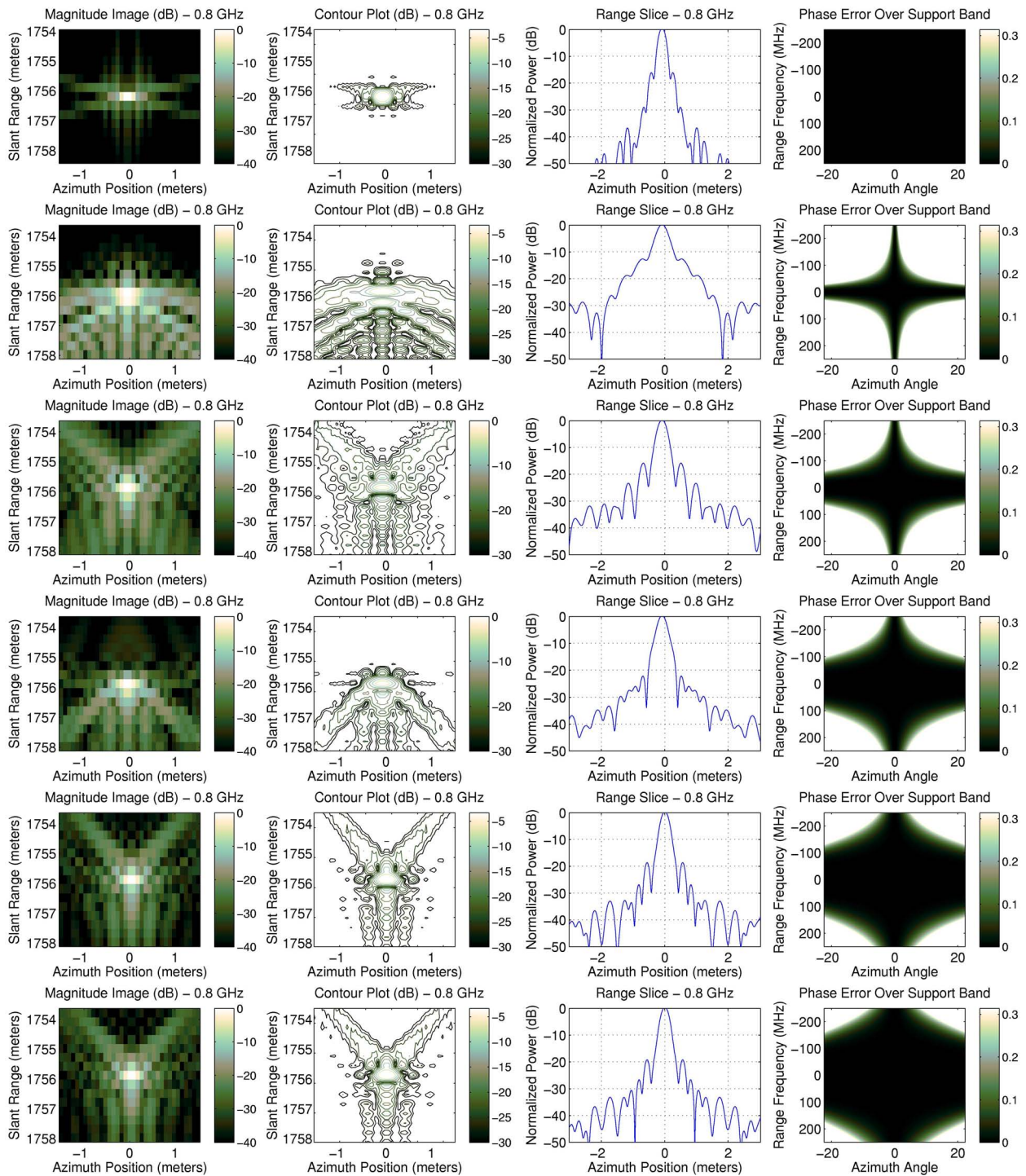
Figure 3.13: Simulated SAR data of a point target at the reference range with a center frequency of 800 MHz, a bandwidth of 500 MHz, a beamwidth of 40.3°, and range to target 1755.6 m. Approximation orders two through six and ideal processing are used with results summarized in Table 3.2. The top row shows ideal processing. Approximation orders two through six are shown in rows two through six respectively.
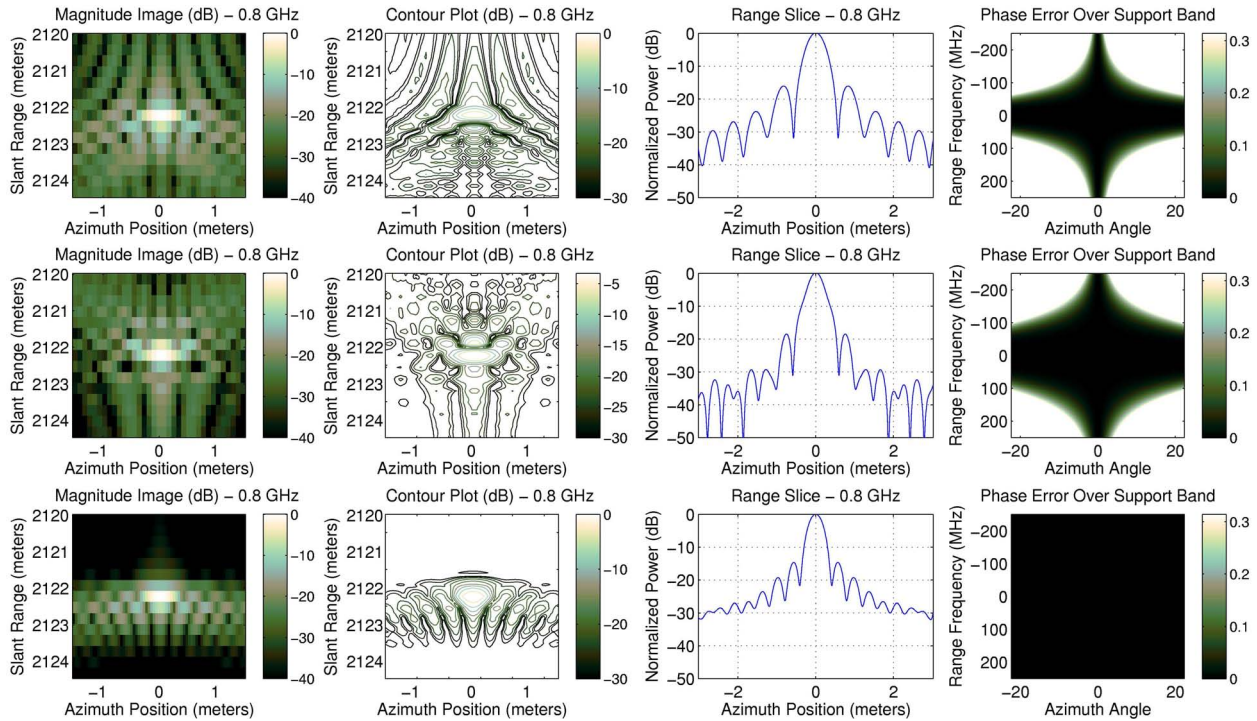
Figure 3.14: The processed image of a second point target from the simulations of Fig. 3.13 more than 300 m away from the reference range. The top figure shows this target after 3rd order processing, the middle figure shows the results of the 4th order processing, and the bottom figure shows the results of processing with the ω-k algorithm using cubic-spline interpolation for the Stolt mapping. The generalized processing is designed to reduce range dependence, demonstrated by the fact that the focusing of this target improves when processed with a higher-order approximation, however some range dependent errors persist as the focusing of these targets is degraded compared to Fig. 3.13. While not as striking, a similar range dependent defocusing is visible in the "ideal" ω-k image. The quality of focusing with the ω-k algorithm is highly dependent on the precision of the Stolt interpolation. This example demonstrates good focusing using a fairly accurate interpolation at the cost of much greater processing time (see Table 3.2).
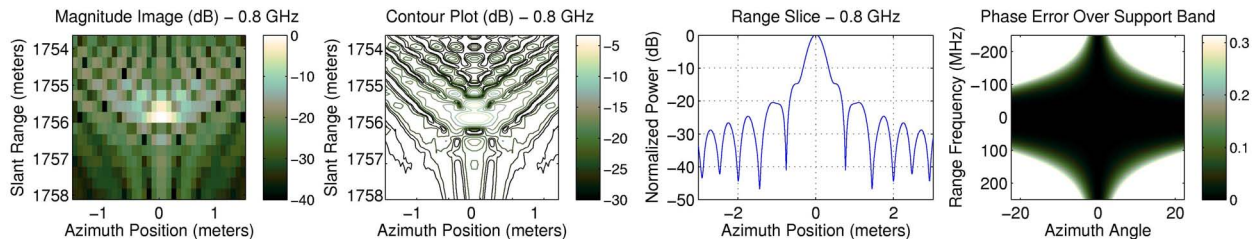
Figure 3.15: The same data from Fig. 3.13 processed with an approximation to the generalized algorithm, shown here is the 4th order results. A processing time savings of 30% comes at the cost of higher sidelobes.

Table 3.2: The Numerical Results from the Images in Fig. 3.13.

Approximation Order	Theoretic Azimuth Resolution (cm)	Measured Azimuth Resolution (cm)	Defocus Factor (%)	Percent of Phase Error Greater Than $\pi/10$ (%)	Processing Time as a multiple of CSA
2nd (CSA)	23.7	36.6	54.4	70.3	1
3rd	23.7	30.0	26.6	51.2	2.2
4th	23.7	29.1	22.7	33.9	3.6
5th	23.7	28.3	19.4	20.0	5.4
6th	23.7	27.7	16.8	10.1	7.2
Ideal	23.7	23.7	0.1	0.0	27.04

We start with the approximation of the phase of our signal in the two-dimensional frequency domain, Eq. (3.2), which we express as Φ_{SS} in row 4 of Table 3.3, where Υ_i is the ith derivative of $\Upsilon(f_\tau)$ evaluated at $f_\tau = 0$, as in Eq. (3.16).

This signal is multiplied by a higher-order phase filter, H_{HOPF} in row 5 of Table 3.3. The X_i terms are solved later in the derivation to reduce the range-dependence of the higher order terms.

The inverse range Fourier transform is approximated by the principle of stationary phase (POSP). Assuming the higher-order terms are small, as in [22, 24, 40], the signal in the range-Doppler domain can be shown to be Φ_{sSm} in row 6 of Table 3.3, where, as in [8, 22],

$$K_m = \frac{Kr}{1 - \frac{K_r c R_0 f_\eta^2}{2v^2 f_0^3 D^3(f_\eta)}} \tag{3.24}$$

and $\tau_d = (2R_0)/(cD(f_\eta))$. τ_d is the trajectory of a target with range of closest approach R_0.

The chirp-scaling is performed by a phase multiply of orders up through n. The chirp-scaling phase is H_{CS} in row 7 of Table 3.3, where the q_i's are the scaling coefficients, which we will solve for, and $\tau_{ref} = (2R_{ref})/(cD(f_\eta))$, which is the trajectory for a target at reference range R_{ref}.

After chirp-scaling the signal phase is Φ_{sSz} in row 8 of Table 3.3, where the first term is the along-track modulation, which we will ignore for the moment. The remaining terms, shown as the sum of C_i, are formed by making the substitutions

$$\tau_{ref} = \tau_s - \alpha \Delta\tau, \tag{3.25}$$

$$\tau_d = \tau_s - (\alpha - 1)\Delta\tau \tag{3.26}$$

where $\Delta\tau = (2(R_0 - R_{ref}))/(cD(f_\eta))$, the difference between τ_d and τ_{ref}, and α is a scaling term determined by the Doppler centroid, f_{dc},

$$\alpha(f_\eta) = \frac{\sqrt{1 - \frac{c^2 f_\eta^2}{4v^2 f_0^2}}}{\sqrt{1 - \frac{c^2 f_{dc}^2}{4v^2 f_0^2}}} \tag{3.27}$$

which simplifies to $D(f_\eta)$ when there is no squint. Carefully expanding the result, and reordering the terms as a series of $(\tau - \tau_s)$ yields

$$C_0 + C_1 (\tau - \tau_s) + C_2 (\tau - \tau_s)^2 \ldots C_n (\tau - \tau_s)^n \tag{3.28}$$

where C_i is defined as

$$
\begin{aligned}
C_0 &= C_{x0} + \pi K_m \Delta\tau^2 (\alpha - 1)^2 , \\
C_1 &= C_{x1} + 2\pi K_m (\alpha - 1) \Delta\tau, \\
C_2 &= C_{x2} + \pi K_m, \\
C_i &= C_{xi}, \quad \text{for } i > 2,
\end{aligned}
\tag{3.29}
$$

with

$$
\begin{aligned}
C_{xi} &= \sum_{h=i}^{n} \left(\frac{h!}{i!\,(h-i)!} \pi \left(\alpha\Delta\tau\right)^{(h-i)} q_h \right) \\
&+ \sum_{h=i}^{n} \left(\frac{2\pi K_m^i (\Delta\tau (\alpha - 1))^{h-i} \left(\frac{f_0 \Upsilon_h \left(2R_{ref} + \Delta\tau D(f_\eta)c \right)}{c} - \frac{h! X_h}{2} \right)}{i!\,(h-i)!} \right),
\end{aligned}
\tag{3.30}
$$

where $X_i = 0$ and $\Upsilon_i = 0$ for $i < 3$ and $q_i = 0$ for $i < 2$.

The range-dependent range frequency rate K_m is approximately expressed as the sum of K_f, which is K_m at a reference range, and $\Delta\tau$. We first define

$$K_s = -\frac{c^2 f_\eta^2}{4v^2 f_0^3 D^2(f_\eta)} \tag{3.31}$$

then equivalent to Eq. (3.24)

$$K_m = -\frac{K_f}{-1 + K_s \Delta\tau K_f}. \tag{3.32}$$

We Taylor-expand K_m in terms of $\Delta\tau$, and keep up to the second order,

$$K_m \approx K_f + K_s K_f^2 \Delta\tau + K_s^2 K_f^3 \Delta\tau^2. \qquad (3.33)$$

Each C_i, for $i > 0$, is expressed as a series of $\Delta\tau$, for example

$$
\begin{aligned}
C_1 = {}& 2\pi \left(\alpha K_f + q_2\alpha - K_f\right)\Delta\tau \qquad (3.34) \\
& + \left(\frac{\pi K_f^3 (\alpha - 1)^2 (2f_0\Upsilon_3 R_{ref} - 3X_3 c)}{c} + 2\pi K_s K_f^2 (\alpha - 1) + 3\pi q_3\alpha^2 \right) \Delta\tau^2 + \dots
\end{aligned}
$$

When the coefficients of $\Delta\tau$ are zero, the range variations are eliminated. For the linear and quadratic terms of $\Delta\tau$, setting them equal to zero results in $2n - 3$ equations for $2n - 3$ unknowns, for example

$$2\pi \left(\alpha K_f + q_2\alpha - K_f\right) = 0, \qquad (3.35)$$

$$\frac{\pi K_f^3 (\alpha-1)^2 \left(2f_0\Upsilon_3 R_{ref} - 3X_3 c\right)}{c} + 2\pi K_s K_f^2 (\alpha - 1) + 3\pi q_3\alpha^2 = 0,$$

$$\frac{\pi K_f^3 (\alpha-1) \left(2f_0\Upsilon_3 R_{ref} - 3X_3 c\right)}{c} + \pi K_s K_f^2 + 3\pi q_3\alpha = 0,$$

$$etc.$$

We solve for q_i and X_i in Table 3.4

The linear and quadratic terms of $\Delta\tau$ in each C_i for $i > 0$ become zero, while the higher order terms are very small and can be neglected. This results in the SAR signal phase being expressed as in the second part of row 8 of Table 3.3.

A range FFT takes the signal into the two-dimensional frequency domain, resulting in Φ_{SS2} in row 9 of Table 3.3. The signal is multiplied by a range matched filter, H_R in row 10 of Table 3.3.

A range inverse Fourier transform is then calculated, resulting in a signal with a phase that is compensated by an azimuth compression and residual phase compensation H_{az} in Table 3.3. An inverse azimuth Fourier transform results in the focused image.

This generalized method was applied in processing the data shown in Fig. 3.13 and Fig. 3.14. Significant improvements in focusing are seen, as detailed in Table 3.2.

Of note is the relationship of this algorithm with those previously developed. When $n = 2$, this algorithm simplifies to the CSA. When $n = 3$, it simplifies to the non-linear CSA [22], without the extra orbital geometry term. If the α term is coupled with a β term that scales the range bandwidth, so that everywhere there is an α it becomes $\alpha\beta$, then when $n = 2$ the algorithm simplifies to the extended CSA of [23]. Also, when $n = 4$ it simplifies to the QPA [24] with a note that our algorithm includes a 4th order signal model. The extended CSA, non-linear CSA and QPA were all specifically developed for squint mode processing, but it is not only squinting that can cause the low-order approximations to break down. The approximation error has been dealt with more generally in this chapter, but the method developed is well suited for squint-mode processing.

An approximation to the generalized algorithm that eliminates the extra range FFT and IFFT is obtained by, in Table 3.3, eliminating rows 3-6 and combining row 5 with row 10. An example is shown in Fig. 3.15, where it is plain to see that the focusing is similar, but the sidelobes are larger.

3.4 Summary

With new SAR systems pushing center frequencies lower, bandwidths larger, and beamwidths wider, the approximations used in common frequency-domain SAR processing algorithms are inadequate. By developing an expression for the phase error term and visualizing it over the two-dimensional frequency support band, analysis of the effects of varying the SAR parameters for a given approximation is enhanced. RDA and CSA are low-order approximations of ideal frequency domain processing. A generalized algorithm is herein developed. A set of guidelines is proposed to determine the required approximation order for proper image processing, for a given set of SAR parameters. An efficient frequency-domain algorithm, built upon the CSA framework, which accounts for higher order terms is used to increase the precision over existing algorithms. Together, these tools provide an attractive alternative to the ω-k and time-domain methods for processing wide-beamwidth, low-frequency, large-bandwidth SAR data.

Table 3.3: Nth-Order Generalized Chirp-Scaling Processing Flow

Action	Parameter Value
1. Digitize SAR Signal $\rightarrow e^{j\Phi_0}$	$\Phi_0 = -4\pi f_0 R(\eta)/c + \pi K_r(\tau - 2R(\eta)/c)^2$
2. Azimuth FFT	
3. Range FFT $\rightarrow e^{j\Phi_{1RA}}$	$\Phi_{1RA} = -\frac{4\pi R_0 f_0}{c}\sqrt{D^2(f_\eta) + \frac{2f_\tau}{f_0} + \frac{f_\tau^2}{f_0^2}} - \frac{\pi f_\tau^2}{K_r}$
4. Approximate Φ_{1RA} as Φ_{SS}	$\Phi_{SS} = -\pi f_\tau^2/K_r - 4\pi R_0 f_0/c \cdot \left[D(f_\eta) + \frac{f_\tau}{f_0 D(f_\eta)} + \frac{D^2(f_\eta)-1}{2f_0^2 D^3(f_\eta)} f_\tau^2 \right]$ $-\frac{4\pi R_0 f_0}{c} \cdot \sum_{i=3}^{n} \frac{\Upsilon_i}{i!} f_\tau^i$
5. $e^{j\Phi_{SS}} \times e^{j\cdot H_{HOPF}}$	$H_{HOPF} = \pi \cdot \sum_{i=3}^{n} X_i f_\tau^i$
6. Range IFFT $\rightarrow e^{j\Phi_{sSm}}$	$\Phi_{sSm} = \frac{-4\pi R_0 D(f_\eta) f_0}{c} + \pi K_m (\tau - \tau_d)^2$ $+ \sum_{i=3}^{n} \left(\frac{4\pi R_0 f_0}{c} \frac{\Upsilon_i}{i!} - \pi X_i \right) K_m^i (\tau - \tau_d)^i$
7. $e^{j\Phi_{sSm}} \times e^{jH_{CS}}$	$H_{CS} = \pi q_2 (\tau - \tau_{ref})^2 + \pi \sum_{i=3}^{n} q_i (\tau - \tau_{ref})^i$
8. Rearange Terms $\rightarrow e^{j\Phi_{sSz}}$	$\Phi_{sSz} = \frac{-4\pi R_0 D(f_\eta) f_0}{c} + \sum_{i=0}^{n} C_i (\tau - \tau_s)^i$ $= \frac{-4\pi R_0 D(f_\eta) f_0}{c} + \pi(q_2 + K_f)(\tau - \tau_s)^2 + \pi \sum_{i=3}^{n} \left(q_i - X_i K_f^i + \frac{4f_0 \Upsilon_i R_{ref} K_f^i}{i!c} \right) (\tau - \tau_s)^i$ $+ \pi K_m \Delta\tau^2 (\alpha - 1)^2 + \sum_{i=3}^{n} \left(\frac{2\pi K_m^i f_0 \Delta\tau^i \Upsilon_i (\Delta\tau c + 2R_{ref})}{i!c} - \pi K_m^i \Delta\tau^i X_i \right) + \sum_{i=2}^{n} \pi \alpha^i \Delta\tau^i q_i$
9. Range FFT $\rightarrow e^{j\Phi_{SS2}}$	$\Phi_{SS2} = \frac{-4\pi R_0 D(f_\eta) f_0}{c} - \left(\frac{4\pi R_{ref}(1-\alpha)}{cD(f_\eta)} + \frac{4\pi\alpha R_0}{cD(f_\eta)} \right) f_\tau - \frac{\pi\alpha f_\tau^2}{K_f} - \pi \sum_{i=3}^{n} \left(q_i - X_i K_f^i + \frac{4f_0 \Upsilon_i R_{ref} K_f^i}{i!c} \right) f_\tau^i$ $+ \pi K_m \Delta\tau^2 (\alpha - 1)^2 + \sum_{i=3}^{n} \left(\frac{2\pi K_m^i f_0 \Delta\tau^i \Upsilon_i (\Delta\tau c + 2R_{ref})}{i!c} - \pi K_m^i \Delta\tau^i X_i \right) + \sum_{i=2}^{n} \pi \alpha^i \Delta\tau^i q_i$
10. $e^{j\Phi_{SS2}} \times e^{jH_R}$	$H_R = \frac{4\pi R_{ref} f_\tau (1-\alpha)}{cD(f_\eta)} + \frac{\pi\alpha f_\tau^2}{K_f} + \pi \sum_{i=3}^{n} \left(q_i - X_i K_f^i + \frac{4f_0 \Upsilon_i R_{ref} K_f^i}{i!c} \right) f_\tau^i$
11. Range IFFT $\rightarrow e^{j\Phi_{sSaz}}$	$\Phi_{sSaz} = \frac{-4\pi R_0 D(f_\eta) f_0}{c}$ $+ \pi K_m \Delta\tau^2 (\alpha - 1)^2 + \sum_{i=3}^{n} \left(\frac{2\pi K_m^i f_0 \Delta\tau^i \Upsilon_i (\Delta\tau c + 2R_{ref})}{i!c} - \pi K_m^i \Delta\tau^i X_i \right) + \sum_{i=2}^{n} \pi \alpha^i \Delta\tau^i q_i$
12. $e^{j\Phi_{sSaz}} \times e^{jH_{az}}$	$H_{az} = \frac{4\pi R_0 D(f_\eta) f_0}{c}$ $- \pi K_m \Delta\tau^2 (\alpha - 1)^2 - \sum_{i=3}^{n} \left(\frac{2\pi K_m^i f_0 \Delta\tau^i \Upsilon_i (\Delta\tau c + 2R_{ref})}{i!c} - \pi K_m^i \Delta\tau^i X_i \right) - \sum_{i=2}^{n} \pi \alpha^i \Delta\tau^i q_i$
13. Azimuth IFFT	

Table 3.4: Solved High-Order Filter Parameters and Chirp-Scaling Terms

Parameter	Solution
q_2	$K_f \frac{1-\alpha}{\alpha}$
q_3	$K_s K_f^2 \frac{1-\alpha}{3\alpha}$
X_3	$\frac{-(\alpha-2)K_s c + (\alpha-1)2f_0 \Upsilon_3 R_{ref} K_f}{3K_f c(\alpha-1)}$
q_4	$K_f^3 \frac{(\alpha-1)\left(f_0 D(f_\eta)c\Upsilon_3 + 6f_0 R_{ref} K_s K_f \Upsilon_3 - 9K_s K_f c X_3\right) + 2K_s^2 c}{-12c\alpha}$
X_4	$\frac{(\alpha-2)\left(f_0 D(f_\eta)c\Upsilon_3 + 6f_0 R_{ref} K_s K_f \Upsilon_3 - 9K_s K_f c X_3\right) - (\alpha-1)2f_0 \Upsilon_4 R_{ref} K_f + 2K_s^2 c}{-12K_f c(\alpha-1)}$
q_5	$K_f^4 \frac{(\alpha-1)\left(f_0 \Upsilon_4 D(f_\eta)c + 8f_0 \Upsilon_4 R_{ref} K_s K_f - 48X_4 K_s K_f c\right) + 6f_0 K_s \Upsilon_3 \left(4R_{ref} K_f K_s + cD(f_\eta)\right) - 36X_3 K_s^2 K_f c}{-60c\alpha}$
X_5	$\frac{(\alpha-2)\left(f_0 D(f_\eta)c\Upsilon_4 + 8f_0 R_{ref} K_s K_f \Upsilon_4 - 48K_s K_f c X_4\right) - (\alpha-1)2K_f f_0 \Upsilon_5 R_{ref} + 6f_0 K_s \Upsilon_3 \left(4R_{ref} K_f K_s + cD(f_\eta)\right) - 36K_s^2 K_f X_3}{-60K_f c(\alpha-1)}$
q_6	$K_f^5 \frac{8f_0 K_s \Upsilon_4 \left(5R_{ref} K_s K_f + cD(f_\eta)\right) - (\alpha-1)\left(-f_0 D(f_\eta)c\Upsilon_5 + 300K_s K_f c X_5 - 10f_0 R_{ref} K_s K_f \Upsilon_5\right) - 240K_s^2 K_f c X_4}{-360c\alpha}$
X_6	$\frac{(\alpha-2)\left(-300K_s K_f c X_5 + f_0 D(f_\eta)c\Upsilon_5 + 10f_0 R_{ref} K_s K_f \Upsilon_5\right) - (\alpha-1)2f_0 R_{ref} K_f \Upsilon_6 + 8f_0 \Upsilon_4 K_s \left(5R_{ref} K_s K_f + cD(f_\eta)\right) - 240X_4 K_s^2 K_f c}{-360K_f c(\alpha-1)}$

CHAPTER 4.   GENERALIZED LFM-CW SAR PROCESSING

Very small synthetic aperture radar (SAR) systems are made possible by using a linear frequency modulated continuous wave (LFM-CW) signal which can achieve a good signal-to-noise ratio with lower transmit power. Combined with an analog dechirp, these systems can be made with hardware that is simpler, cheaper, and consumes less power than traditional SAR systems. This enables the use of low cost SARs on small unmanned aircraft systems (UAS), which opens up a whole range of new applications, permitting SAR imagery to be collected in harsh climates or in environments too dangerous for manned aircraft or expensive SAR systems. The potential of this new technology has been shown in a variety of demonstration systems [41, 42, 43, 44, 45, 46, 47, 48, 49].

Along with new possibilities come new challenges. The fact that a CW signal is both continuously transmitting and receiving means that processing must take into account the continuous motion of the platform. Continuous wave operation requires a separate transmit and a receive antenna to separate the signals on the transmit and receive signal paths, also, the direct feed-through from the transmit to the receive antenna must be controlled. Several SAR processing algorithms have been adapted for LFM-CW SAR [6, 50, 51, 52, 53], but for some very useful algorithms (e.g., backprojection) the issues associated with using a CW signal have yet to be addressed. Also, like most traditional SAR processing, the existing algorithms make assumptions and approximations that lose validity when used with extreme SAR parameters.

This chapter contains a general treatment of the LFM-CW SAR signal and develops new SAR processing algorithms appropriate for processing CW data, taking care to examine approximations made along the way. We analyze the effects of the continuous platform motion, for linear and non-linear flight paths, and develop a general correction for the effects. An overview of LFM-CW SAR is provided in Section 4.1 with a discussion of the

LFM-CW SAR signal. In developing the processing methods, we first discuss high precision algorithms, then explore the approximations used in developing more computationally efficient algorithms. Section 4.2 examines backprojection for LFM-CW SAR and develops an algorithm kernel for handling the continuous motion, both precisely and approximately. In Section 4.3, we examine frequency domain processing methods, such as the range-Doppler algorithm (RDA) and the frequency scaling algorithm (FSA). We first show the signal derivation and the algorithms' dependence on a Taylor series expansion which approximates the signal in the dechirped Doppler domain (which is similar to the wavenumber domain in traditional SAR). For certain SAR system parameters, neglecting the higher order terms of the Taylor series expansion causes defocusing. To address this, an efficient generalized frequency scaling algorithm (GFSA) is developed that processes the data using an arbitrary number of terms of the expansion.

4.1 The LFM-CW SAR Signal

An LFM-CW radar continuously transmits a frequency modulated signal. This signal is a linear frequency ramp, or chirp. In SAR the radar is carried on a platform and the radar illuminates the target area. Part of the signal is scattered back to the radar where the receive antenna continuously collects the reflected signal which can then be digitized and processed to form the SAR image.

LFM-CW SAR often uses an analog dechirp to reduce sample rate required to digitize the signal. A general expression for the dechirped signal is

$$s_{dc}(t, \eta) = e^{j\left(2\pi k_r t(\tau - d) + 2\pi f_0(\tau - d) - \pi k_r\left(\tau^2 - d^2\right)\right)} \tag{4.1}$$

where τ is the two-way travel time to a target and d is the dechirp delay. The derivation of Eq. (4.1) is given in Subsection 4.1.1, including a discussion of how τ is approximated in processing algorithms.

For LFM-CW SAR systems with a direct dechirp [41, 42, 45, 49], $d = 0$, and Eq. (4.1) simplifies to

$$s_{dc0}(t, \eta) = e^{j\left(2\pi k_r t\tau + 2\pi f_0\tau - \pi k_r\tau^2\right)}. \tag{4.2}$$

The direct dechirp limits the available swath width. A large portion of the sampling bandwidth is used to record data that corresponds to the empty space between the SAR and the ground. A system with a delayed dechirp [54] can ignore data from ranges nearer than a minimum range determined by the duration of the delay. By doing this, the radar more efficiently utilizes the radar's resources, providing a wider ground swath. This is discussed in more detail in Subsection 4.1.1.

The two way time of flight to a target is approximated

$$\tau(t,\eta) = \frac{2R(t,\eta)}{c_0} \tag{4.3}$$

where R is the range to a target, which is dependent on slow-time η and fast-time t. This change in range needs to be precisely known to properly form a well-focused SAR image. The traditional SAR imaging scenario involves the platform moving in a straight line (or nearly a straight line with motion corrections [6]) where the change in range can be expressed as a hyperbolic function. Many processing algorithms are built around the assumption of a linear flight path. However, the increasing popularity of backprojection methods has made processing SAR data collected from non-linear flight paths gain more attention [55]. In any case, traditional SAR processing algorithms assume that the platform is stationary during a pulse, but with the continuous transmit and receive of LFM-CW SAR, the continuous motion of the platform causes noticeable degradation in image quality if not properly accounted for. In the following sections we develop processing algorithms that account for the continuous platform motion, starting with a general backprojection algorithm that handles arbitrary flight paths.

4.1.1 Derivation of the Dechirped Signal

The frequency of the LFM-CW signal increases from a starting frequency f_0, and spans the bandwidth BW, at the chirp-rate $k_r = BW \cdot PRF$. This cycle is repeated at the PRF, giving a PRI equal to the pulse length, T_p. The transmitted up-chirp signal can be
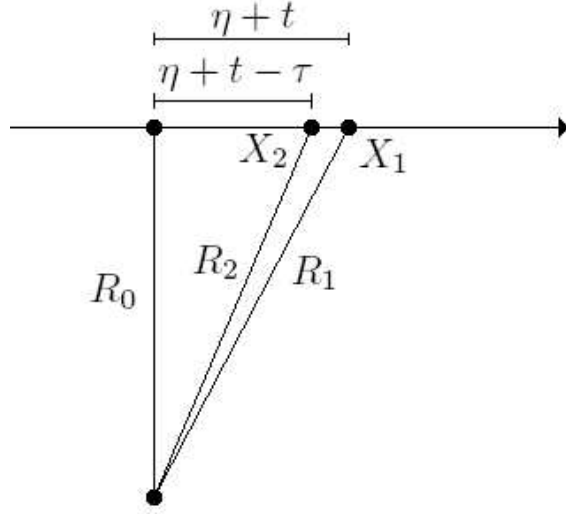
Figure 4.1: SAR imaging geometry, the platform flies in a line following the arrow. The radar echo received at point X_1 was transmitted toward the target at point X_2. The total time of flight for the signal can be calculated using Eq. (4.9).

expressed in the time domain, where t is fast-time and η is slow-time, as

$$s_t(t, \eta) = e^{j(\phi + 2\pi f_0 t + \pi k_r t^2)}, \tag{4.4}$$

where ϕ is the initial phase. A down chirp is similar with $f_{0d} = f_0 + BW$ being the starting frequency and $-k_r$ the chirp-rate.

At time t, the radar is also receiving the reflected signal transmitted at time $t - \tau$, where τ is the two way time of flight to a target. τ is calculated using the range to target, which is different from time t and time $t - \tau$ due to the constant motion of the aircraft. Using the slant range geometry shown in Fig. 4.1, we assign x_1 to the location of the radar at time $\eta + t$, and x_2 to the location at $\eta + t - \tau$, where η is slow-time. The calculation of τ is complicated by the motion of the aircraft, but can be approximated.

In order to precisely determine τ, we define a point, x_h approximately half way between x_1 and x_2.

$$x_h = x_2 + \frac{R_2}{c_0} v = x_1 - \frac{R_1}{c_0} v \tag{4.5}$$

where R_1 and R_2 are the distances to the target from points x_1 and x_2 respectively, defined as

$$R_1 = \sqrt{R_0^2 + x_1^2}, \tag{4.6}$$

$$R_2 = \sqrt{R_0^2 + x_2^2}. \tag{4.7}$$

We also know that $x_1 = (\eta + t)\,v$, from which we know R_1. That leaves us with unknowns x_2 and R_2, which we solve for,

$$x_2 = \frac{-v^3 R_1}{c_0\left(c_0^2 - v^2\right)} + \frac{v^2 x_1}{c_0^2 - v^2} + x_1 - \frac{R_1 v}{c_0} - \frac{v\sqrt{-v^2 R_0^2 c_0^2 + c_0^4 R_0^2 - 2c_0^3 x_1 R_1 v + c_0^2 R_1^2 v^2 + c_0^4 x_1^2}}{c_0(c_0^2 - v^2)} \tag{4.8}$$

and now we have all the pieces to calculate τ,

$$\tau = \frac{R_1 + R_2}{c_0}, \tag{4.9}$$

which can be used in Eq. (4.1) or Eq. (4.2).

A very close approximation is to assume that the ranges R_1 and R_2 are the same (for spaceborne SAR they can differ by as much as several meters, but for airborne applications they only differ by at most a few millimeters, and much less than that for low altitude operation), thus the expression for τ can be simplified to $\tau = 2R(t, \eta)/c_0$ where $R(t, \eta) = \sqrt{R_0^2 + v^2(t + \eta)^2}$ and R_0 is the range of closest approach to the target.

Going forward with this approximation, the received signal from a target at range R, with time delay τ is

$$s_r(t, \eta) = e^{j(\phi + 2\pi f_0(t - \tau) + \pi k_r(t - \tau)^2)}. \tag{4.10}$$

The transmit signal is mixed with the received signal and low-pass filtered in hardware, which is mathematically equivalent to multiplying Eq. (4.4) by the complex conjugate of Eq. (4.10). This results in the dechirped signal

$$s_{dc0}(t, \eta) = e^{j(2\pi f_0\tau + 2\pi k_r t\tau - \pi k_r \tau^2)}. \tag{4.11}$$

Alternatively the return signal is mixed with a copy of the transmit signal delayed by d

$$s_{td}(t, \eta) = e^{j(\phi + 2\pi f_0(t-d) + \pi k_r(t-d)^2)}. \tag{4.12}$$

The dechirped signal can then be expressed by multiplying Eq. (4.12) by the complex conjugate of Eq. (4.10), resulting in

$$s_{dc}(t, \eta) = e^{j\left(2\pi k_r t(\tau-d) + 2\pi f_0(\tau-d) - \pi k_r\left(\tau^2 - d^2\right)\right)}. \tag{4.13}$$

In the dechirped signal, each frequency directly correlates to a given range, $f_r = 2R\,k_r/c_0$. The sampling rate of an LFM-CW SAR can be much less than a traditional SAR. For a direct dechirp (no delay, $d = 0$), the sampling bandwidth directly corresponds to the maximum range that can be imaged,

$$f_s = \frac{2R_{max}k_r}{c_0}. \tag{4.14}$$

For a delayed dechirp, this maximum range is shifted by the delay,

$$f_s = \frac{2R_{max}k_r}{c_0} - d \cdot k_r = \frac{2R_{max}k_r}{c_0} - \frac{2R_{min}k_r}{c_0}. \tag{4.15}$$

A small LFM-CW SAR may be limited to a small sampling bandwidth due to hardware constraints driven by the need to reduce the size, weight, and power consumption. This can severely limit the imaging swath width. A delayed dechirp shifts more ranges into the sampling bandwidth, allowing for a wider swath. The delay is set to the nearest range desired in the image - the frequencies increase with range from that point. In this way none of the sampling bandwidth is wasted on any range nearer to the platform than this minimum range.

To remove returns from targets outside the desired swath, LFM-CW SAR systems usually employ a band-pass filter with high out of band rejection [45, 49, 54]. For targets at ranges farther than the maximum range with a corresponding frequency higher than the sampling rate, aliasing can occur, placing the target return within the swath. It is important that the bandpass filter attenuates such signals to avoid ambiguities. For a delayed dechirp there can be targets nearer to the radar than the minimum range. The frequencies from
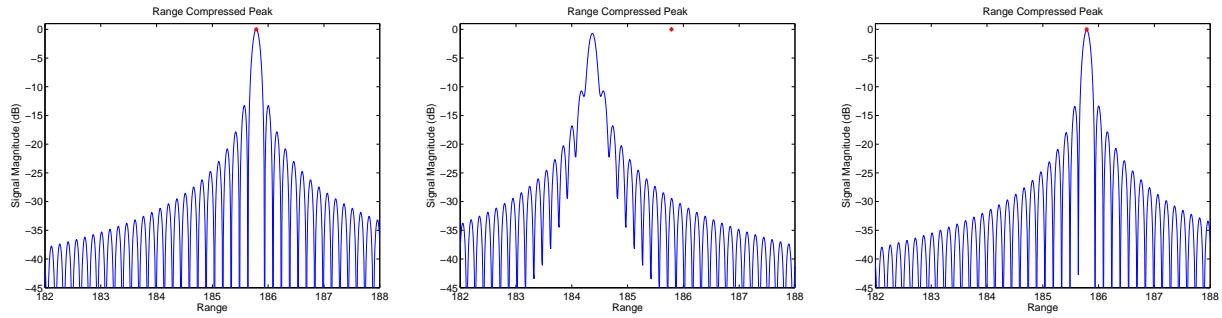
(a) Range-compressed point target, simulated without motion during the chirp

(b) Range-compressed point target where the continuous motion during the chirp is uncompensated

(c) A motion correction is applied to the data from (b).

Figure 4.2: SAR data of a single point target is simulated and range-compressed. These figures show cuts of this range-compressed data at the edge of the azimuth beam, i.e. on the far left edge of Fig. 4.3. The asterisk shows where the target peak should be, which is the range to the target at the time of the chirp shown in the figures. The effects of the continuous motion are clearly seen in (b), where the peak is shifted and is wider.
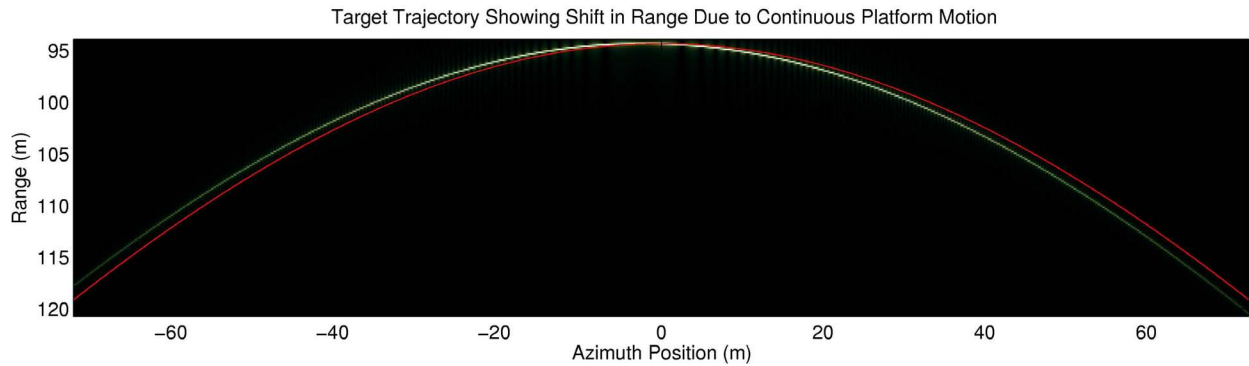
Figure 4.3: Range-compressed simulated SAR data for a single point target showing the range shift due to the continuous platform motion. The narrow solid line (the bottom line in the left side of the image and the top line on the right) represents the actual range to target for each azimuth position. The other line is the range compressed SAR data which is clearly shifted in range due to the platform motion.

such targets can fold over into the sampling band when the signal is dechirped to baseband. One solution is to dechirp the signal to an intermediate frequency, apply the band-pass filter, then mix to baseband [54] to avoid near range ambiguities.

61

4.1.2 Derivation of the Range-Compressed Signal

Assuming no motion during the chirp is equivalent to assuming R is not a function of t. With $\tau = 2R/c_0$, the range Fourier transform of Eq.(4.1) is calculated with the integral

$$
\begin{aligned}
S_R &= \int_{\frac{2R}{c_0}}^{\frac{2R}{c_0}+T_p} s_{dc}(t,\eta)\ e^{-j2\pi f_r t} dt & (4.16) \\[2mm]
&= \frac{\frac{1}{2}j\left(-e^{j\pi T_p(f_r+k_r d-k_r\tau)}+e^{-j\pi T_p(f_r+k_r d-k_r\tau)}\right)\ e^{j\pi\Phi_{rc}}}{\pi(f_r+k_r d-k_r\tau)} \\[2mm]
&= T_p\ \mathrm{sinc}[T_p\ (f_r+k_r d-k_r\tau)]\ e^{j\pi\Phi_{rc}}
\end{aligned}
$$

where

$$
\Phi_{rc} = k_r T_p(\tau-d) - f_r T_p + \frac{4k_r R\ (\tau-d)}{c_0} + 2f_0(\tau-d) - k_r(\tau^2-d^2) - \frac{4f_r R}{c_0}. \qquad (4.17)
$$

When there is no dechirp delay, i.e. $d=0$, this simplifies to

$$
S = T_p\ \mathrm{sinc}\left[T_p\ \left(f_r - \frac{2k_r R}{c_0}\right)\right] \cdot e^{\ j\pi\ \left(\frac{2k_r R T_p}{c_0} - f_r T_p + \frac{4k_r R^2}{c_0^2} + \frac{4f_0 R}{c_0} - \frac{4f_r R}{c_0}\right)}. \qquad (4.18)
$$

In order to explore what happens when we include the motion during the chirp, we assume that the platform motion is linear, calculate the two way time of flight to a target, and approximate the change in range as linear during a single chirp, thus

$$
\tau(t,\eta) = \frac{2\sqrt{R_0^2+v^2(\eta+t)^2}}{c_0} \approx \frac{2R}{c_0} + \frac{2v^2\eta t}{R\ c_0} \qquad (4.19)
$$

where $R = \sqrt{R_0^2+v^2\eta^2}$ and R_0 is the range of closest approach.

Substituting the approximation in Eq. (4.19) for τ in Eq. (4.1) and Eq. (4.2) and rearranging the terms yields

$$
\begin{aligned}
s_{dcm}(t,\eta) &= s_{dc}(t,\eta)\ e^{j\Phi_m}, & (4.20) \\[2mm]
s_{dcm0}(t,\eta) &= s_{dc0}(t,\eta)\ e^{j\Phi_m}, & (4.21)
\end{aligned}
$$
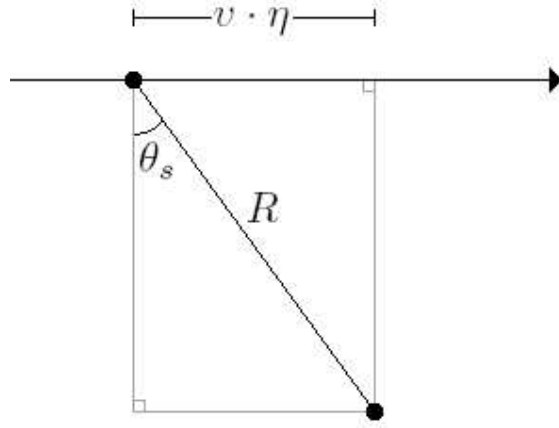
Figure 4.4: SAR imaging geometry, the SAR flies to the right following the arrow. A target at range R is at a squint angle of θ_s. The Doppler frequency of the signal return can be calculated from the angle or the distance to the point of closest approach (calculated as velocity times time, $v \cdot \eta$), according to Eq. (4.23).

where

$$\Phi_m = \left(-\frac{4v^4\eta^2\pi k_r}{R^2 c_0^2} + \frac{4v^2\eta\pi k_r}{R\ c_0}\right) t^2 + \left(\frac{-8v^2\eta\pi k_r}{c_0^2} + \frac{4v^2\eta\pi f_0}{R\ c_0}\right) t. \tag{4.22}$$

The effects of continuous motion on the signal phase can be seen by inspecting Eq. (4.22). As the range to target changes during a chirp, a change in frequency is introduced. The t^2 terms represent this chirp caused by the platform motion. The Fourier transform of this chirp is rect-like, and when convolved with Eq. (4.16) results in a spreading of the impulse response, as demonstrated in Fig. 4.2(b).

The motion also induces an effect on the carrier frequency, visible in the t terms. Additional insight can be gained by noticing that the final term is the Doppler frequency. Using the geometry of Fig. 4.4, the Doppler frequency is

$$2\pi f_d = 2\pi\ \frac{2v \sin (\theta_s)}{\lambda} = 2\pi\ 2v\frac{v}{R}\frac{\eta}{c_0}\frac{f_0}{c_0}. \tag{4.23}$$

The second t term in Eq. (4.22) is much larger than all the other terms and is the dominate effect of the platform motion: a frequency shift equal to the Doppler frequency, which translates into a range shift in the range-compressed data, as is visible in Figs. 4.2(b) and 4.3.

If we neglect the small terms and re-write Eq. (4.22) in terms of f_d, we obtain an convenient range-independent expression that can correct for the effects of continuous motion. The phase of the correction is

$$\Phi_{cor} = -2\pi f_d t. \tag{4.24}$$

Because the correction is expressed in terms of Doppler frequency, which is a measure of the continuous change in range to the target, the shift caused by the continuous motion of flight can be corrected. The correction can be applied to data collected with an arbitrary platform path, as demonstrated in Fig. 4.6.

4.2 LFM-CW Backprojection

Backprojection normally operates on interpolated, range-compressed data. For dechirped SAR, interpolation and range compression can be performed by means of zero-padding and a range Fourier transform; however, the continuous platform motion complicates the issue. The derivation of an expression for the range-compressed data is found in Subsection 4.1.2. For a pixel located at (x_0, y_0, z_0), the SAR backprojection algorithm can be expressed as

$$A(x_0, y_0, z_0) = \sum_n S_R(r[n]) \ e^{j\Phi_e(r[n])} \tag{4.25}$$

where $A(x_0, y_0, z_0)$ is the complex pixel power, $r[n]$ is the distance from the pixel location to the platform antenna phase center position for chirp number n, $\Phi_e(r[n])$ is the complex conjugate of the expected phase for range $r[n]$, and $S_R(r[n])$ is the range-compressed SAR data, defined in Eq. (4.16), interpolated to slant range $r[n]$. We take Eq. (4.17) allowing $f_r = 2Rk_r/c_0 - k_r d$, simplifying and conjugating to obtain

$$\Phi_e(r[n]) = \frac{4\pi k_r r[n]^2}{c_0^2} - \frac{4\pi f_0 r[n]}{c_0} - \pi k_r d^2 + 2\pi f_0 d. \tag{4.26}$$

The advantages of backprojection include the simplicity of the algorithm, the parallel computation structure, the ability to process data from an arbitrary platform path, and the
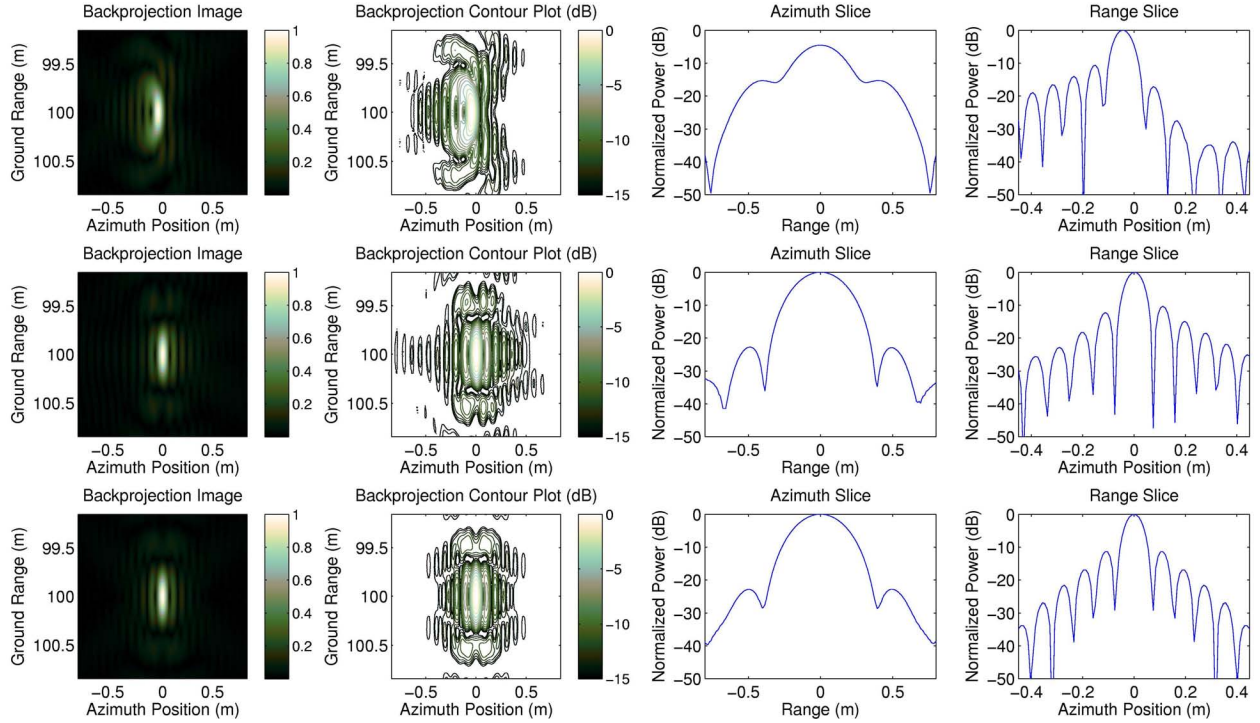
Figure 4.5: Simulated SAR data for a point target with a linear trajectory, a bandwidth from 1.5 to 2 GHz, and a 65° beamwidth with no squint, processed with the backprojection algorithm of Section 4.2. The leftmost column shows the magnitude of the focused SAR image, the second column shows a contour plot of the focused image, the two columns on the right show an azimuth slice and a range slice, respectively, through the center of the target. The first row shows defocusing and a shift in the target location due to the uncompensated continuous platform motion. In the second row the continuous motion is efficiently compensated using the correction of Eq. (4.24), and in the third row the continuous motion is inefficiently accounted for using the exact backprojection of Eq. (4.27).

ability to project the data onto a three dimensional grid. The dissadvantages are that the motion of the platform must be precisely known and the algorithm is very computationally taxing, though exploiting the parallel nature of the algorithm and the parallel processing capabilities of modern general-purpose graphic processor units can greatly improve the processing time. (BYU has reported a 300 times speed up in backprojection processing using an NVIDIA C1060 Tesla card [56].)

In using backprojection to process LFM-CW SAR data, it is important to account for the spreading and shifting effects visible in the range-compressed data due to the continuous platform motion, as discussed in Subsection 4.1.2. There are several of ways to do this. The
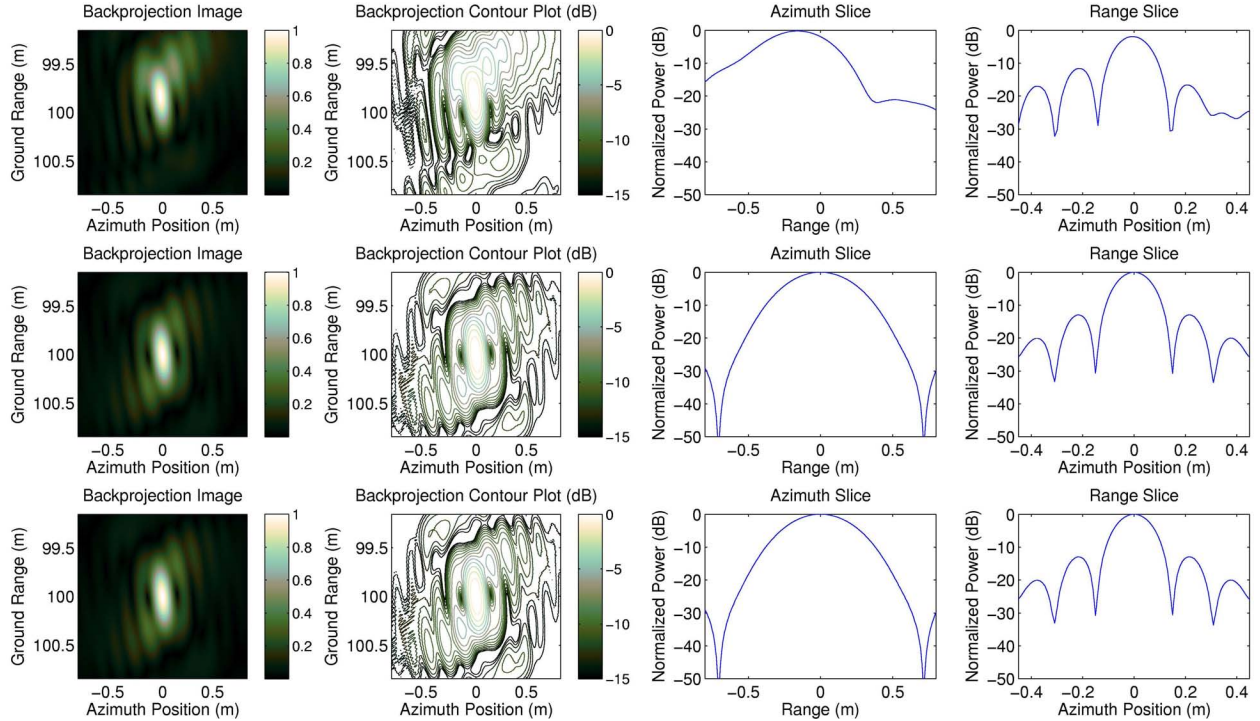
Figure 4.6: Simulated SAR data from a quarter of a circular path, where the target is located near the far edge of the circle, with the same SAR parameters and image layout as in Fig. 4.5. The first row neglects continuous motion, the middle row corrects for the motion using Eq. (4.24), and the bottom row is from exact processing in Eq. (4.27). The description of the columns is the same as in Fig. 4.5.

first is to use the raw data directly, without range-compression. The platform position for each *sample* of raw data is used. In this case the backprojection operation expands to

$$A_2(x_0, y_0, z_0) = \sum_t \sum_\eta s_{dc}(t, \eta) \, e^{(j\Phi_{e2}(t,\eta))} \tag{4.27}$$

where Φ_{e2} is the conjugate of the phase in Eq. (4.1) or Eq. (4.2), and the $\tau(t, \eta)$ buried inside s_{dc} and Φ_{e2} is the continuously changing two way time of flight to the point (x_0, y_0, z_0). This is a very exact method, but is even more computationally taxing than the conventional backprojection algorithm.

The second (and more efficient) option for accounting for the continuous motion is to use the correction presented in Eq. 4.24. In Fig. 4.5 simulated SAR data with a standard linear trajectory is processed with and without accounting for the continuous platform motion

showing the effects on the image quality. In Fig. 4.6 the platform trajectory is circular, showing how the same continuous motion correction also works for non-linear flight paths. Real SAR imagery processed with the LFM-CW backprojection algorithm can be found in Appendix C, in Fig. C.11.

4.3 Generalized Frequency Domain Processing

For SAR processing that is more efficient than backprojection, frequency domain methods have been developed, such as the RDA and the FSA. These algorithms apply a series of matched filters and scaling terms or interpolations to compress the data in range and azimuth and remove the range cell migration. Both of these algorithms depend upon a Taylor series approximation of the signal in the dechirped Doppler domain. This approximation is only valid for a limited set of SAR parameters, which prevents these algorithms from properly focusing the SAR data when the radar parameters push beyond the validity of the approximation.

This section derives an expression for the SAR signal in the dechirped Doppler domain. The Taylor series expansion of the signal and the errors it introduces are then discussed. The relationship between the Taylor approximation and the frequency domain processing algorithms is shown. To overcome the limits of these algorithms, a generalized frequency scaling algorithm (GFSA) that includes an arbitrary number of terms of the expansion is developed.

4.3.1 Derivation of LFM-CW SAR Signal in the Dechirped Doppler Domain

In processing, an azimuth Fourier transform of the raw, dechirped data puts the data in the dechirped Doppler domain. Analytically computing the azimuth Fourier transform for Eq. (4.1) is impractical, so finding an expression for the signal requires some algebraic manipulation and an approximation. We start with the range-compressed data, make an approximation of the original dechirped signal, then take the azimuth Fourier transform.

From Eq. (4.16) and Eq. (4.20) in Subsection 4.1.2, the range-compressed signal can be expressed as a function of range-frequency. Range-frequency has a direct relationship to

the distance to the target (the target range) according to $f_r = 2R\,k_r/c_0$. Thus,

$$S_R(f_r, \eta) = \mathcal{F}_t\left\{e^{j\Phi_m}\right\} * T_p \operatorname{sinc}\left[T_p\left(f_r - \frac{2k_r R}{c_0}\right)\right] \cdot e^{j\left(\frac{4\pi f_0 R}{c_0} - \pi T_p f_r + \frac{2\pi T_p k_r R}{c_0} - \frac{4\pi f_r R}{c_0} + \frac{4\pi k_r R^2}{c_0^2}\right)}$$

(4.28)

where $e^{j\Phi_m}$ represents the effects of the continuous platform motion expressed in Eq. (4.22). For convenience, we rewrite the last five exponential terms of Eq. (4.28) as

$$e^{j(A_s + B_s + C_s + D_s + E_s)}.$$

(4.29)

As in [1, 57], the inverse Fourier transform is facilitated by making a substitution and multiplying Eq. (4.28) by 1, or an equivalent expression:

$$e^{\left(-j\frac{\pi}{k_r}f_r^2\right)} e^{\left(j\frac{\pi}{k_r}f_r^2\right)} = e^{j\left(-\frac{\pi}{k_r}f_r^2 + \frac{\pi}{k_r}f_r^2\right)} = e^{j\left(-\frac{\pi}{k_r}f_r^2 + G_s\right)}.$$

(4.30)

The substitution is

$$F = f_r - \frac{2k_r R}{c_0}$$

(4.31)

and we note that

$$-\pi T_p F = -\pi T_p f_r + \frac{2\pi T_p k_r R}{c_0} = B_s + C_s$$

(4.32)

$$\frac{\pi}{k_r} F^2 = \frac{\pi}{k_r} f_r^2 - \frac{4\pi f_r R}{c_0} + \frac{4\pi k_r R^2}{c_0^2} = G_s + D_s + E_s.$$

(4.33)

We can now re-write Eq. (4.28) as

$$S_R = \mathcal{F}_t\left\{e^{j\Phi_m}\right\} * T_p \operatorname{sinc}[T_p\ F] \cdot e^{j\frac{4\pi f_0 R}{c_0}}\ e^{-j\pi T_p F}\ e^{j\frac{\pi}{k_r}F^2}\ e^{-j\frac{\pi}{k_r}f_r^2}.$$

(4.34)

The inverse Fourier integral is also expressed applying the F substitution

$$\int_{-\infty}^{\infty} e^{j2\pi f_r t} df_r = \int_{-\infty}^{\infty} e^{j2\pi\left(F + \frac{2k_r R}{c_0}\right)t} dF = e^{j\frac{4\pi k_r R t}{c_0}} \int_{-\infty}^{\infty} e^{j2\pi F t} dF$$

(4.35)

68

and the inverse Fourier integral for Eq. (4.34) is computed

$$
\begin{aligned}
s_{dc0} &= e^{j\pi k_r t^2} * \left\{ e^{j\Phi_m} \ T_p \ e^{j\frac{4\pi f_0 R}{c_0}} \ e^{j\frac{4\pi k_r R t}{c_0}} \cdot \int_{-\infty}^{\infty} \text{sinc}[T_p \ F] \ e^{-j\pi T_p F} \ e^{j\frac{\pi}{k_r} F^2} \ e^{j2\pi F t} dF \right\} \\
&\approx e^{j\pi k_r t^2} * \left\{ \text{rect}\left(\frac{t - Tp}{T_p}\right) \ e^{j\Phi_m + j\frac{4\pi f_0 R}{c_0} + j\frac{4\pi k_r R t}{c_0}} \right\}
\end{aligned}
\tag{4.36}
$$

where the F^2 term is neglected in computing the integral (which is a good approximation for a large time-bandwidth product [1, 57]) and the sinc function transforms to a rect function shifted by the F terms. The term on the left hand side of the convolution in the last line of Eq. (4.36) is known as the residual video phase (RVP) term [1, 57].

The azimuth Fourier transform for the signal can be computed using the principle of stationary phase. We express the phase of the signal within the curly brackets on the bottom line of Eq. (4.36) using the same approximation as for the continuous motion correction of Eq. (4.24). This phase is

$$
\phi_s = 2\pi f_d t + \frac{4\pi f_0 R}{c_0} + \frac{4\pi k_r R t}{c_0}.
\tag{4.37}
$$

We use the linear motion assumption, substituting $R = \sqrt{R_0^2 + v^2 \eta^2}$ into Eq. (4.37), and setting the derivative of $\phi_s - 2\pi f_a \eta$ with respect to η equal to zero, resulting in

$$
\frac{4\pi f_0 v^2 \eta}{c_0 \sqrt{R_0^2 + v^2 eta^2}} + \frac{4\pi k_r t v^2 \eta}{c_0 \sqrt{R_0^2 + v^2 eta^2}} - 2\pi f_a = 0.
\tag{4.38}
$$

The stationary point is found by solving for η

$$
\eta = \frac{c_0 f_a R_0}{v \sqrt{-f_a^2 c_0^2 + 4v^2 f_0^2 + 8v^2 f_0 k_r t + 4v^2 k_r^2 t^2}}.
\tag{4.39}
$$
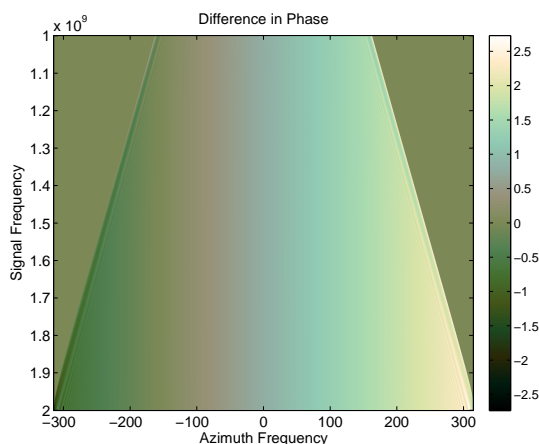
(a) The approximation from Eq. (4.41) shows little variation in the phase difference over the support band. This indicates that the approximation is very close to the actual signal phase. When used to form an image, the whole support band contributes in generating a well focused image, as seen in Fig. 4.9(a).
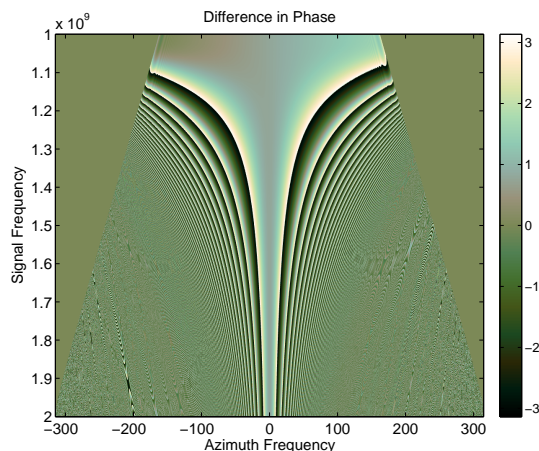
(b) A second order approximation from Eq. (4.45) has a very small portion of the support band (the upper and middle sections) with a nearly constant phase difference. When used to form an image, only a small portion of the support band contributes to properly focusing the target, which results in poor focusing, as in Fig. 4.9(b)
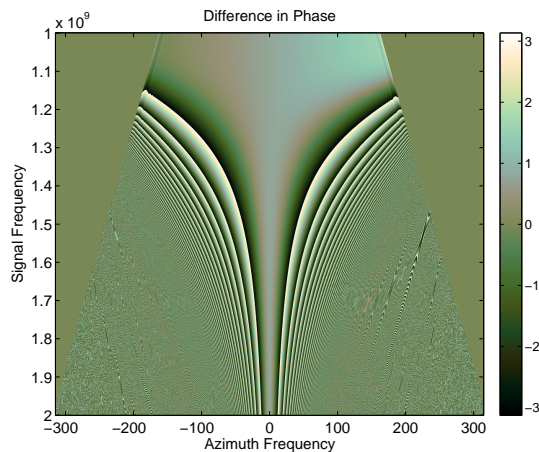
(c) A third order approximation has a larger portion of the support band that is useful for image formation.
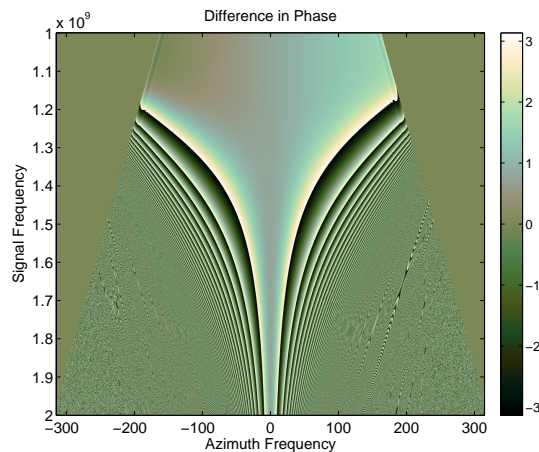
(d) The fourth order approximation increases the useful portion of the support band due to the higher order terms.

Figure 4.7: These figures show the phase difference between the azimuth Fourier transform of simulated SAR data, and analytical approximations for the signal from Eqs. (4.41) and (4.45). The simulated data shown has a bandwidth of 1 to 2 GHz, a beamwidth of 57° and a velocity of 50 m/s. The support band has a trapezoidal shape because the Doppler bandwidth is smaller for a fixed beamwidth at lower frequencies. Ideally the phase difference is constant over the support band, but each approximation falls short of this ideal.
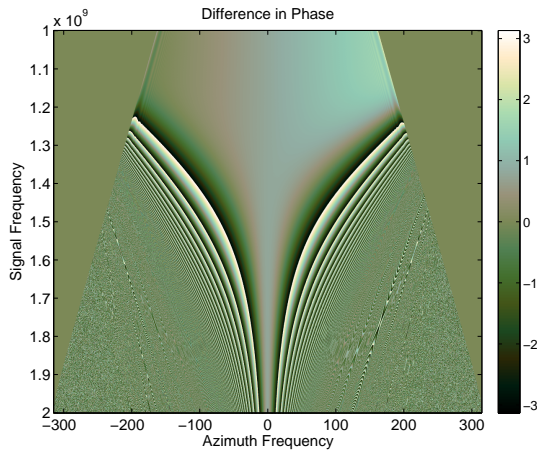
(a) The fifth order approximation shows how the useful portion of the support band increases with the inclusion of higher order terms.
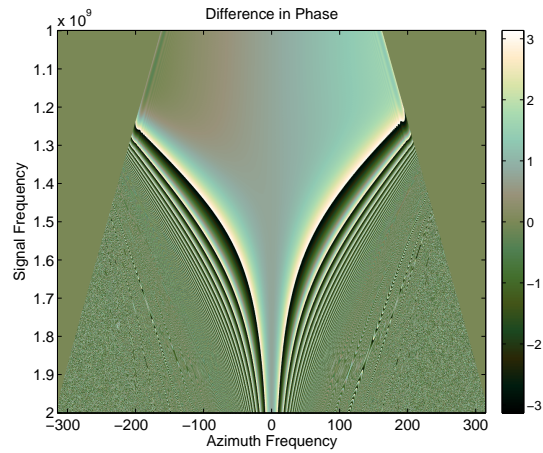
(b) A sixth order approximation results in better focusing, as seen in Fig. 4.9(c).
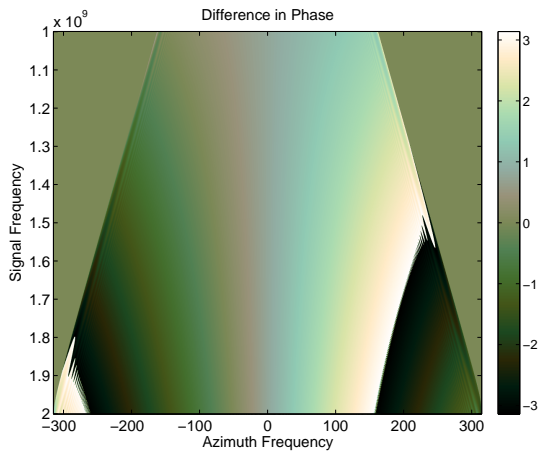
(c) Neglecting the continuous platform motion term in the approximation from Eq. (4.41) increases the phase error.
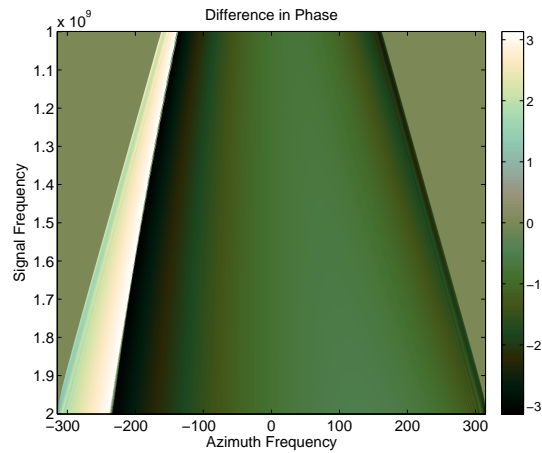
(d) Neglecting the residual video phase (RVP) correction with the approximation from Eq. (4.41) also increases the phase error

Figure 4.8: These figures show the phase difference as in Figs. 4.7(a)-4.7(d)
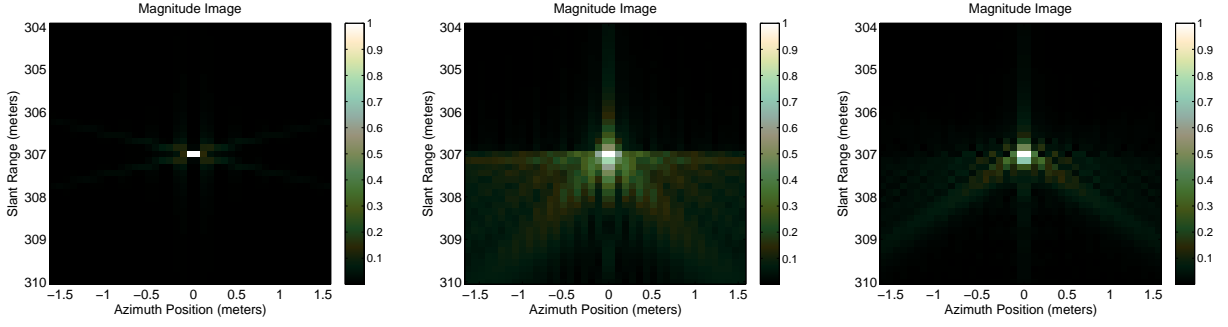
(a) Well-focused point target formed using Eq. (4.41), see Fig. 4.7(a)

(b) Poorly focused point target formed using a second order approximation in Eq. (4.45), see Fig. 4.7(b)

(c) Focused point target formed using a sixth order approximation in Eq. (4.45), see Fig. 4.8(b)

Figure 4.9: For a single point target, the conjugate of Eq. (4.41) or Eq. (4.45) can be used directly to generate a focused image. Using this method, the effects of different order approximations of Eq. (4.45) can be seen in the focused targets shown here.

Then, the phase of the signal after the azimuth Fourier transform is found by substituting Eq. (4.39) back into $\phi_s - 2\pi f_a \eta$. With some algebraic manipulation the expression simplifies,

$$
\begin{aligned}
\Phi_{S_A} &= \left(\frac{-\pi k_r f_d^2}{f_0^2} + \frac{2\pi k_r f_d}{f_0} \right) t^2 + 2\pi f_d t + \frac{4\pi (f_0 + k_r t) \sqrt{R_0^2 + \frac{c_0^2 f_a^2 R_0^2}{-f_a^2 c_0^2 + 4v^2 f_0^2 + 8v^2 f_0 k_r t + 4v^2 k_r^2 t^2}}}{c_0} \\
&\quad - \frac{2\pi f_a^2 c_0 R_0}{v\sqrt{-f_a^2 c_0^2 + 4v^2 f_0^2 + 8_v^2 f_0 K r t + 4v^2 k_r^2 t^2}} \\
&= \left(\frac{-\pi k_r f_d^2}{f_0^2} + \frac{2\pi k_r f_d}{f_0} \right) t^2 + 2\pi f_d t + \frac{\frac{8\pi (f_0 + k_r t)^2 v R_0}{c_0} - \frac{2\pi f_a c_0 R_0}{v}}{\sqrt{-f_a^2 c_0^2 + 4v^2 f_0^2 + 8v^2 f_0 k_r t + 4v^2 k_r^2 t^2}} \\
&= \left(\frac{-\pi k_r f_d^2}{f_0^2} + \frac{2\pi k_r f_d}{f_0} \right) t^2 + 2\pi f_d t + \frac{4\pi R_0}{\lambda} \sqrt{\left(1 + \frac{k_r \lambda t}{c_0} \right)^2 - \frac{f_a^2 \lambda^2}{4v^2}}. \quad (4.40)
\end{aligned}
$$

Assuming that $f_d = f_a$, the exponentials that make up the signal in the dechirped-Doppler domain can be expressed,

$$
S_A = e^{j\pi k_r t^2} * \left\{ e^{j\left[\frac{-\pi k_r f_a^2}{f_0^2} + \frac{2\pi k_r f_a}{f_0} \right] t^2 + 2\pi f_a t} \; e^{j\left[\frac{4\pi R_0}{\lambda} \sqrt{\left(1 + \frac{k_r \lambda t}{c_0} \right)^2 - \frac{f_a^2 \lambda^2}{4v^2}} \right]} \right\}, \quad (4.41)
$$

72

which is a very good approximation of the signal. Fig. 4.7(a) reveals a small variation in the phase difference between the actual phase and this approximation over the support band, indicating a small error due to the approximation $F^2 = 0$. The effects of the continuous platform motion can be removed at this point by multiplying Eq. (4.41) by Eq. (4.24).

4.3.2 Taylor Series Expansion of the SAR Signal

Typical processing algorithms use a Taylor series approximation of the square-root term in Eq. (4.41) about the point $t = 0$. To simplify the analysis, we define

$$D(f_\eta) = \sqrt{1 - \frac{f_a^2 \lambda^2}{4v^2}}, \tag{4.42}$$

then substitute it into the square-root term in Eq. (4.41) and expand,

$$
\begin{aligned}
\Upsilon(t) &= \sqrt{\left(1 + \frac{k_r \lambda t}{c_0}\right)^2 - 1 + D^2(f_\eta)} \\
&\approx \Upsilon(0) + \frac{\Upsilon'(0)}{1!}t + \frac{\Upsilon''(0)}{2!}t^2 + \frac{\Upsilon'''(0)}{3!}t^3 \cdots \\
&\approx Y_0 + Y_1 t + \frac{Y_2}{2!}t^2 + \frac{Y_3}{3!}t^3 \cdots
\end{aligned}
\tag{4.43}
$$

where Y_i is the ith derivative of $\Upsilon(t)$ evaluated at $t = 0$.

The phase error of this approximation can be expressed

$$\phi_{Error} = \frac{4\pi R_0}{\lambda} \left[\Upsilon(t) - \sqrt{\frac{k_r \lambda t \left(2c_0 + k_r \lambda t\right)}{c_0^2} + D^2(f_\eta)} \right] \tag{4.44}$$

which is a function of the following four parameters:

1. the range to target, R_0;

2. the center frequency, f_0;

3. the chirp-rate times fast-time, $k_r\, t$;

4. the azimuth frequency, f_η.

73
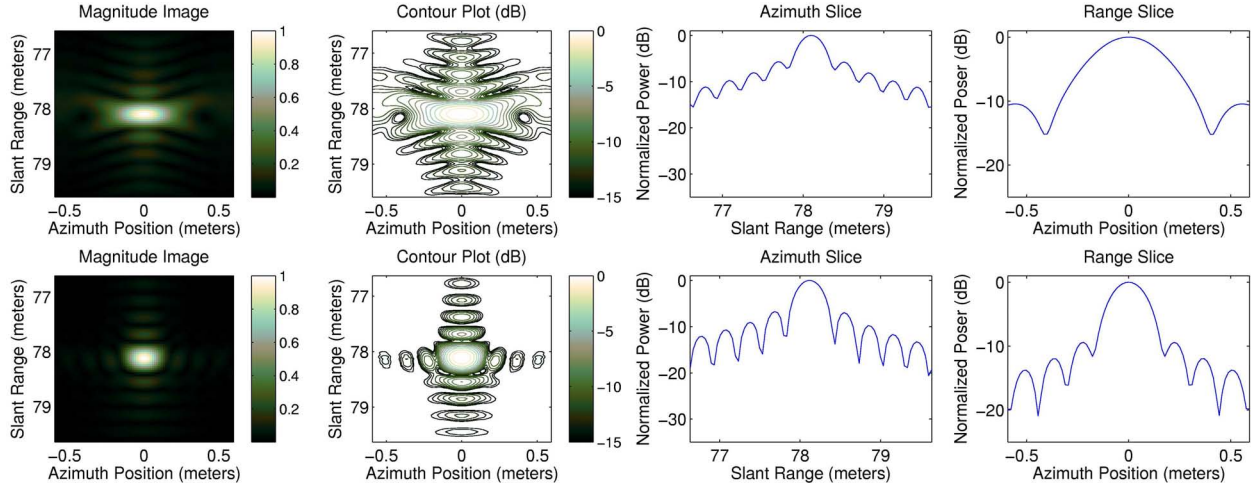
Figure 4.10: Simulated SAR data for a point target with a bandwidth from 2.5 to 3 GHz and a 20° beamwidth with no squint. The top row shows the results of processing the data with the FSA, with the target at the reference range for the SRC. The bottom row shows the results of processing the data with the proposed generalized FSA with $n = 2$. The description of the columns is the same as in Fig. 4.5.
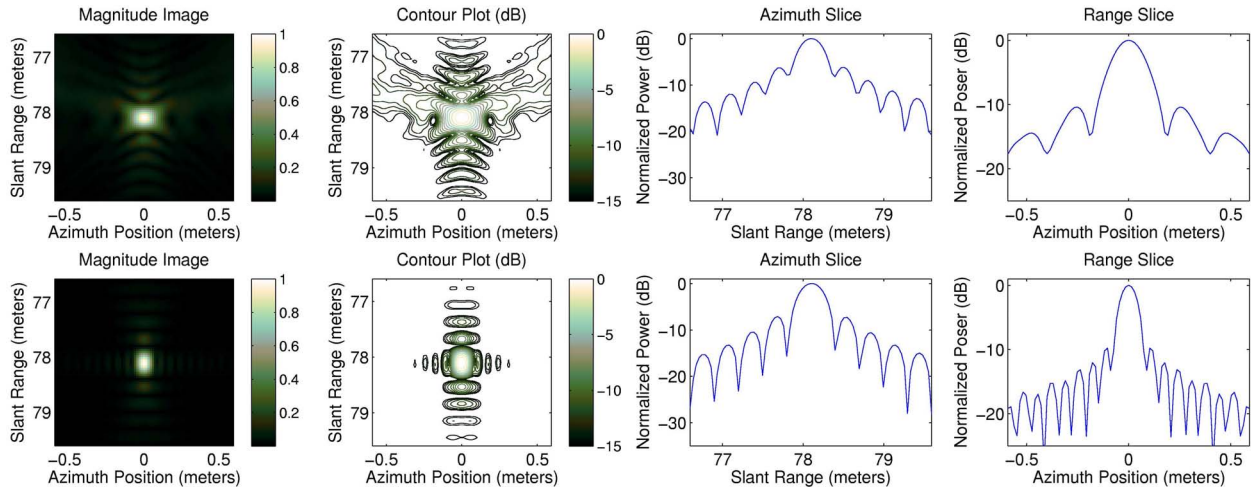
Figure 4.11: Simulated SAR data for a point target with a bandwidth from 5.5 to 6 GHz and a 20° beamwidth with no squint. The top row shows the results of processing the data with the FSA, with the target at the reference range for the SRC. The bottom row shows the results of processing the data with the proposed generalized FSA with $n = 2$. The description of the columns is the same as in Fig. 4.5.

The phase error gets larger as the range increases, the center frequency decreases, the product of the chirp-rate times t increases, and/or the azimuth frequency increases. The product of

the chirp-rate times fast-time grows with increases in bandwidth while the azimuth frequency increases with wider antenna beamwidths.

In Fig. 4.7(b) we see how only a small portion of the frequency support band is usable due to the large phase errors of the second order approximation. As suggested by Figs. 4.7(c), 4.7(d), 4.8(a), and 4.8(b), including more high order terms in the approximation reduces the phase error, making more of the support band usable. The effect of these phase errors on target focusing can be seen in Figs. 4.9(a), 4.9(b), and 4.9(c) where a single point target is focused using the conjugate of Eq. (4.41) or Eq. (4.45). It can be seen that, as expected, the target focusing is best when no approximations are used. The use of approximations in efficient SAR algorithms introduces errors that can significantly reduce image quality. However, when higher order approximations that are closer to the ideal are used, the resulting image is better focused.

The phase of the signal with n order terms is expressed as

$$\Phi_{S_a} = \frac{4\pi R_0 D(f_\eta)}{\lambda} + \frac{4\pi R_0 ket}{D(f_\eta)c_0} + \frac{\pi t^2}{K_m} + \sum_{i=3}^{n} \frac{4\pi R_0}{\lambda} Y_i \tag{4.45}$$

where

$$K_m = \frac{D^3(f_\eta)c_0^2}{2R_0 \lambda k_r^2 \left(D^2(f_\eta) - 1\right)}. \tag{4.46}$$

4.3.3 Frequency Domain SAR Processing Algorithms

The RDA uses a second order expansion. In the algorithm, the zeroth order term (the first term of Eq. (4.45)) is the azimuth (Doppler) modulation matched during azimuth compression, range cell migration shows up in the first order term (the second term of Eq. (4.45)) and is corrected by way of an interpolation, while the second order term (the third term of Eq. (4.45)) is compensated in the secondary range compression (SRC).

The FSA, as described in [50, 52, 57], uses a third order expansion, but only compensates for the second and third order terms (which correspond to the SRC) at a reference range. Recognizing the increased importance of the higher order terms for squinted data, the non-linear FSA from [40], introduces a number of steps that can reduce the range depen-

dence of the second and third order terms, providing better performance for SAR scenarios (such as squint mode) that push beyond the validity of the traditional approximations.

A generalized FSA that accounts for an arbitrary number of terms is beneficial for processing SAR data with a wide variety of system parameters. For a given set of SAR parameters, an appropriate number of terms can be used to maximize efficiency, accuracy, and precision in processing. Such an algorithm is now derived. The algorithm flow is shown in Table 4.1.

The first step is to apply a prefilter, with phase

$$H_{pre} = \sum_{i=3}^{n} \pi X_i t^i \tag{4.47}$$

where X_i is solved for at a later point in this derivation and is carefully chosen to reduce the range dependence of the higher order terms and to compensate for the higher order terms at a reference range, R_f.

A range Fourier transform of the signal is now computed using the principle of stationary phase. To find the stationary point, the terms of order higher than two are neglected and the derivative of $\Phi_{S_a} + H_{pre} - 2\pi f_r t$ is set to zero and solved for t,

$$t = \frac{-(2R_0 k_r - f_r D(f_\eta) c_0) K_m}{D(f_\eta) c_0} = -(f_t - f_r) K_m \tag{4.48}$$

where f_t is the frequency trajectory of a target at range R_0,

$$f_t = \frac{2R_0 k_r}{c_0 D(f_\eta)}. \tag{4.49}$$

The phase of the signal after the range Fourier transform is

$$\begin{aligned} \Phi_{S_3} &= \frac{4\pi R_0 D(f_\eta)}{\lambda} - \frac{4\pi R_0 k_r (f_t - f_r) K_m}{D(f_\eta) c_0} + \pi (f_t - f_r)^2 K_m \\ &+ \sum_{i=3}^{n} (-1)^i \left(\frac{4\pi R_0 Y_i}{\lambda\, i!} + \pi X_i \right) (f_t - f_r)^i K_m^i + 2\pi f_r (f_t - f_r) K_m. \end{aligned} \tag{4.50}$$

76

Figure 4.12: Simulated SAR data for point targets with a bandwidth from 2.5 to 3 GHz and a 20° beamwidth with a 15° squint. The data is processed with the FSA, with the center row showing a target at the reference range that was used for SRC. The top row shows a nearer-range target while the bottom row shows a farther-range target. The description of the columns is the same as in Fig. 4.5.

Combining the second term and the last term, and again using the substitution of Eq. (4.49),

$$
\begin{aligned}
&-\frac{4\pi R_0 k_r (f_t - f_r) K_m}{D(f_\eta) c_0} + 2\pi f_r (f_t - f_r) K_m \\
&= \frac{2\pi (f_t - f_r) K_m (-2R_0 k_r + f_r D(f_\eta) c_0)}{D(f_\eta) c_0} \\
&= -2\pi (f_t - f_r)^2 K_m,
\end{aligned}
\tag{4.51}
$$

which is combined with the third term of Eq. (4.50), and simplifies to

$$
\Phi_{S_3} = \frac{4\pi R_0 D(f_\eta)}{\lambda} - \pi (f_t - f_r)^2 K_m + \sum_{i=3}^{n} (-1)^i \left(\frac{4\pi R_0 Y_i}{\lambda \, i!} + \pi X_i \right) (f_t - f_r)^i K_m^i.
\tag{4.52}
$$

Figure 4.13: Simulated SAR data for point targets with a bandwidth from 2.5 to 3 GHz and a 20° beamwidth with a 15° squint. The data is processed with the proposed generalized FSA with $n = 2$, with the center row showing a target at the reference range. The top row shows a nearer-range target while the bottom row shows a farther-range target. The focusing is clearly superior to the traditional FSA in Fig. 4.12. The description of the columns is the same as in Fig. 4.5.

A scaling filter consisting of terms of orders from two to n is now applied to the signal:

$$H_{scale} = \sum_{i=2}^{n} \pi q_i \left(f_{ref} - f_r \right)^i. \tag{4.53}$$

The signal is expanded and algebraically rearranged with the help of the following substitutions:

$$f_t = f_{ref} + \Delta f, \tag{4.54}$$

and

$$f_{ref} = f_s - D(f_\eta) \, \Delta f. \tag{4.55}$$

where

$$\Delta f = \frac{2 \left(R_0 - R_f \right) k_r}{c_0 D(f_\eta)} \tag{4.56}$$

78

Figure 4.14: Simulated SAR data for point targets with a bandwidth from 5.5 to 6 GHz and a 20° beamwidth with a 15° squint. The data is processed with the FSA, with the center row showing a target at the reference range that was used for the SRC. The top row shows a nearer-range target while the bottom row shows a farther-range target. The description of the columns is the same as in Fig. 4.5.

and f_s is the scaled target frequency trajectory for a target at range R_0 that has the same shape as the reference frequency trajectory.

The signal is rearranged to match the form

$$\Phi_{S_{3b}} = \sum_{i=0}^{n} C_i \ (f_s - f_r)^i \tag{4.57}$$

where

$$
\begin{aligned}
C_i \ \ = \ \ & c_{hi} + \sum_{k=i}^{n} \frac{k!}{i! \, (k-i)!} \\
& \cdot \left\{ (-K_m)^k \left(\Delta f \ (1 - D(f_\eta)) \right)^{(k-i)} \cdot \left(\frac{4\pi R_0 Y_k}{k! \lambda} + \pi X_k \right) + \pi q_k \left(-\Delta f D(f_\eta) \right)^{(k-i)} \right\},
\end{aligned}
\tag{4.58}
$$

79
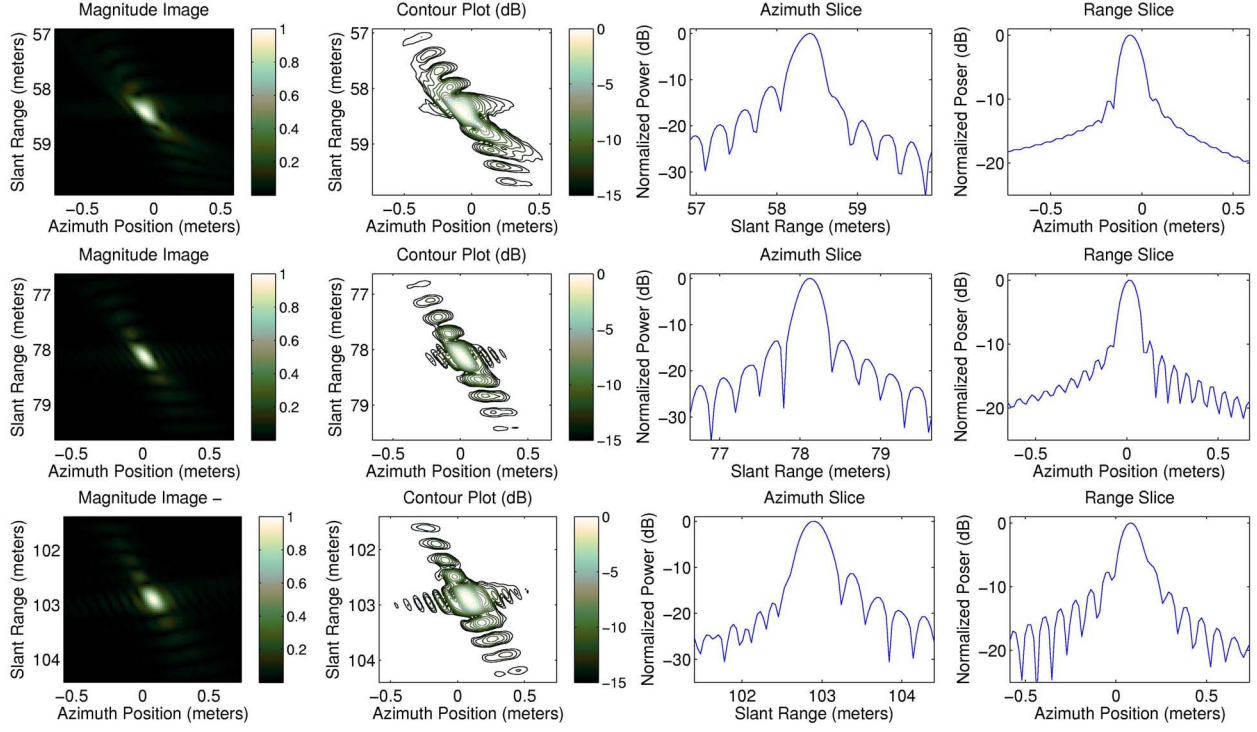
Figure 4.15: Simulated SAR data for point targets with a bandwidth from 5.5 to 6 GHz and a 20° beamwidth with a 15° squint. The data is processed with the proposed generalized FSA with $n = 2$, with the center row showing a target at the reference range. The top row shows a nearer-range target while the bottom row shows a farther-range target. The focusing is clearly superior to the traditional FSA in Fig. 4.14. The description of the columns is the same as in Fig. 4.5.

and

$$
\begin{aligned}
c_{h0} &= -\pi K_m \Delta f^2 \left(D(f_\eta) - 1 \right)^2, \\
c_{h1} &= 2\pi K_m \Delta f \left(D(f_\eta) - 1 \right), \\
c_{h2} &= -\pi K_m, \\
c_{hi} &= 0 \quad \text{for } i > 2,
\end{aligned}
\tag{4.59}
$$

where $X_i = 0$ and $Y_i = 0$ for $i < 3$, and $q_i = 0$ for $i < 2$.

The range dependence of each C_i term can be reduced by appropriately choosing the X_i's and the q_i's. Determining these values is aided by expanding each C_i about a reference range R_f. In Eq. (4.58), each R_0 is expanded and expressed in terms of Δf from Eq. (4.56):
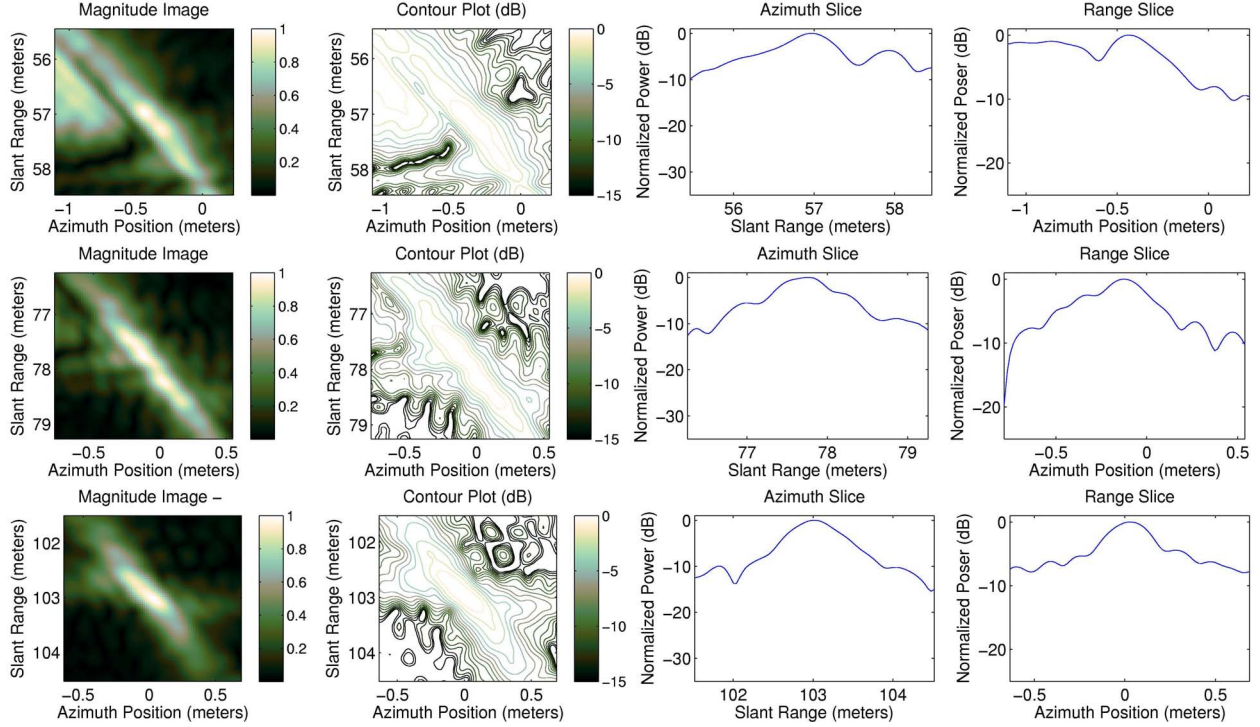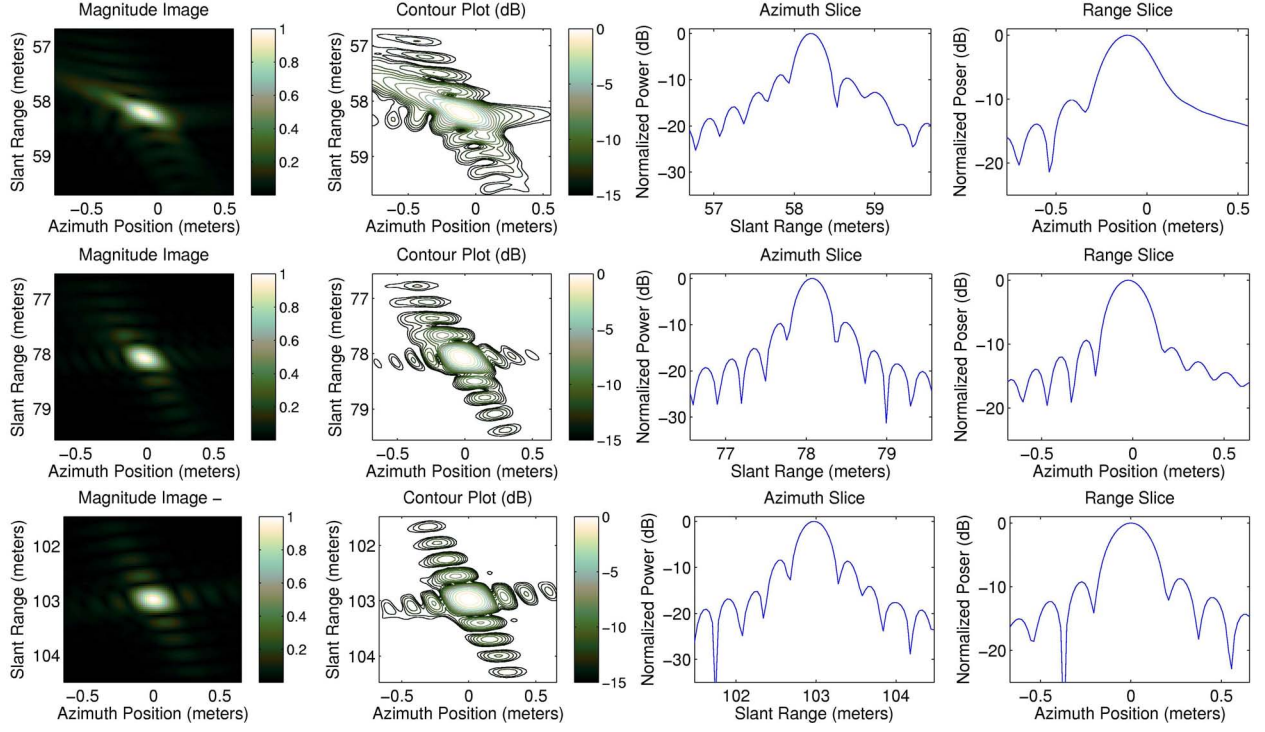
Figure 4.16: Simulated SAR data for point targets with a bandwidth from 2.5 to 3 GHz and a 20° beamwidth with a 15° squint. The data is processed with the proposed generalized FSA with $n = 3$, with the center row showing a target at the reference range. The top row shows a nearer-range target while the bottom row shows a farther-range target. The inclusion of the third order term results in slightly improved performace when compared to Fig. 4.13. The description of the columns is the same as in Fig. 4.5.

$$R_0 = R_f + R_0 - R_f = R_f + \frac{\Delta f D(f_\eta) c_0}{2k_r}. \tag{4.60}$$

We express K_m from Eq. (4.46) in terms of Δf

$$K_m = \frac{-K_f}{K_s K_f \Delta f - 1} \tag{4.61}$$

where

$$K_f = \frac{D^3(f_\eta) c_0^2}{2R_f \lambda k_r^2 \left(D^2(f_\eta) - 1\right)} \tag{4.62}$$

and

$$K_s = \frac{\left(D^2(f_\eta) - 1\right) k_r \lambda}{c_0 D^2(f_\eta)}. \tag{4.63}$$
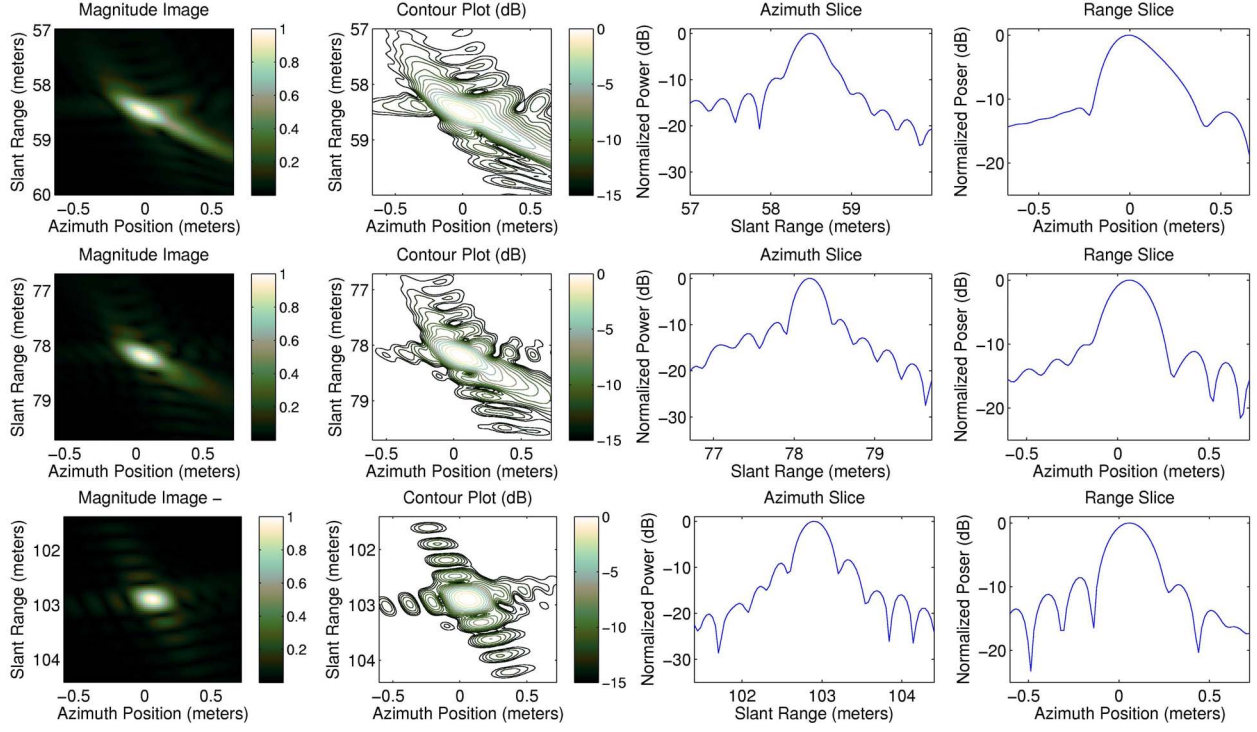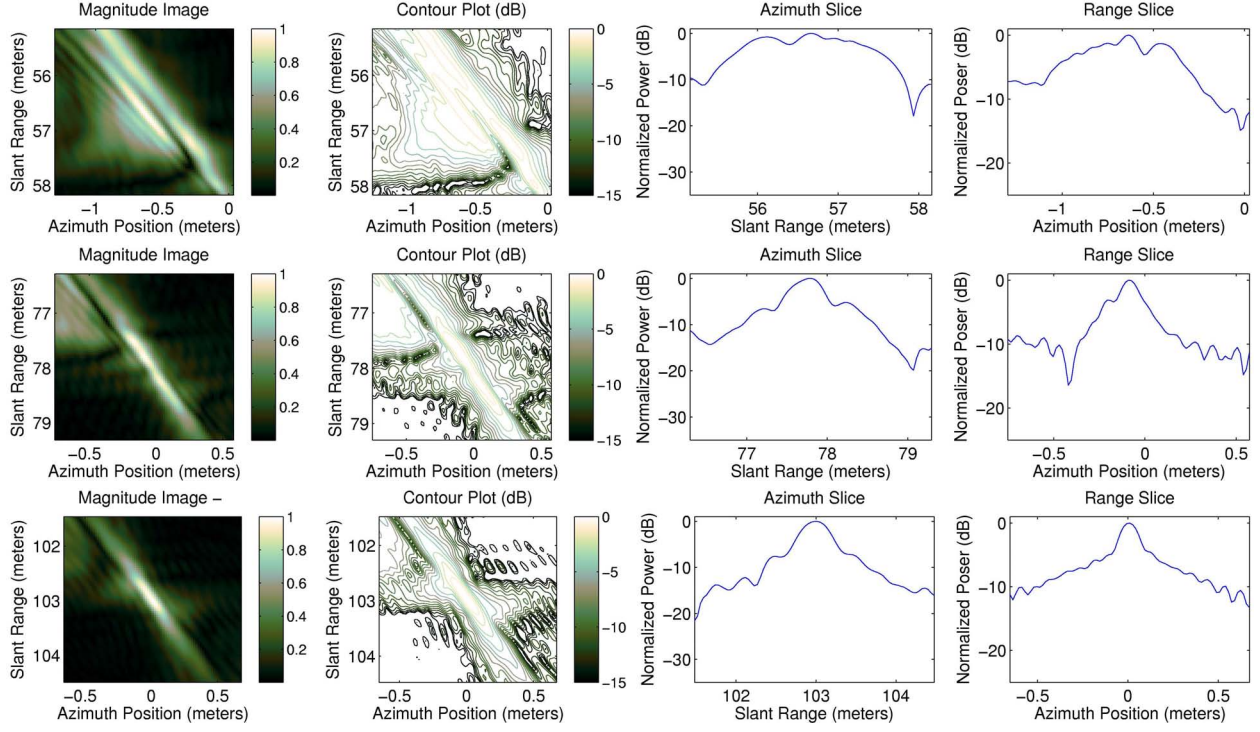
81
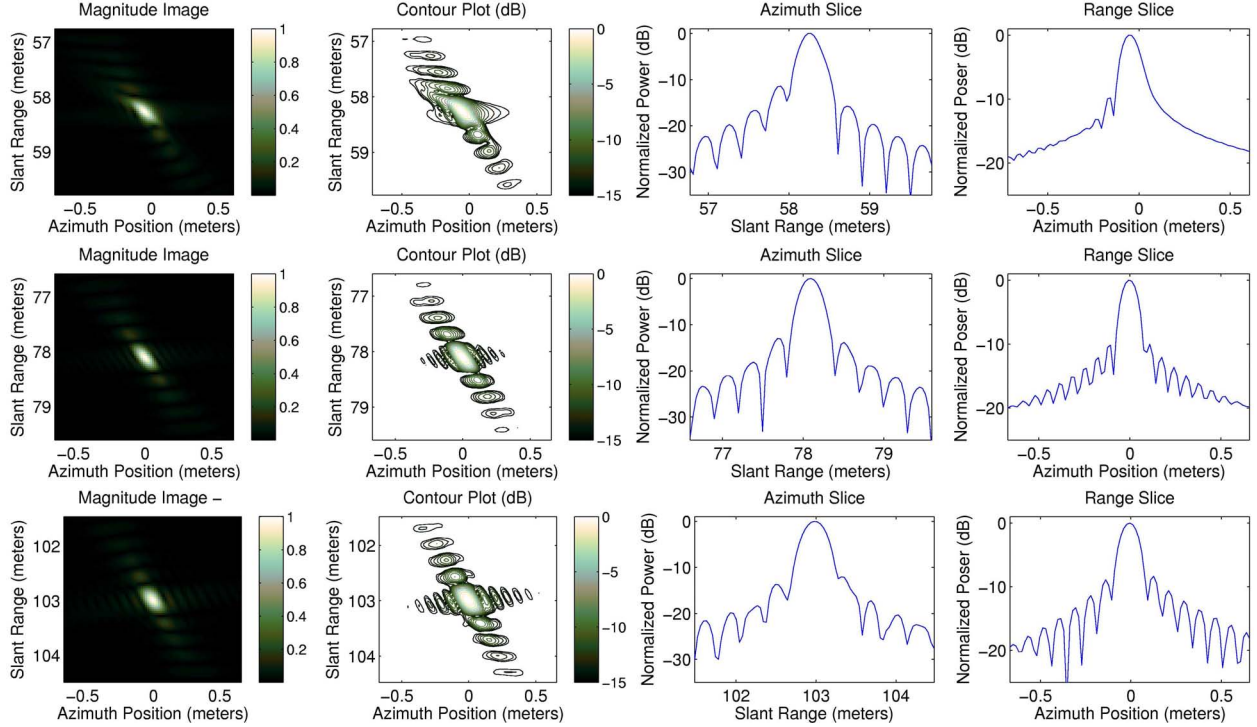
Figure 4.17: Simulated SAR data for point targets with a bandwidth from 5.5 to 6 GHz and a 20° beamwidth with a 15° squint. The data is processed with the proposed generalized FSA with $n = 3$, with the center row showing a target at the reference range. The top row shows a nearer-range target while the bottom row shows a farther-range target. The inclusion of the third order term results in slightly improved performace when compared to Fig. 4.15. The description of the columns is the same as in Fig. 4.5.

We Taylor-expand K_m in terms of Δf, retaining up to the second order,

$$K_m \approx K_f + K_s K_f^2 \Delta f + K_s^2 K_f^3 \Delta f^2. \tag{4.64}$$

Each C_i, for $i > 0$, is rearranged to be expressed as a power series of Δf, for example,

$$
\begin{aligned}
C_1 &= \left[2\pi K_f \left(D(f_\eta) - 1 \right) - 2\pi q_2 D(f_\eta) \right] \Delta f + \left[\frac{-2\pi R_f Y_3 K_f^3 (D(f_\eta) - 1)^2}{\lambda} + 3\pi q_3 D^2(f_\eta) \right. \\
&\quad - 3\pi X_3 K_f^3 \left(D(f_\eta) - 1 \right)^2 + \left. -2\pi K_s K_f^2 \left(D(f_\eta) - 1 \right) \right] \Delta f^2 \cdots . \tag{4.65}
\end{aligned}
$$

When the coefficients of Δf are equal to zero, the range variations are eliminated. We approach this by setting the linear and quadratic terms of Δf equal to zero, resulting in
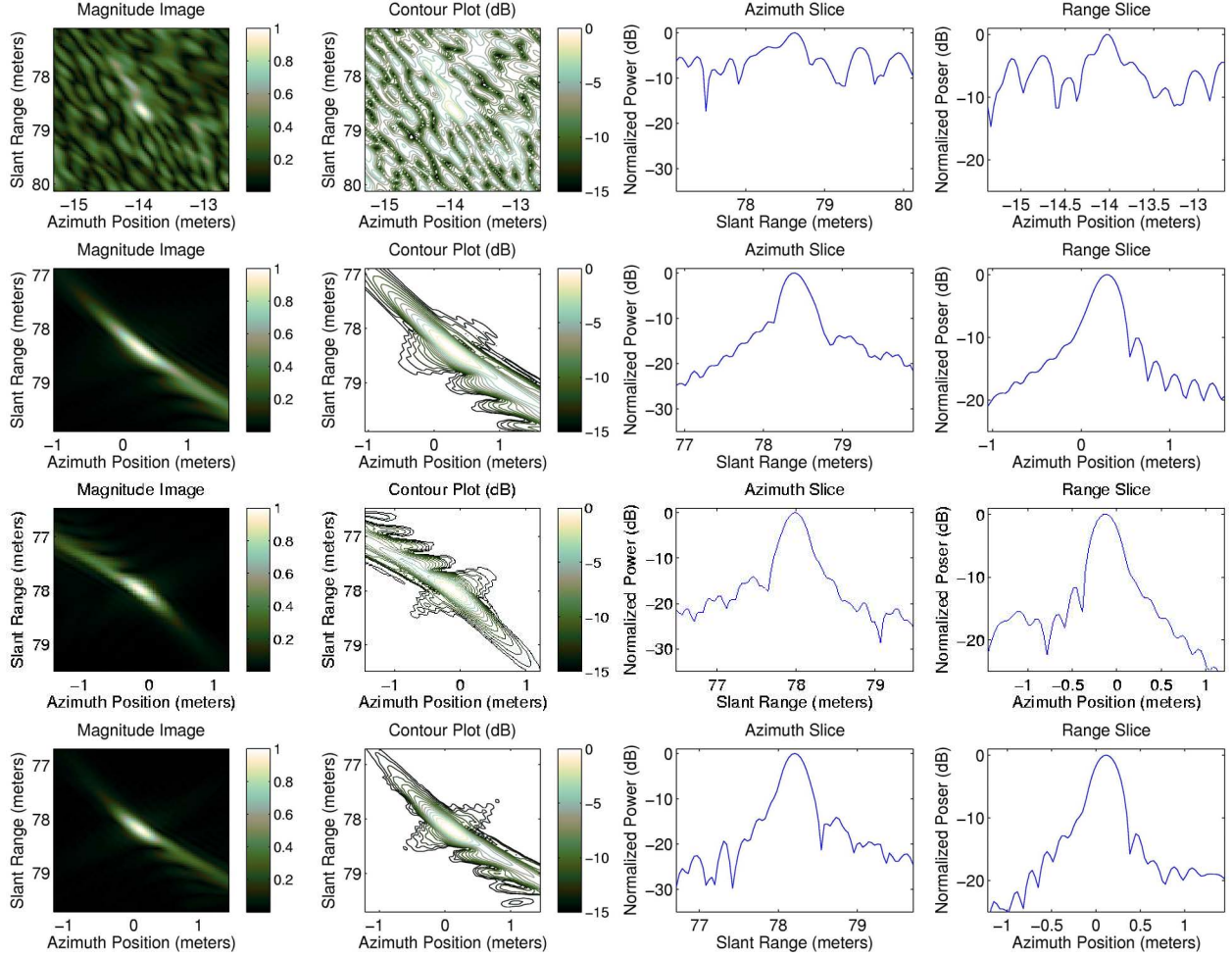
Figure 4.18: Simulated SAR data for a point target with a bandwidth from 2.5 to 3 GHz and a 20° beamwidth with a 43° squint. The top row shows the data processed using the FSA. The second row shows the results of the generalized FSA with $n = 2$. The third and fourth rows show the results of with $n = 3$ and $n = 4$ respectively. The FSA completely breaks down while the algorithm proposed in this chapter shows results improving with each additional order included in the processing. The description of the columns is the same as in Fig. 4.5.

$2n - 3$ equations and $2n - 3$ unknowns, for example

$$2\pi K_f \left(D(f_\eta) - 1 \right) - 2\pi q_2 D(f_\eta) = 0,$$

$$\frac{-2\pi R_f Y_3 K_f^3 (D(f_\eta) - 1)^2}{\lambda} + 3\pi q_3 D^2(f_\eta) - 3\pi X_3 K_f^3 \left(D(f_\eta) - 1 \right)^2 + 2\pi K_s K_f^2 \left(D(f_\eta) - 1 \right) = 0,$$

$$\frac{2\pi R_f Y_3 K_f^3 (D(f_\eta) - 1)}{\lambda} - 3\pi q_3 D(f_\eta) + 3\pi X_3 K_f^3 \left(D(f_\eta) - 1 \right) - \pi K_s K_f^2 = 0. \qquad (4.66)$$

We solve for q_i and X_i in Table 4.2.
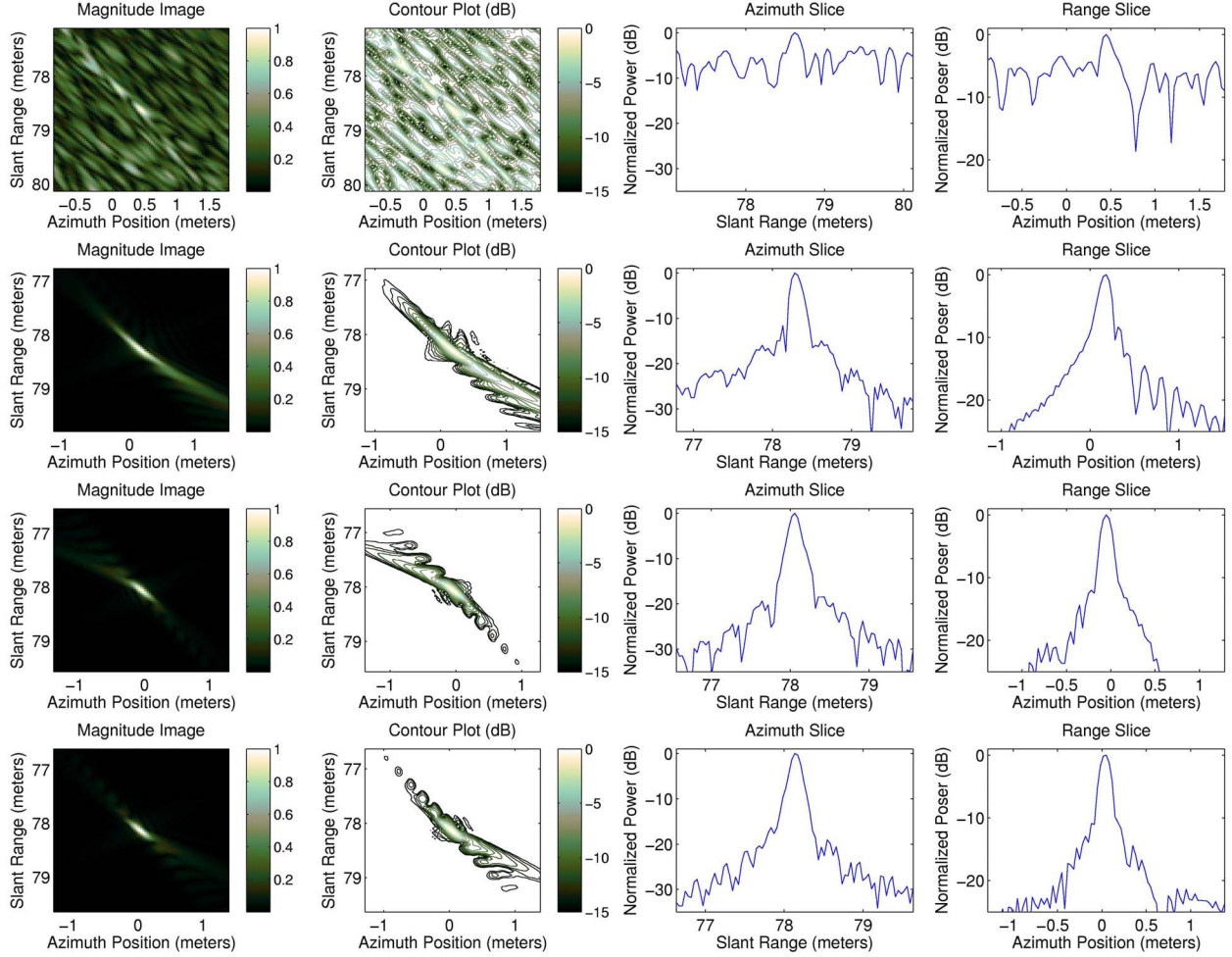
Figure 4.19: Simulated SAR data for a point target with a bandwidth from 5.5 to 6 GHz and a 20° beamwidth with a 43° squint. The top row shows the data processed using the FSA. The second row shows the results of the generalized FSA with $n = 2$. The third and fourth rows show the results of with $n = 3$ and $n = 4$ respectively. The FSA completely breaks down while the algorithm proposed in this chapter shows results improving with each additional order included in the processing. The description of the columns is the same as in Fig. 4.5.

The linear and quadratic terms of Δf in each C_i for $i > 0$ become zero, while the higher order terms are small and can be neglected. What remains of the SAR signal phase can be expressed as

$$\frac{4\pi R_0 D(f_\eta)}{\lambda} - \frac{\pi K_f (f_s - f_r)^2}{D(f_\eta)} + C_0 + \sum_{i=3}^{n} \pi \left[q_i + (-K_m)^i X_i + \frac{4R_f Y_i (-K_m)^i}{i!\lambda} \right] (f_s - f_r)^i.$$

$$(4.67)$$

An inverse Fourier transform of the signal is taken, which can be approximated using the principle of stationary phase with the stationary point found using the first two terms of Eq. (4.67),

$$\frac{d}{df_r}\left[\frac{4\pi R_0 D(f_\eta)}{\lambda} - \frac{\pi K_f (f_s - f_r)^2}{D(f_\eta)} + 2\pi f_r t\right] = 0$$

$$f_r = \frac{K_f f_s + t D(f_\eta)}{K_f}. \tag{4.68}$$

The signal phase after the inverse Fourier transform can be expressed as

$$\Phi_{s_4} = \frac{4\pi R_0 D(f_\eta)}{\lambda} + \frac{\pi t^2 D(f_\eta)}{K_f} + 2\pi t f_s + C_0 + \sum_{i=3}^{n} \frac{4\pi\left(\frac{i!}{4}q_i\lambda + R_f Y_i K_f^i + \frac{i!}{4}X_i K_f^i\lambda\right) t^i D^i(f_\eta)}{i!\lambda K_f^i}. \tag{4.69}$$

A phase filter, H_{mf}, is now applied, where

$$H_{mf} = \frac{4\pi t R_f k_r}{c_0} - 2\pi t f_{ref} - \frac{\pi t^2 D(f_\eta)}{K_f} - \sum_{i=3}^{n} \frac{4\pi\left(\frac{i!}{4}q_i\lambda + R_f Y_i K_f^i + \frac{i!}{4}X_i K_f^i\lambda\right) t^i D^i(f_\eta)}{i!\lambda K_f^i} \tag{4.70}$$

The resulting signal phase is

$$\Phi_{s_{4b}} = \frac{4\pi R_0 D(f_\eta)}{\lambda} + \frac{4\pi t R_0 k_r}{c_0} + C_0. \tag{4.71}$$

A range Fourier transform compresses the signal in range

$$\int_{\frac{2R_0}{c_0}}^{\frac{2R_0}{c_0}+T_p} s_{4b}\, e^{-j(2\pi t f_r)} dt$$

$$= \frac{-jc_0}{2\pi\left(2R_0 k_r - f_r c_0\right)} \cdot e^{j\,\frac{4\pi R_0 D(f_\eta)}{\lambda} - \frac{4\pi f_r R_0}{c_0} + \frac{8\pi R_0^2 k_r}{c_0^2} + C_0 - 2\pi f_r T_p} \cdot \left[e^{j2\pi f_r T_p} - e^{j\,\frac{4\pi R_0 k_r T_p}{c_0}}\right]$$

$$= T_p \cdot \mathrm{sinc}\left(\frac{\pi T_p\left(f_r c_0 - 2R_0 k_r\right)}{c_0}\right) \cdot e^{j\,\frac{4\pi R_0 D(f_\eta)}{\lambda} - \frac{4\pi f_r R_0}{c_0} + \frac{8\pi R_0^2 k_r}{c_0^2} + C_0 - \pi f_r T_p + \frac{2\pi R_0 k_r T_p}{c_0}}. \tag{4.72}$$

The last two terms in the exponential on the last line of Eq. (4.72) are zero at the peak of the sinc function, and can be ignored.

The final azimuth matched filter is now applied

$$H_{az} = -\frac{4\pi R_0 D(f_\eta)}{\lambda} + \frac{4\pi f_r R_0}{c_0} - \frac{8\pi R_0^2 k_r}{c_0^2} - C_0 \qquad (4.73)$$

and an inverse Fourier transform results in the focused image.

Examples of the results of the new algorithm are illustrated as follows: Figs. 4.10 and 4.11 show a comparison between a simulated point target with two different sets of mild SAR parameters processed with the traditional FSA and with the proposed generalized algorithm with only a second order approximation. Figs. 4.12 and 4.14 show a set of point targets at different ranges with a 15° squint and the same SAR parameters as Figs. 4.10 and 4.11 and processed with the traditional FSA. The squint makes it so that the SAR data can no longer be accurately modeled by the approximations made in the FSA. Figs. 4.13 and 4.15 offer greatly improved performace using the proposed algorithm with a second order approximation to process the data. This comes with a little extra processing burden (20% more processing time). Including the third order term further improves the performance, as shown in Figs. 4.16 and 4.17, while approximately doubling the processing time.

If we simulate SAR data at an even larger squint angle ($> 40°$), the traditional FSA hardly works at all. In Figs. 4.18 and 4.19 we observe the focus improving as additional terms from the Taylor series expansion are included in the processing.

4.4 Summary

While the continuous motion of the radar platform creates some unwelcome issues for processing LFM-CW SAR data, the problems can be dealt with, allowing for precision processing in a variety of applications. The failings of approximations made in deriving traditional SAR processing algorithms can be overcome by taking a general approach to the LFM-CW SAR signal. This chapter has demonstrated a robust continuous motion correction for arbitrary flight paths, both precise and approximate LFM-CW SAR backprojection algorithms, and a generalized FSA allowing for an arbitrary number of terms from a Taylor series expansion. These algorithms extend the utility of LFM-CW SAR systems, allowing operation with a wider variety of system parameters and in nearly any imaging scenario.

Table 4.1: Nth-Order Generalized Frequency-Scaling Algorithm (GFSA) Processing Flow

Action	Parameter Value
1. Digitize SAR Signal $\rightarrow s_{dc0}$	$s_{dc0}(t, \eta) = e^{j\left(2\pi k_r t\tau + 2\pi f_0\tau - \pi k_r\tau^2\right)}$
2. 2D FFT $\rightarrow S_1$	
3. RVP Removal: $S_1 e^{j\Phi_{RVP}}$	$\Phi_{RVP} = \frac{\pi f_r^2}{k_r}$
4. Range IFFT $\rightarrow s_2$	
5. Motion Compensation and Pre-Filter: $s_2 e^{j(\Phi_{mc}+\Phi_{pre})}$	$\Phi_{mc} = -2\pi t f_\eta$ $\Phi_{pre} = \sum_{i=3}^{n} \pi X_i t^i$
6. Range FFT $\rightarrow S_3$	
7. Scaling Filter: $S_3 e^{j\Phi_{scale}}$	$\Phi_{scale} = \sum_{i=2}^{n} \pi q_i \left(f_{ref} - f_r\right)^i$
8. Range IFFT $\rightarrow s_4$	
9. Matched Filter: $s_4 e^{j\Phi_{mf}}$	$\Phi_{mf} = \frac{4\pi t R_f k_r}{c_0} - 2\pi t f_{ref} - \frac{\pi t^2 D(f_\eta)}{K_f} - \sum_{i=3}^{n} \frac{4\pi\left(\frac{i!}{4}q_i\lambda + R_f Y_i K_f^i + \frac{i!}{4}X_i K_f^i\lambda\right)t^i D^i(f_\eta)}{i!\lambda K_f^i}$
10. Range FFT $\rightarrow S_5$	
11. Azimuth Filter: $S_5 e^{j\Phi_{az}}$	$\Phi_{az} = -\frac{4\pi R_0 D(f_\eta)}{\lambda} + \frac{4\pi f_r R_0}{c_0} - \frac{8\pi R_0^2 k_r}{c_0^2} - C_0$
12. Azimuth IFFT $\rightarrow s_6$	

Table 4.2: Nth-Order Generalized Frequency-Scaling Algorithm (GFSA) Solved Parameters

$$q_2 = \frac{K_f(D(f_\eta)-1)}{D(f_\eta)} \ , \quad q_3 = \frac{-(D(f_\eta)-1)K_s K_f^2}{3D(f_\eta)}, \quad X_3 = \frac{-\left(D(f_\eta)Ks\lambda + 2R_f Y_3 D(f_\eta)K_f - 2K_s\lambda - 2R_f Y_3 K_f\right)}{3K_f\lambda(D(f_\eta)-1)}$$

$$q_4 = \frac{-(c_0 D(f_\eta)^2 Y_3 - c_0 D(f_\eta)Y_3 + 9X_3 D(f_\eta)K_s K_f k_r \lambda + 6R_f Y_3 D(f_\eta)K_s K_f k_r - 9X_3 K_s K_f k_r \lambda - 2K_s^2 k_r \lambda - 6R_f Y_3 K_s K_f k_r)K_f^3}{12k_r \lambda D(f_\eta)}$$

$$X_4 = \frac{9X_3 K_s K_f k_r \lambda(D(f_\eta)-2) + Y_3(D(f_\eta)-2)\left(c_0 D(f_\eta)+6R_f K_s K_f k_r\right) - 2K_f k_r R_f Y_4(D(f_\eta)-1) - 2K_s^2 k_r \lambda}{12K_f k_r \lambda(D(f_\eta)-1)}$$

$$q_5 = \frac{\left(36X_3 K_s^2 K_f k_r \lambda + 48k_r X_4 K_s K_f \lambda(D(f_\eta)-1) + 6Y_3 K_s\left(4R_f K_s K_f k_r + c_0 D(f_\eta)\right) + Y_4(D(f_\eta)-1)(c_0 D(f_\eta)+8R_f K_s K_f k_r)\right)K_f^4}{60k_r \lambda D(f_\eta)}$$

$$X_5 = \frac{36X3 K_s^2 K_f k_r \lambda + 48k_r X4 K_s K_f \lambda(D(f_\eta)-2) - 2Y_5 k_r R_f K_f(D(f_\eta)-1) + 6Y_3 K_s\left(4R_f K_s K_f k_r + c_0 D(f_\eta)\right) + Y_4(D(f_\eta)-2)\left(c_0 D(f_\eta)+8R_f K_s K_f k_r\right)}{60K_f k_r \lambda(D(f_\eta)-1)}$$

CHAPTER 5.   MOTION COMPENSATION FOR LFM-CW SAR

Very small low-cost SAR systems have recently been demonstrated as an alternative to expensive and complex traditional systems [41, 42, 45, 47, 58, 59, 60]. The use of a frequency modulated continuous wave (FMCW) signal facilitates system miniaturization and low-power operation which make it possible to fly these systems on small UAV's. The ease of operation and low operating costs make it possible to conduct extensive SAR studies without a large investment.

Recently, new processing methods have been developed to address issues specific to FMCW SAR [51]. The Range-Doppler Algorithm (RDA) [61] and the Frequency (or Chirp) Scaling Algorithm (FSA or CSA) [50] can be modified to compensate for the constant forward motion during the FMCW chirp. Non-linearities in the chirp can also be corrected [62], and squint mode data can be processed [63]. In this chapter the problems caused by non-ideal motion of an LFM-CW SAR are addressed and new compensation algorithms are developed.

Stripmap SAR processing assumes that the platform is moving in a straight line, at a constant speed, and with a consistent geometry with the target area. During data collection, whether in a manned aircraft or a UAV, there are deviations from this ideal as the platform changes its attitude, speed, or is subjected to turbulence in the atmosphere. These displacements introduce variations in the phase history, the signal's time of flight to a target, and the sample spacing, all of which degrade the image quality. If the motion of the platform is known, then corrections can be made to the SAR data for more ideal image processing. Small aircraft and UAV's are more susceptible to atmospheric turbulence, thus the need for motion compensation on these platforms is greater.

Motion compensation algorithms for traditional pulsed SAR have been extensively studied [64, 65], but the underlying differences with an LFM-CW signal make it a challenge to extend existing motion compensation methods to LFM-CW sensors. In pulsed SAR, the

platform is assumed to be stationary during each pulse and the motion takes place between pulses. With an LFM-CW SAR, the signal is constantly being transmitted and received, thus the motion takes place during the chirp.

This chapter presents the development of new motion compensation algorithms, suitable for use with both the RDA and the FSA (or CSA), that account for the motion during the chirp. The proposed algorithms also correct the range shift introduced by translational motion of magnitude greater than a single range bin without interpolation. First, in Section 5.1, the theoretical underpinnings of LFM-CW SAR and developed and processing methods described. Section 5.2 shows the effects of non-ideal motion. In Section 5.3 theoretic correction algorithms are developed and made practical through simplifying assumptions.

Section 5.4 presents simulation results in which a SAR system images a few point targets with non-ideal motion. The known deviations are used to compensate for the effects of the non-ideal motion in the simulated data. A quantitative analysis of the simulation results is performed which compares the proposed motion compensation algorithm to the traditional method. The new motion compensation scheme is applicable to a number of FMCW SAR systems which are summarized in Section 5.5. The developed algorithm is applied to actual data from the Brigham Young University (BYU) μSAR data and the results are presented. Motion data is provided by an inertial navigation system and GPS. The flight path data is interpolated between samples to provide position data for each sample of SAR data. The motion data is used to determine the necessary corrections which are introduced into the SAR data, effectively straightening the flight path.

5.1 LFM-CW SAR Signal Processing

In a symmetric LFM-CW chirp the frequency of the signal increases from a starting frequency ω_0, and spans the bandwidth BW, at the chirp rate $k_r = BW \cdot 2 \cdot PRF$. The frequency then ramps back down as seen in Fig. 5.1. This up-down cycle is repeated at the PRF, giving a PRI of T_p. The transmitted up-chirp signal can be expressed in the time domain, where t is fast-time and η is slow time, as

$$s_t(t,\eta) = e^{j(\phi + \omega_0 t + \pi k_r t^2)}, \tag{5.1}$$
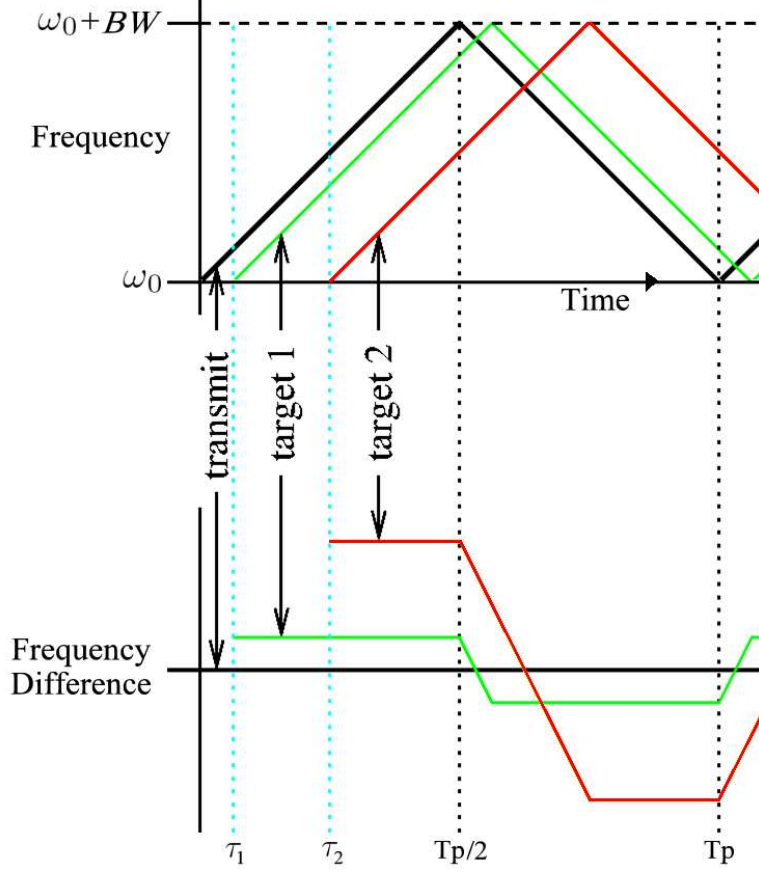
Figure 5.1: The frequency change of a symmetric LFM-CW signal over time is shown above, together with the signal returns from two separate targets. The frequencies of the de-chirped signal are shown below, with the times of flight, τ_1 and τ_2, due to range determining the de-chirped frequency. The relative sizes of τ_1, τ_2, and T_p are exaggerated for illustrative purposes.

where ϕ is the initial phase. The down chirp is similar with $\omega_0 + BW$ being the starting frequency and $-k_r$ the chirp rate.

The received signal from a target at range $R(t, \eta) = \sqrt{R_0^2 + v^2(t + \eta)^2}$, with time delay $\tau = 2R(t, \eta)/c$ is

$$s_r(t, \eta) = e^{j(\phi + \omega_0(t - \tau) + \pi k_r(t - \tau)^2)} \tag{5.2}$$

where R_0 is the range of closest approach of the target.

The transmit signal is mixed with the received signal and low-pass filtered in hardware, which is mathematically equivalent to multiplying Eq. (5.1) by the complex conjugate

91
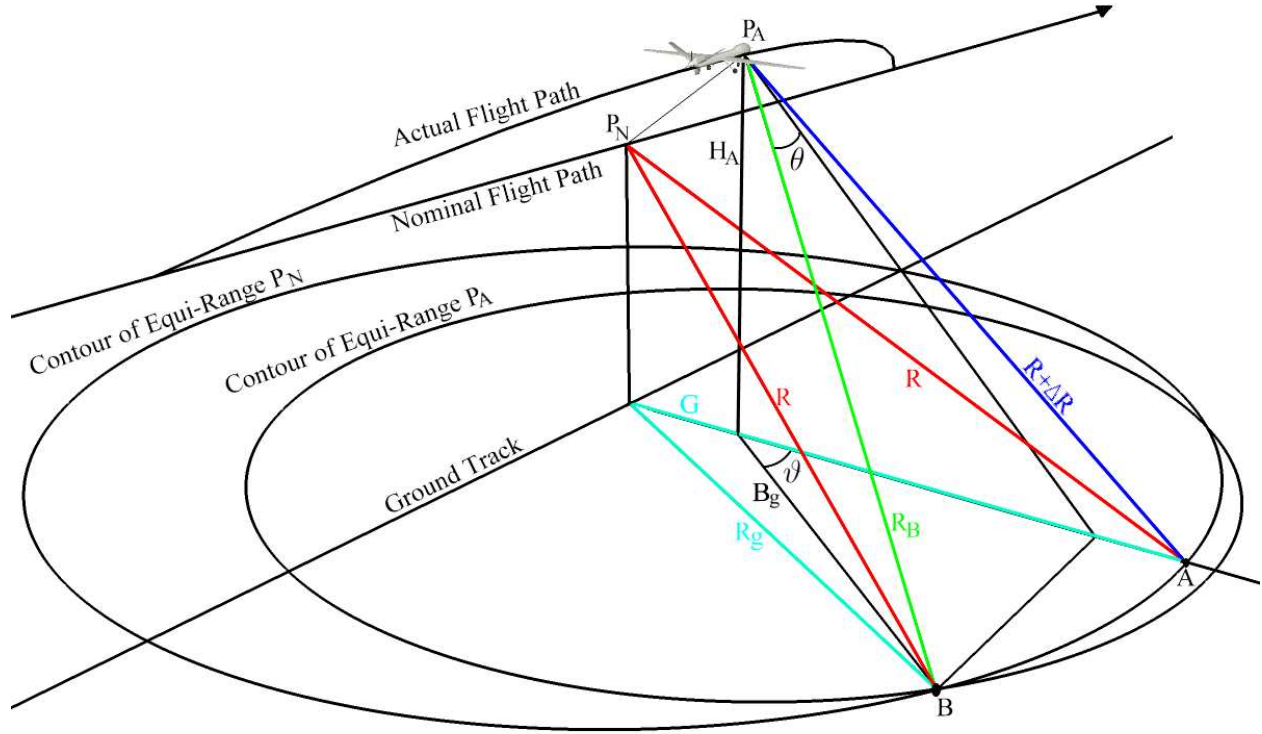
Figure 5.2: The SAR platform deviates from its nominal path, point P_N, resulting in a change in range to point A from R to $R + \Delta R$. Point B is nominally at a range R, but the deviation to point P_A changes the range to R_B, which is different from $R + \Delta R$.

of Eq. (5.2). This results in the de-chirped signal

$$s_{dc}(t, \eta) = e^{j(\omega_0 \tau + 2\pi k_r t \tau - \pi k_r \tau^2)}. \tag{5.3}$$

This raw data is then processed to create a SAR image.

Options for data processing include the RDA and the FSA (or CSA), as shown in Fig. 5.4. For RDA processing, this signal is range compressed with an FFT in the range direction then taken to the range-Doppler domain with an FFT in the azimuth direction. Using standard interpolation methods the range cell migration (RCM) can be compensated, but this is computationally costly. The Doppler shift introduced by the continuous forward motion of the platform can also be removed [61]. The azimuth compression is performed by

multiplying by the azimuth matched filter

$$H_{az}(f_\eta, R_0) = e^{j\frac{4\pi R_0}{\lambda}D(f_\eta, v)}. \tag{5.4}$$

where $D(f_\eta, v) = \sqrt{1 - \lambda^2 f_\eta^2/4v^2}$ is the range migration factor, v is the platform along-track velocity, and λ is the wavelength of the center transmit frequency.

Alternatively, the Frequency (or Chirp) Scaling Algorithm (FSA or CSA) [8] can also be modified to work with the de-chirped data [57]. With the FSA, the RCM can be compensated for without interpolation. This advantage makes FSA the preferred method for LFM-CW SAR processing. Fig. 5.3 compares the RDA (without RCM correction) and the FSA in processing data from the BYU μSAR.

FSA processing involves a series of Fourier transforms and phase multiplies. If a known non-linearity exists in the FMCW chirp, it can be compensated by modifying the functions as in [50]. To start the FSA processing, an FFT is performed in the azimuth direction on the signal from Eq. (5.3). The resulting signal in the de-chirped-Doppler domain is

$$S(t, f_\eta) = e^{-j\frac{4\pi R_0 D(f_\eta, v)}{\lambda}} e^{-j\frac{4\pi k_r R_0 t}{cD(f_\eta, v)}} e^{j2\pi f_\eta t} e^{-j\pi k_r t^2}. \tag{5.5}$$

The frequency scaling function is applied with an additional term that removes the Doppler shift [50],

$$H_1(t, f_\eta) = e^{-j(2\pi f_\eta t + \pi k_r t^2(1 - D(f_\eta, v)))}. \tag{5.6}$$

A range FFT is performed and the second function is applied which corrects the residual video phase,

$$H_2(f_r, f_\eta) = e^{(-j\pi f_r^2)/(k_r D(f_\eta, v))}. \tag{5.7}$$

An inverse FFT in the range direction is performed followed by a function that performs an inverse frequency scaling,

$$H_3(t, f_\eta) = e^{-j\pi k_r t^2[D(f_\eta, v)^2 - D(f_\eta, v)]}. \tag{5.8}$$
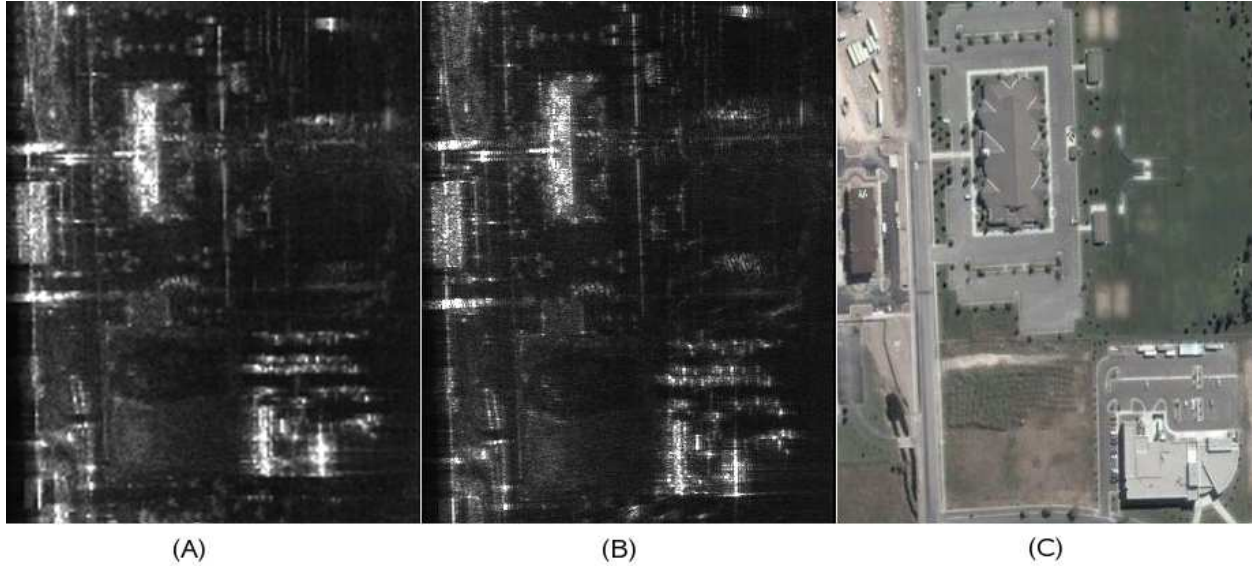
Figure 5.3: Taken from a larger image, a 286 m x 360 m area of North Logan, Utah is shown. Imaged with the BYU μSAR operating at 5.62 GHz with a bandwidth of 80 MHz, the data was processed with the RDA and the FSA. The horizontal axis is slant range with the aircraft moving upward at image left. (A) shows the RDA processed data, without RCM correction (the entire collection was processed in 30.4 seconds). (B) was processed with the FSA (the entire collection took 84.3 seconds to process). (C) shows a aerial photograph for comparison. It is clear that the focusing is better with the FSA, and worth the extra processing load.

Here the secondary range correction and bulk range shift phase function can be used, as in [57].

We again take the range FFT and apply the final filter that performs the azimuth compression, Eq. (5.4). An azimuth IFFT results in the final focused image.

5.2 Non-Ideal Motion Errors

The SAR processing algorithms described in Section 5.1 assume that the platform moves at a constant speed in a straight line. In any actual data collection this is not the case, as the platform experiences a variety of deviations from the ideal path. These deviations introduce errors in the collected data which degrade the SAR image.

Translational motion causes platform displacement from the nominal, ideal path. This results in the target scene changing in range during data collection. This range shift

also causes inconsistencies in the target phase history. A target at range R is measured at range $R + \Delta R$ resulting in a frequency shift in the de-chirped data. The de-chirped signal in Eq. (5.3) then becomes

$$s_{\Delta dc}(t, \eta) = e^{j(\omega_0(\tau+\Delta\tau)+2\pi k_r t(\tau+\Delta\tau)-\pi k_r(\tau+\Delta\tau)^2)}. \tag{5.9}$$

where $\Delta\tau = 2\Delta R/c$. Targets that lie within the beamwidth that have a non-zero Doppler frequency experience a different change in range dependent on the azimuth position. This is illustrated in Fig. 5.2 where the range to target A changes with motion differently than the range to target B.

Variations in along-track ground speed result in non-uniform spacing of the radar pulses on the ground. This non-uniform sampling of the Doppler spectrum results in erroneous calculations of the Doppler phase history.

Changes in pitch, roll, and yaw introduce errors of a different kind. The pitching displaces the antenna footprint on the ground, the roll changes the antenna gain pattern over the target area, and the yaw introduces a squint. Pitch and yaw shift the Doppler centroid, with the shift being range dependent in the yaw case. If the Doppler spectrum is shifted so that a portion lies outside the Doppler bandwidth, then aliasing occurs. The azimuth compression produces ghost images at the azimuth locations where the Doppler frequency is aliased to zero.

5.3 Motion Compensation

Previously developed methods of motion compensation are limited for correcting the non-ideal motion of an LFM-CW SAR system. Methods like those of [21] apply a bulk motion compensation to the raw data and a secondary correction to the range compressed data. This works as an approximation for motion correction, but relies on assuming the platform is stationary during a pulse. In range compressing the data, we lose the ability to differentiate the motion over the chirp, which is problematic for LFM-CW SAR.

For an LFM-CW SAR signal, the motion corrections can be applied directly to the raw de-chirped data (Eq. 5.9) or Doppler dependent corrections are applied to the azimuth

FSA

Dechirped LFM-CW Signal

$s_{dc}(t,\eta)$

1st Order Motion Compensation ⊗ ← $H_{mc1}(t, \Delta\tau_{ref})$

| Azimuth FFT |

Frequency Scaling ⊗ ← $H_1(t, f_\eta)$

| Range FFT |

RVP Correction ⊗ ← $H_2(f_r, f_\eta)$

| Range IFFT |

Inverse Frequency Scaling and SRC ⊗ ← $H_3(t, f_\eta)$, H_{SRC}

| Range FFT |

| Azimuth IFFT |

2nd Order Motion Compensation ⊗ ← $H_{mc2}(\tau_0, \Delta\tau_0)$

| Azimuth FFT |

Azimuth Compression ⊗ ← $H_{az}(t, f_\eta)$

| Azimuth IFFT |

Final Compressed Image

RDA

Dechirped LFM-CW Signal

$s_{dc}(t,\eta)$

1st Order Motion Compensation ⊗ ← $H_{mc1}(t, \Delta\tau_{ref})$

| Range FFT |

2nd Order Motion Compensation ⊗ ← $H_{mc2}(\tau_0, \Delta\tau_0)$

| Azimuth FFT |

RCMC

Azimuth Compression ⊗ ← $H_{az}(t, f_\eta)$

| Azimuth IFFT |

Final Compressed Image

Figure 5.4: Block diagram showing LFM-CW SAR processing using the FSA (left) and RDA (right) including the proposed two-step motion compensation.

FFT of the raw data, in the de-chirped-Doppler domain. Because each data point contains information from every range, and the corrections are range and azimuth dependent, any corrections applied in the de-chirped-Doppler domain are valid for only one single range and one azimuth value. However, with approximations these restrictions can be relaxed.

5.3.1 Theoretical Treatment

In general, motion data is collected at a much slower rate than SAR data. For LFM-CW SAR the motion data must be interpolated so that every sample of SAR data has corresponding position information (as opposed to only each pulse having position data). Each data point also needs to have a corresponding location on the ideal path to which the error is corrected. For a target at range R, ΔR is calculated from the difference between the distance to the ideal track and the actual track. The flat-terrain geometry of Fig. 5.2 is assumed. If more precise knowledge of the terrain is available then the model can be adjusted [66, 67]. Knowing the coordinates of target A, the actual flight path (point P_A), and the nominal flight path (point P_N), the distances R and $R + \Delta R$ can be calculated from geometry. Again $\Delta \tau = 2 \Delta R / c$, but $\Delta \tau$ is updated for every data sample. The motion errors are corrected using our correction filter

$$H_{MC}(t, \Delta \tau) = e^{-j(\omega_0 \Delta \tau + 2\pi k_r t \Delta \tau - \pi k_r(2\tau \Delta \tau - \Delta \tau^2))}. \tag{5.10}$$

When applied to the data (in the raw de-chirped time domain or the de-chirped Doppler domain), this shifts the range of the target and adjusts the phase.

There are targets in the beamwidth at the same range but different azimuth positions that experience a different range shift due to translational motion. For a given azimuth position, as shown in Fig. 5.2, target B is at a position where it has the Doppler frequency f_η. The angle to target B is

$$\theta(f_\eta) = \sin^{-1}\left(\frac{f_\eta \lambda}{2v}\right). \tag{5.11}$$

Working through some particularly unpleasant geometry, the angle on the ground (as defined in Fig. 5.2) $\vartheta(\theta(f_\eta), R_g, G, H_A)$ is found. The range $R + \Delta R$ and the angle θ are derived from the SAR data and the height H_A and the range R are found from the motion data. We define a right triangle on the ground with hypotenuse B_g and sides $B_g \cdot \cos(\vartheta)$ and $B_g \cdot \sin(\vartheta)$. We

take the angle ϕ to be between the lines R_g and G. From this we get the following equalities:

$$\sin(\phi) = \frac{B_g \cdot \sin(\vartheta)}{R_g}, \tag{5.12}$$

$$\cos(\phi) = \frac{G + B_g \cdot \cos(\vartheta)}{R_g}, \tag{5.13}$$

$$\arcsin\left(\frac{B_g \cdot \sin(\vartheta)}{R_g}\right) = \arccos\left(\frac{G + B_g \cdot \cos(\vartheta)}{R_g}\right). \tag{5.14}$$

This gives us two unknowns, B_g and ϑ. We introduce another equation:

$$\tan(\theta) = \frac{B_g \cdot \sin(\vartheta)}{\sqrt{(B_g \cdot \cos(\vartheta))^2 + H_A{}^2}}. \tag{5.15}$$

Eqs. 5.14 and 5.15 are simultaneously solved for ϑ and B_g. The closed form solution can be easily found using a symbolic solver. Unfortunately, the resulting equation is too large to be printed here. However tedious the solution may be, given the input values, a computer has no difficulty in producing the correct result.

From ϑ we find the ground range,

$$B_g(f_\eta) = -\cos(\vartheta)G \pm \sqrt{\cos^2(\vartheta)G^2 + R_g^2 - G^2}, \tag{5.16}$$

and the actual range to target B,

$$R_B(f_\eta) = \sqrt{H_A^2 + B_g^2}. \tag{5.17}$$

We then find $\Delta R = R - R_B(f_\eta)$, $\Delta\tau = 2\Delta R(f_\eta)/c$, and apply Eq. (5.10) in the de-chirped-Doppler domain. This correction is valid for a single range and azimuth position.

Exactly correcting the motion errors in this way is computationally taxing. For every pixel of the final image, the correction is applied in the de-chirped-Doppler domain for the given range and azimuth position. The data is processed through range compression and a single data point is kept. A composite range compressed image is created from these individual points, and the final image is formed through azimuth compression. Fortunately there are approximations that can be made to reduce the computational load while still maintaining the advantages of this method.

5.3.2 Simplifying Approximations

If the beamwidth is narrow, then the errors due to motion can be assumed to be constant for a given range across the Doppler bandwidth. This is the center-beam approximation [68] and is used in many motion compensation algorithms. The errors induced by this approximation are detailed in [27]. A number of methods have been proposed as alternatives to this approximation, they are discussed in [69]. When using this approximation, we apply the correction filter (Eq. 5.10) to the raw data. The correction is valid for only a single range, thus a composite range compressed image is created and then azimuth compressed to form the final image.

Further simplification is possible by splitting the correction into two steps. The first step applies the correction for a reference range R_{ref}. ΔR_{ref} is calculated as before with $\Delta\tau_{ref} = 2\Delta R_{ref}/c$ and $\tau_{ref} = 2R_{ref}/c$. The correction is then

$$
\begin{aligned}
H_{MC1}(t, \Delta\tau_{ref}) \ = \ &\exp(-j(\omega_0\Delta\tau_{ref} + 2\pi k_r t\Delta\tau_{ref} \\
&-\pi k_r(2\tau_{ref}\Delta\tau_{ref} - \Delta\tau_{ref}^2))).
\end{aligned}
\tag{5.18}
$$

The second step applies a differential correction after range compression. For this step, position information is averaged over each pulse. This is due to the fact that when LFM-CW data is range compressed, each range bin is formed from data that spans the entire pulse. This second order correction is calculated for each range bin R_0 with a calculated ΔR_0, $\Delta\tau_0 = 2\Delta R_0/c$, and $\tau_0 = 2R_0/c$. It is simply $H_{MC}(t, \Delta\tau_0)/H_{MC}(t, \Delta\tau_{ref})$ or

$$
\begin{aligned}
H_{MC2}(\tau_0, \Delta\tau_0) \ = \ &\exp(j(-\omega_0\Delta\tau_0 + 2\pi k_r \tau_0\Delta\tau_0 \\
&-\pi k_r\Delta\tau_0^2 + \omega_0\Delta\tau_{ref} - 2\pi k_r \\
&\tau_{ref}\Delta\tau_{ref} + \pi k_r\Delta\tau_{ref}^2)).
\end{aligned}
\tag{5.19}
$$

This is similar to the traditional motion compensation model but with a couple of advantages. The motion during the pulse is still considered in applying the initial correction, thus making it suitable for LFM-CW SAR. Also, the range shift caused by translational

Table 5.1: Simulation Parameters

Chirp Bandwidth (MHz)	250
Center Frequency (GHz)	5.62
Azimuth Beamwidth	12°
Pulse Repetition Frequency (Hz)	320
Sample Rate (Hz)	327680

Table 5.2: Theoretic Values

Range Resolution (meters)	0.5996
Azimuth Resolution (meters)	0.1274

motion is corrected without interpolation. Fig. 5.5 shows simulated point targets focused by correcting the non-ideal motion using this method.

The errors introduced by this two-step approximate method are much less than the errors from the traditional method. We denote the phase error caused by approximations in the motion correction function as

$$\phi_E = \frac{4\pi \Delta R_e}{\lambda} \tag{5.20}$$

where ΔR_e is the error in the calculation of the required correction due to translational motion. For the proposed correction there is no error caused by the motion during the chirp while for traditional motion compensation, the first order correction has the error

$$\Delta R_{e1} = \Delta R_{ref}(t) - \Delta R'_{ref} \tag{5.21}$$

where $\Delta R_{ref}(t)$ is the time varying translational motion correction that takes into account motion during the chirp and $\Delta R'_{ref}$ is a constant for each pulse. For a SAR with the parameters listed in Table 5.1, with a velocity of 25 m/s and translational motion of 0.5 m over 10 m of along-track distance, the maximum phase error is calculated to be 0.4598 radians.

Table 5.3: Measured Simulation Values

	Ideal Collection	Traditional Correction	Proposed Correction
Range			
Resolution (m)	0.647	0.919	0.6048
PSLR (dB)	13.37	18.49	13.77
ISLR (dB)	10.69	12.79	10.83
Azimuth			
Resolution (m)	0.313	0.358	0.309
PSLR (dB)	14.49	11.93	9.70
ISLR (dB)	10.62	12.57	7.99
Processing Time (s)	7.525	10.691	10.677

For the second order motion compensation, the error is the same for both the proposed motion compensation scheme and the traditional method. It is calculated

$$\Delta R_{e2} = (\Delta R_{ref}(t) - \Delta R_0(t)) - (\Delta R'_{ref} - \Delta R'_0) \qquad (5.22)$$

where $\Delta R'_{ref}$ and $\Delta R'_0$ are constant over the chirp. As an example, using the same 0.5 m translational error with a platform height of 100 m, a reference range of 141.4 meters and a target range of 111.8 m. The maximum second order phase error is calculated to be 0.0238 radians. This is the total error of the proposed method. Thus we see that the proposed method has a phase error an order of magnitude less than traditional motion compensation.

5.4   Motion Compensation of Simulated Data

Fig. 5.5 and Table 5.3 show the results of an analysis of simulated LFM-CW SAR data. An array of point targets is used for qualitative analysis and a single point target is used for quantitative analysis. The proposed motion compensation algorithm is compared to the traditional motion compensation in the presence of severe translation motion and to an ideal collection made with ideal motion. The proposed motion compensation results are very near the ideal and much better than the traditional method. Of note are the measured improvement in range resolution (51%) and azimuth resolution (15%). The theoretic azimuth

resolution is not reached, even with ideal motion, because of defocusing due to the change in wavelength over the chirp.

5.5 FMCW SAR Systems

The proposed motion compensation scheme is suitable for a number of recently developed FMCW SAR systems. The BYU μSARs are small, student-built, low-power, LFM-CW SAR systems [45]. They weigh less than 2 kg, including antennas and cabling, and consume 18 watts of power. The μSAR systems operate at C-band or L-band with bandwidths of 80-160 MHz. Units have been successfully flown in manned aircraft and on UAV's. Imaged areas include the arctic and areas in Utah and Idaho. The BYU μSAR is flown with an MMQ-G INS/GPS unit from Systron Donner Inertial which measures the motion of the aircraft. SAR data and motion data are collected together and stored on-board or down-linked to ground station. As discussed, the motion data is interpolated and matched with the actual SAR data. The results are seen in Fig. 5.6 where data collected from a UAV shows that the motion corrections improve the focusing of an array of corner reflector targets. A more detailed description of the μSAR system is found in Appendix C. Another imagery example, from the more advanced MicroASAR, is seen in Fig. 5.7. A number of other small FMCW SAR's are described below.

The MISAR [42] developed by EADS was designed to fly on small UAV's having a weight of less than 4 kg and power consumpsion under 100 W. The system operates at Ka-band (35 GHz) and produces images with 0.5 m x 0.5 m resolution. SAR and motion data (from an on-board INS) are transmitted to the ground via a 5 MHz analog video link. The non-ideal motion is compensated using the INS data and autofocusing.

The Delft University of Technology has developed a demonstrator system [41] with a center frequency of 10 GHz and a variable bandwidth of 130-520 MHz. Algorithms have been developed which compensate for non-linearities in the chirp [62] and the continuous forward motion during the chirp [70]. An INS unit is used to measure the aircraft motion.

The MINISARA [47] from the Universidad Politécnica de Madrid is a portable SAR system with a center frequency of 34 GHz and a bandwidth of 2 GHz. The system is small

(24x16x9 cm), and lightweight (2.5 kg). The motion compensation relies upon autofocus algorithms.

The ImSAR NanoSAR(TM) [58] is a one-pound SAR specifically built for use on small UAV's.

The DRIVE from ONERA [59] has a central frequency of 35 GHz and a bandwidth of about 800 MHz. The goal is to develop a 3-D SAR imaging system, studies include compensating for the motion of the wings that carry the antennas.

The FGAN ARTINO [60] is a 3-D imaging radar similar to the ONERA project that operates at Ka-band. A custom INS was developed for the project and is used for motion compensation and UAV control.

5.6 Summary

In this chapter the effects of non-ideal motion on an LFM-CW SAR signal have been explored and corrective algorithms developed. The motion compensation has been successfully applied to simulated and real SAR data taking into account the motion during the pulse and correcting the motion-induced range shift without interpolation. The small size of LFM-CW SAR, like the BYU μSAR, makes it possible for it to operate from a small aircraft or UAV, which are especially susceptible to the effects of atmospheric turbulence. With motion measurements, the negative effects of non-ideal motion can be corrected, extending the utility of small LFM-CW SAR.
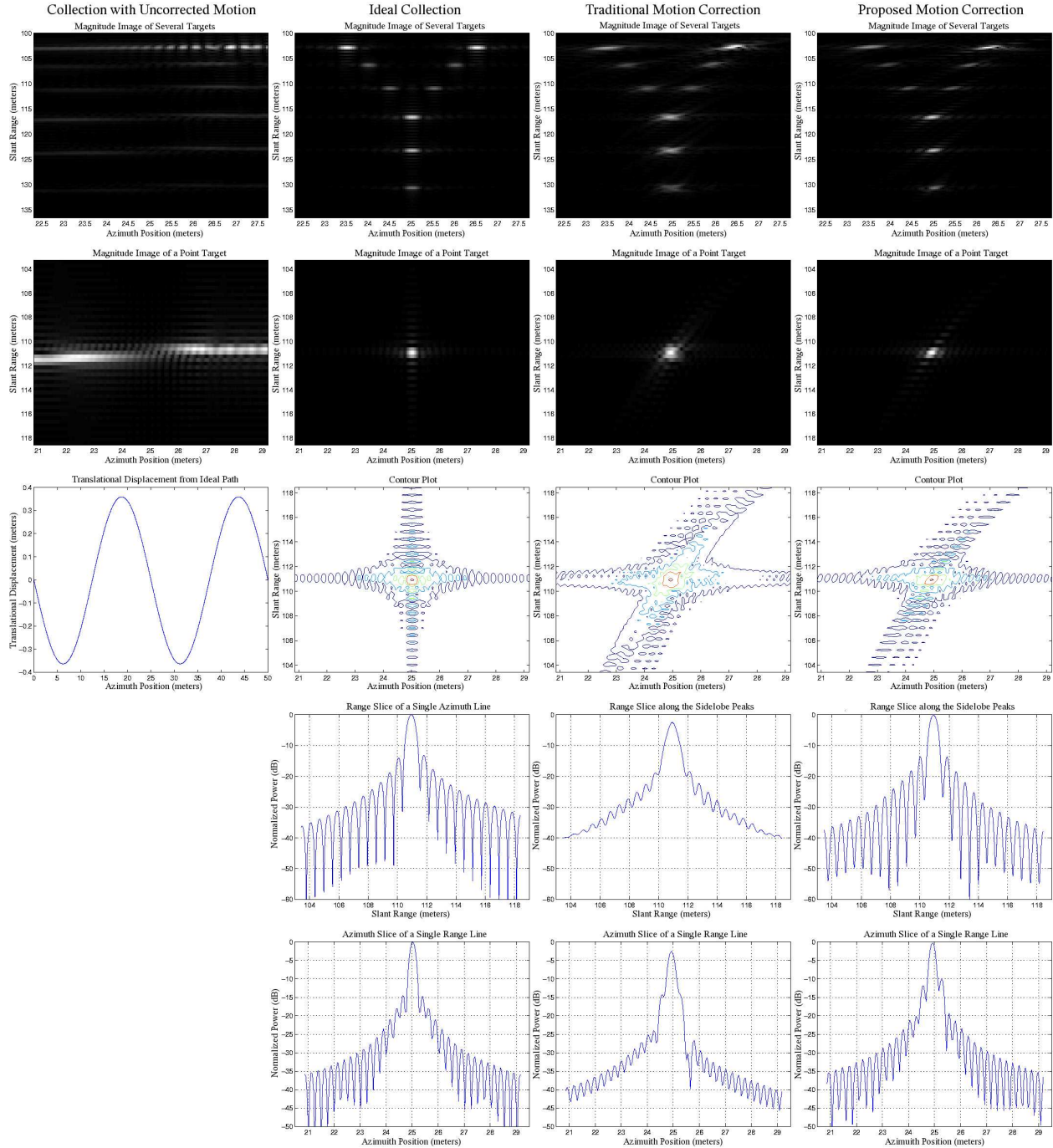
Figure 5.5: Simulated LFM-CW SAR data of an array of point targets and a single point target. The first column shows the motion errors, the second column shows an ideal collection without any motion errors. The third column shows motion correction using the traditional compensation and the fourth column shows the proposed motion compensation. The power is normalized to the peak of the ideal collection. In this example the non-ideal motion is sinusoidal. The principal component of the translational motion while the target is in the main beamwidth is moving toward the target, this results in the corrected targets appearing "squinted."
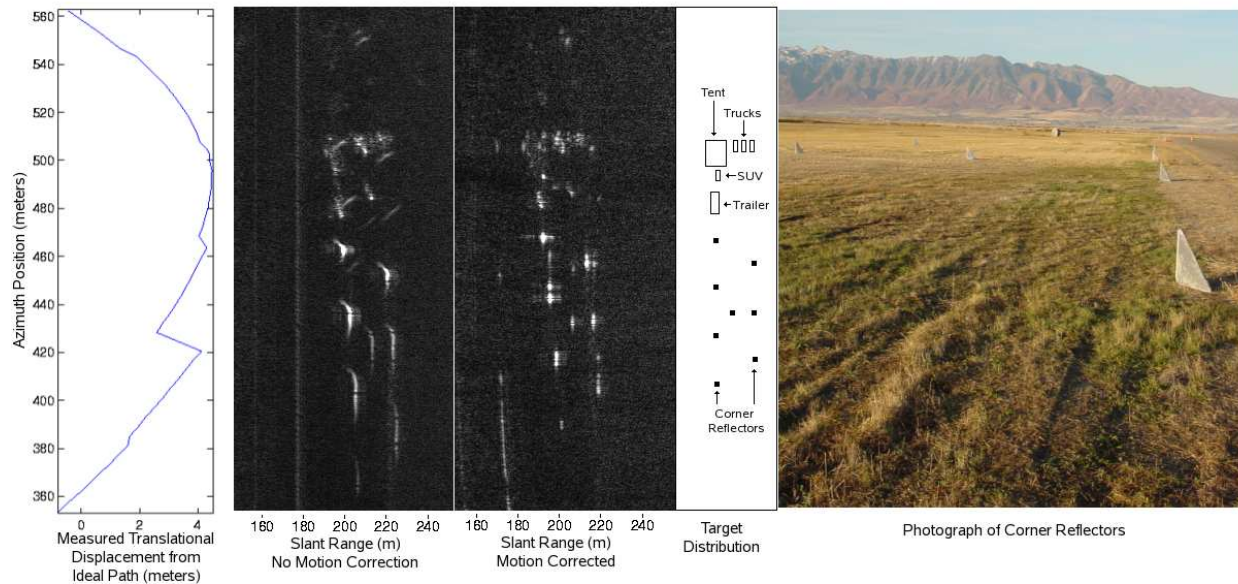
Figure 5.6: An area of the airport at Logan, Utah, imaged with a 160 MHz bandwidth C-band μSAR flown on a UAV and processed with the FSA, is shown with corner reflector targets arrayed in a field. From left to right the panels show: the translational motion errors calculated from the INS motion data, the processed image without motion compensation, the image after applying the proposed compensation scheme, the arrangement of targets in the image, and a photograph taken from near the trailer. The limitations of the INS motion sensor are noticeable in the inconsistency of the measured translational displacement, which results in defocusing of a few of the targets in the compensated image.
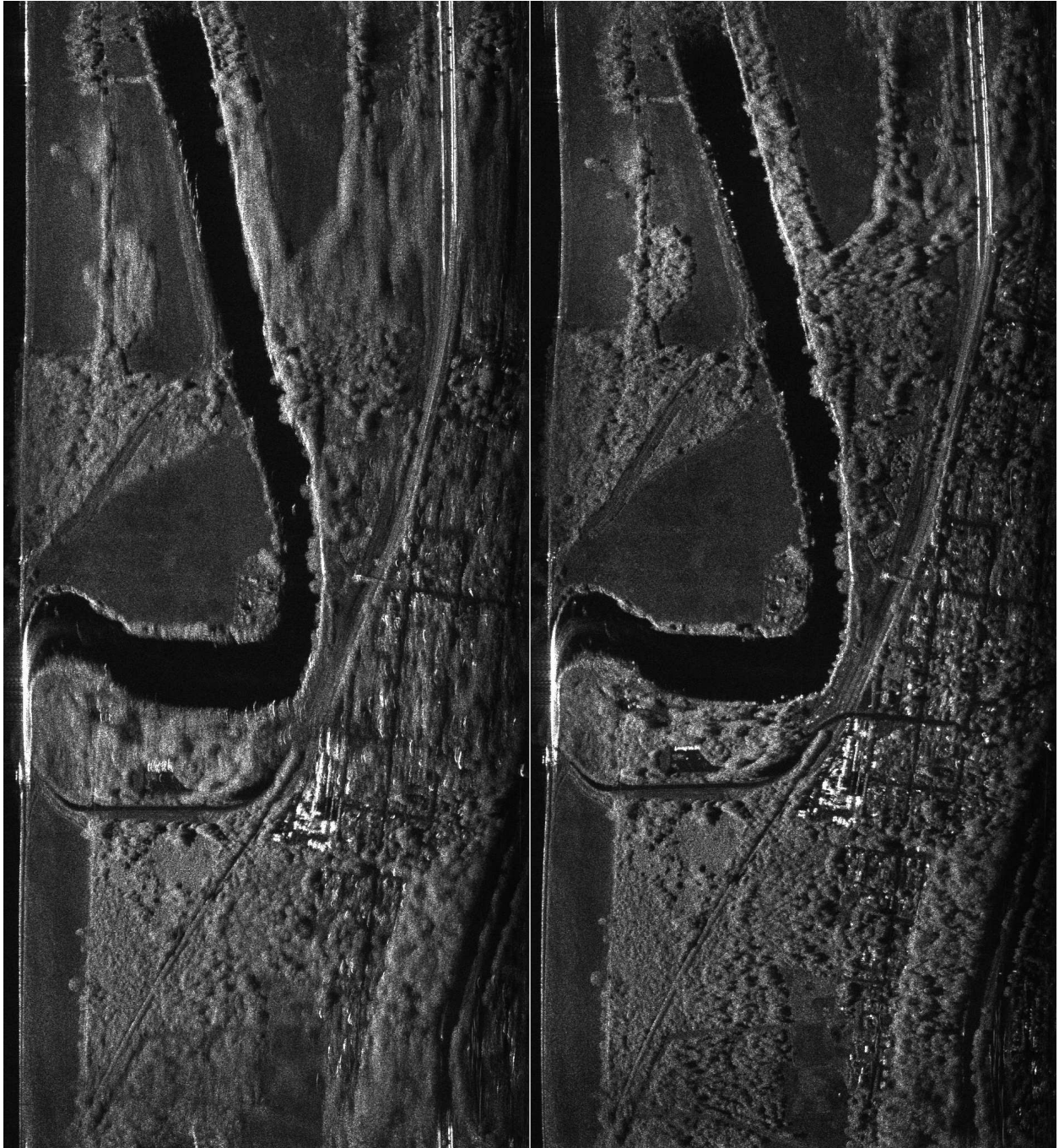
Figure 5.7: A MicroASAR image processed without motion compensation on the left and with motion compensation on the right. Both images are processed with the FSA, with the image at right showing the effects of using the motion compensation algorithm developed in this chapter. The blurring in the image at left is caused by the non-ideal motion of the platform. Because the motion data was precisely measured during the data collection, the image at right is well focused. The area imaged is the Snohomish River south-east of Everret, WA.

CHAPTER 6.   CONCLUSION

This dissertation contributes to the theory and technology of synthetic aperture radar image processing by presenting research which generalizes SAR processing methods to avoid the image degradation that can result from commonly used approximations of the SAR signal model. This is achieved through the development of a generalized chirp-scaling algorithm and a generalized frequency scaling algorithm which address the problems caused by approximations based on a Taylor series expansion of the SAR signal for both pulsed SAR and LFM-CW SAR. Also, for LFM-CW SAR, the traditional stop-and-go approximation for modeling the platform motion is invalid. To overcome this, I have developed image formation algorithms that account for the continuous platform motion and a compensation algorithm for correcting translational position errors due to the continuous non-ideal motion of real-world SAR platforms.

For SAR systems that push the center frequency lower, the bandwidth larger, and the beamwidth wider, the Taylor series approximation used in common frequency-domain SAR processing algorithms is inadequate. An expression for the phase error term due to the approximation has been developed. Visualizing this error over the two-dimensional frequency support band enhances analysis of the effects of varying the SAR parameters for a given approximation. Accounting for an arbitrary number of high-order terms by using a generalized algorithm, built upon the CSA framework for pulsed SAR (the GCSA) and the FSA framework for LFM-CW SAR (the GFSA), increases the precision over existing algorithms, providing an attractive alternative to the ωKA and time-domain methods for processing wide-beamwidth, low-frequency, large-bandwidth SAR data. A comparative summary of the various different processing algorithms discussed in this dissertation is presented in Table 6.1.

Table 6.1: **SAR Processing Algorithm Summary**

Algorithm	Approximate Processing Time for Typical NuSAR Image	Comments
RDA (without RCMC)	6 min	Robust processing, works with poor motion data (image quality may be poor). Motion compensation straightforward. Processing limited to narrow beamwidths, small squints. Poor performance with low-frequency SAR and large bandwidths.
CSA	10 min	Less robust processing, requires better motion data (image quality better). Motion compensation straightforward. Limited to narrow beamwidths, small squints. Poor performance with low-frequency SAR and large bandwidths.
GCSA (3rd Order)	22 min	Image formation is less robust and requires better motion data (resulting in improved image quality with increased order). Motion compensation is straightforward. Improved processing at wider beamwidths and larger squints. Improved performance with low-frequency SAR.
GCSA (4th Order)	36 min	
GCSA (5th Order)	54 min	
GCSA (6th Order)	72 min	
ω-K	60-120 min	Image formation not robust, requires good motion data (very good image quality). Motion compensation limited to reference range. Works well with wide beamwidth, squint, and/or low-frequency SAR, provided there is little non-ideal motion.
Back-projection	5 hours	Very general algorithm that requires precise motion data and elevation data for the imaged area (results in very high quality imagery). Works with non-linear flight paths and handles non-ideal motion, wide beamwidths, high squints, large bandwidths, and low-frequencies.

The information presented in Table 6.1 is representative of the results of running SAR processing software developed at BYU on a Linux workstation with two processors running at 2.4 GHz and 4 GB of RAM. The chart shows some general guidlines for understanding how the different algorithms are used and their limitations. In general, image quality increases with complexity, as shown from top to bottom in Table 6.1. The generalized algorithms developed in this dissertations fill the gap between the approximate, efficient algorithms and the precise but computationally demanding algorithms.

By generalizing the LFM-CW SAR signal model, I avoid the traditional stop-and-go approximation. Using this general model, I have developed a robust continuous motion correction for arbitrary flight paths with both precise and approximate LFM-CW SAR backprojection algorithms. Also, for frequency domain processing methods, I have developed a motion compensation that takes into account the motion during the chirp and corrects the motion-induced range shift without interpolation. These algorithms are especially important when a SAR is operated on a small aircraft or UAS, which are especially susceptible to the effects of atmospheric turbulence. With good motion measurements, the negative effects of non-ideal motion can be corrected, extending the utility of small LFM-CW SAR.

6.1 Contributions and Publications

The contributions of this dissertation include the following:

- I have shown that for SAR systems with lower center frequencies, larger bandwidths, and wider beamwidths, the approximations used in common frequency-domain SAR processing algorithms are inadequate. I have developed both an expression for the phase error due to the Taylor series expansion approximation of the SAR signal in the wavenumber domain and a visualization of the error over the two-dimensional frequency support band. I have analyzed the effects of varying the SAR parameters for a given approximation. I have developed a generalized algorithm with a set of guidelines used to determine the approximation order of the Taylor approximation required for proper image processing given a set of SAR parameters. This efficient frequency-domain

algorithm is built upon the CSA framework and shows that accounting for higher order terms increases the precision over previously existing algorithms.

- For LFM-CW SAR, I have contributed various processing methods and system design innovations as detailed in this dissertation. I developed an LFM-CW backprojection algorithm for both exactly and approximately compensating for the continuous platform motion. I derived the LFM-CW SAR signal in the dechirped Doppler domain and showed the effect of using a Taylor series expansion as an approximate model for the SAR signal. I also developed a generalized frequency scaling algorithm (GFSA) that uses an arbitrary number of terms of the the Taylor series approximation to process LFM-CW SAR data.

- The continuous platform motion must also be taken into account when correcting for the non-ideal translational motion of the platform for LFM-CW SAR. I developed the theory for expressing the effects of translational motion on the LFM-CW SAR signal, and developed compensation algorithms that exactly and approximately correct for the non-ideal platform motion.

- Using the tools developed for correcting the non-ideal motion of LFM-CW SAR, I have developed a motion compensation algorithm for pulsed SAR that avoids a computationally taxing interpolation for differential motion correction.

- I developed the theory and processing algorithm for coherently combining the returns from the separate frequency bands of a multi-frequency-band SAR system to improve the range resolution. The resolution improvement is achieved by combining the bandwiths to form a larger single bandwidth. This method can be used to increase the bandwidth given hardware constraints (each band can have its own RF hardware) and as an alternative to common notched-chirp approaches to keep-out bands.

The following is a list of my peer-reviewed journal papers:

1. E. Zaugg and D. Long, "Theory and Application of Motion Compensation for LFM-CW SAR," *IEEE Transactions on Geoscience and Remote Sensing*, vol. 46, no. 10, pp. 2990-2998, Oct. 2008. [6]

2. E. Zaugg and D. Long, "Generalized Frequency-Domain SAR Processing," *IEEE Transactions on Geoscience and Remote Sensing*, vol. 47, no. 11, pp. 3761-3773, Nov. 2009. [4]

3. E. Zaugg and D. Long, "Generalized LFM-CW SAR Processing," *IEEE Transactions on Geoscience and Remote Sensing*, (in review). [5]

The following is a list of my technical conference publications:

1. E. Zaugg, D. Hudson, and D. Long, "The BYU μSAR: A small, student-built SAR for UAV operation," in *Proceedings of the IEEE International Geoscience and Remote Sensing Symposium*, Denver, Colorado, 31 2006-Aug. 4 2006, pp. 411-414. [45]

2. E. Zaugg and D. Long, "Full motion compensation for LFM-CW synthetic aperture radar," in *Proceedings of the IEEE International Geoscience and Remote Sensing Symposium*, Barcelona, Spain, July 2007, pp. 5198-5201. [71]

3. E. Zaugg, D. Long, and M. Wilson, "Improved SAR motion compensation without interpolation," in *Proceedings of the 7th European Conference on Synthetic Aperture Radar*, Friedrichshafen, Germany, vol. 3, June 2008, pp. 347-350. [72]

4. E. Zaugg and D. Long, "Along-track resolution enhancement for wide-bandwidth, low-frequency SAR by accounting for the wavelength change over the bandwidth," in *Proceedings of the IEEE International Geoscience and Remote Sensing Symposium*, Boston, Massachusetts, vol. 4, July 2008, pp. IV -1272-IV -1275. [73]

5. M. C. Edwards, E. C. Zaugg, D. G. Long, R. Christiansen, and A. Margulis, "A small, manned aircraft as a testbed for radar sensor development," in *Proceedings of SPIE Defense, Security+Sensing*, Orlando, Florida, vol. 7308, no. 1., 2009, p. 730807. [Online]. Available: http://link.aip.org/link/?PSI/7308/730807/1 [54]

6. E. Zaugg, M. Edwards, and Y. Margulis, "The SlimSAR: A small, flexible, synthetic aperture radar for UAS operation (U)," in *Proceedings of the 55th Annual MSS Tri-Service Radar Symposium*, Boulder, Colorado, June 2009. [74]

7. E. Zaugg and D. Long, "Coherent multi-frequency-band resolution enhancement for synthetic aperture radar," in *Proceedings of the IEEE International Geoscience and Remote Sensing Symposium*, Cape Town, South Africa, July 2009. [75]

8. E. Zaugg, M. Edwards, and Y. Margulis, "New small, flexible, synthetic aperture radars for UAS operation (U)," in *Proceedings of the MSS National Symposium*, Las Vega, Nevada, August 2009. [76]

9. E. Zaugg, D. Long, M. Edwards, M. Fladeland, R. Kolyer, R. Crocker, J. Maslanik, and U. Herzfeld, "Environmental science combining data from a small SAR on an unmanned aircraft with satellite observations: The microASAR on the NASA SIERRA UAS for the characterization of Arctic sea ice experiment (CASIE)," in *Proceedings of CEOS SAR*, Pasadena, California, November 2009. [77]

6.2 Future Work

The work of this dissertation can be applied and extended to a variety of research topics. A few examples are enumerated below.

1. For the backprojection algorithm, errors in the motion measurement accuracy and in the SAR system parameters can cause image degradation. An exciting avenue of research is to perform a theoretic error analysis on the different error sources to model the effects of each type of error. Ultimately, an autofocus algorithm for backprojection could be developed to automatically detect and correct for different kinds of errors.

2. The multi-frequency-band resolution enhancement presented in Appendix B has been developed for pulsed SAR, but it can be extended to work with LFM-CW SAR. Also, the techniques still need to be demonstrated with a actual SAR system.

3. The ωKA has some deficiencies in performing high precision motion compensation over the entire swath. The motion compensation techniques developed for both LFM-CW SAR and pulsed SAR can be applied to the ωKA to improve the performace of the motion compensation.

REFERENCES

[1] W. G. Carrara, R. S. Goodman, and R. M. Majewski, *Spotlight Synthetic Aperture Radar: Signal Processing Algorithms.* Artech House, 1995. 2, 3, 4, 14, 18, 68, 69

[2] I. Cumming, Y. Neo, and F. Wong, "Interpretations of the Omega-K algorithm and comparisons with other algorithms," *Proceedings of the IEEE International Geoscience and Remote Sensing Symposium*, vol. 3, pp. 1455–1458, July 2003. 2, 3, 4

[3] M. Soumekh, *Synthetic Aperture Radar Signal Processing with MATLAB Algorithms.* John Wiley & Sons, Inc., 1999. 3

[4] E. Zaugg and D. Long, "Generalized frequency-domain SAR processing," *IEEE Transactions on Geoscience and Remote Sensing*, vol. 47, no. 11, pp. 3761–3773, Nov. 2009. 6, 111

[5] ——, "Generalized LFM-CW SAR processing," *IEEE Transactions on Geoscience and Remote Sensing*, In Review. 6, 111

[6] ——, "Theory and application of motion compensation for LFM-CW SAR," *IEEE Transactions on Geoscience and Remote Sensing*, vol. 46, no. 10, pp. 2990–2998, Oct. 2008. 7, 55, 57, 110

[7] G. Franceschetti and R. Lanari, *Synthetic Aperture Radar Processing.* CRC Press, 1999. 12, 122

[8] I. G. Cumming and F. H. Wong, *Digital Processing of Synthetic Aperture Radar Data.* Artech House, 2005. 22, 24, 29, 30, 33, 48, 93, 124

[9] S. Redadaa, J.-M. Le Caillec, B. Solaiman, and M. Benslama, "Focusing problems of subsurface imaging by a low-frequency SAR," in *Proceedings of the IEEE International Geoscience and Remote Sensing Symposium*, July 2007, pp. 4101–4104. 27

[10] L. Ulander, M. Blom, B. Flood, P. Follo, P.-O. Frolind, A. Gustavsson, T. Jonsson, B. Larsson, D. Murdin, M. Pettersson, U. Raaf, and G. Stenstrom, "Development of the ultra-wideband LORA SAR operating in the VHF/UHF-band," in *Proceedings of the IEEE International Geoscience and Remote Sensing Symposium*, vol. 7, July 2003, pp. 4268–4270. 27

[11] M. Ressler, "The army research laboratory ultra wideband boomSAR," in *Proceedings of the IEEE International Geoscience and Remote Sensing Symposium*, vol. 3, May 1996, pp. 1886–1888. 27

[12] H. Hellsten, "CARABAS-an UWB low frequency SAR," in *IEEE MTT-S International Microwave Symposium Digest*, vol. 3, Jun 1992, pp. 1495–1498. 27

[13] H. Nguyen, H. Roussel, and W. Tabbara, "A coherent model of forest scattering and SAR imaging in the VHF and UHF-band," *IEEE Transactions on Geoscience and Remote Sensing*, vol. 44, no. 4, pp. 838–848, April 2006.   27

[14] G. Smith-Jonforsen, L. Ulander, and X. Luo, "Low VHF-band backscatter from coniferous forests on sloping terrain," *IEEE Transactions on Geoscience and Remote Sensing*, vol. 43, no. 10, pp. 2246–2260, Oct. 2005.   27

[15] A. Manninen and L. Ulander, "Forestry parameter retrieval from texture in CARABAS VHF-band SAR images," *IEEE Transactions on Geoscience and Remote Sensing*, vol. 39, no. 12, pp. 2622–2633, Dec 2001.   27

[16] L. Ulander and P.-O. Frolind, "Ultra-wideband SAR interferometry," *IEEE Transactions on Geoscience and Remote Sensing*, vol. 36, no. 5, pp. 1540–1550, Sep 1998.   27

[17] H. Israelsson, L. Ulander, J. Askne, J. Fransson, P.-O. Frolind, A. Gustavsson, and H. Hellsten, "Retrieval of forest stem volume using VHF SAR," *IEEE Transactions on Geoscience and Remote Sensing*, vol. 35, no. 1, pp. 36–40, Jan 1997.   27

[18] L. Ulander and P. Frolund, "Ultra-wideband and low-frequency SAR interferometry," in *Proceedings of the IEEE International Geoscience and Remote Sensing Symposium*, vol. 1, May 1996, pp. 668–670 vol.1.   27

[19] J. Swiger, "Resolution limits of ultra wideband synthetic aperture radar using a rectangular aperture for FFT processing," *IEEE Transactions on Aerospace and Electronic Systems*, vol. 30, no. 3, pp. 935–938, Jul 1994.   27

[20] R. Goodman, S. Tummala, and W. Carrara, "Issues in ultra-wideband, widebeam SAR image formation," in *Record of the IEEE International Radar Conference*, May 1995, pp. 479–485.   27

[21] A. Moreira and Y. Huang, "Airborne SAR processing of highly squinted data using a chirp scaling approach with integrated motion compensation," *IEEE Transactions on Geoscience and Remote Sensing*, vol. 32, no. 5, pp. 1029–1040, Sep 1994.   27, 33, 95, 121

[22] G. Davidson, I. Cumming, and M. Ito, "A chirp scaling approach for processing squint mode SAR data," *IEEE Transactions on Aerospace and Electronic Systems*, vol. 32, no. 1, pp. 121–133, Jan. 1996.   27, 33, 39, 48, 51

[23] A. Moreira, J. Mittermayer, and R. Scheiber, "Extended chirp scaling algorithm for air- and spaceborne SAR data processing in stripmap and scanSAR imaging modes," *IEEE Transactions on Geoscience and Remote Sensing*, vol. 34, no. 5, pp. 1123–1136, Sep 1996.   27, 33, 51

[24] K. Wang and X. Liu, "Quartic-phase algorithm for highly squinted SAR data processing," *IEEE Geoscience and Remote Sensing Letters*, vol. 4, no. 2, pp. 246–250, April 2007.   27, 33, 48, 51

[25] R. Rau and J. McClellan, "Analytic models and postprocessing techniques for UWB SAR," *IEEE Transactions on Aerospace and Electronic Systems*, vol. 36, no. 4, pp. 1058–1074, Oct 2000.   27

[26] A. Potsis, A. Reigber, J. Mittermayer, A. Moreira, and N. Uzunoglou, "Improving the focusing properties of SAR processors for wide-band and wide-beam low frequency imaging," in *Proceedings of the IEEE International Geoscience and Remote Sensing Symposium*, vol. 7, 2001, pp. 3047–3049.   27, 28

[27] G. Fornaro, G. Franceschetti, and S. Perna, "On center-beam approximation in SAR motion compensation," *IEEE Geoscience and Remote Sensing Letters*, vol. 3, no. 2, pp. 276–280, April 2006.   27, 99

[28] A. Potsis, A. Reigber, E. Alivizatos, A. Moreira, and N. K. Uzunoglou, "Comparison of chirp scaling and wavenumber domain algorithms for airborne low-frequency SAR," F. Posa, Ed., vol. 4883, no. 1.   SPIE, 2003, pp. 11–19. [Online]. Available: http://link.aip.org/link/?PSI/4883/11/1   27

[29] H. Hellsten and L. E. Andersson, "An inverse method for the processing of synthetic aperture radar data," *Inverse Problems*, vol. 3, no. 1, pp. 111–124, 1987. [Online]. Available: http://stacks.iop.org/0266-5611/3/111   27

[30] A. Reigber, E. Alivizatos, A. Potsis, and A. Moreira, "Extended wavenumber-domain synthetic aperture radar focusing with integrated motion compensation," *Proceedings of IEE Radar, Sonar and Navigation*, vol. 153, no. 3, pp. 301–310, June 2006.   27, 28, 32

[31] M. Cobb and J. McClellan, "Omega-k quadtree UWB SAR focusing," in *Proceedings of the IEEE Radar Conference*, 2001, pp. 311–314.   27

[32] H. Choi and J. Munson, D.C., "On the optimality and exactness of wavenumber-domain SAR data processing," in *Proceedings of the IEEE International Conference Image Processing*, vol. 1, Nov 1994, pp. 456–460.   27

[33] T. Sjogren, V. Vu, and M. Pettersson, "A comparative study of the polar version with the subimage version of fast factorized backprojection in UWB SAR," in *Proceedings of the International Radar Symposium*, May 2008, pp. 1–4.   27

[34] L. Ulander, H. Hellsten, and G. Stenstrom, "Synthetic-aperture radar processing using fast factorized back-projection," *IEEE Transactions on Aerospace and Electronic Systems*, vol. 39, no. 3, pp. 760–776, July 2003.   27, 28

[35] A. Yegulalp, "Fast backprojection algorithm for synthetic aperture radar," in *The Record of the IEEE Radar Conference*, 1999, pp. 60–65.   27, 28

[36] M. Blom and P. Follo, "VHF SAR image formation implemented on a GPU," in *Proceedings of the IEEE International Geoscience and Remote Sensing Symposium*, vol. 5, July 2005, pp. 3352–3356.   28

[37] S. Madsen, "Motion compensation for ultra wide band SAR," in *Proceedings of the IEEE International Geoscience and Remote Sensing Symposium*, vol. 3, 2001, pp. 1436–1438. 28, 121

[38] A. Reigber, A. Potsis, E. Alivizatos, N. Uzunoglu, and A. Moreira, "Wavenumber domain SAR focusing with integrated motion compensation," in *Proceedings of the IEEE International Geoscience and Remote Sensing Symposium*, vol. 3, July 2003, pp. 1465–1467. 28, 32

[39] R. Raney, H. Runge, R. Bamler, I. Cumming, and F. Wong, "Precision SAR processing using chirp scaling," *IEEE Transactions on Geoscience and Remote Sensing*, vol. 32, no. 4, pp. 786–799, Jul 1994. 33

[40] L. Jin and X. Liu, "Nonlinear frequency scaling algorithm for high squint spotlight SAR data processing," *EURASIP J. Adv. Signal Process*, vol. 2008, pp. 1–8, 2008. 48, 75

[41] A. Meta, J. de Wit, and P. Hoogeboom, "Development of a high resolution airborne millimeter wave FM-CW SAR," in *Proceedings of the First European Radar Conference*, 2004, pp. 209–212. 55, 56, 89, 102

[42] M. Edrich, "Design overview and flight test results of the miniaturised SAR sensor MISAR," in *Proceedings of the First European Radar Conference*, 2004, pp. 205–208. 55, 56, 89, 102

[43] ——, "Ultra-lightweight synthetic aperture radar based on a 35 GHz FMCW sensor concept and online raw data transmission," *Proceedings of IEE Radar, Sonar and Navigation*, vol. 153, no. 2, pp. 129–134, April 2006. 55

[44] A. Meta, P. Hakkaart, F. Zwan, P. Hoogeboom, and L. Ligthart, "First demonstration of an X-band airborne FMCW SAR," in *Proceedings of the 6th European Conference on Synthetic Aperture Radar*, 2006. 55

[45] E. Zaugg, D. Hudson, and D. Long, "The BYU uSAR: A small, student-built SAR for UAV operation," in *Proceedings of the IEEE International Geoscience and Remote Sensing Symposium*, July 31-Aug. 4 2006, pp. 411–414. 55, 56, 60, 89, 102, 111, 121, 143

[46] J. Nouvel, S. Roques, and O. du Plessis, "A low-cost imaging radar: DRIVE on board ONERA motorglider," in *Proceedings of the IEEE International Geoscience and Remote Sensing Symposium*, July 2007, pp. 5306–5309. 55

[47] P. Almorox-Gonzalez, J.-T. Gonzalez-Partida, M. Burgos-Garcia, C. d. l. Morena-Alvarez-Palencia, L. Arche-Andradas, and B. P. Dorta-Naranjo, "Portable high resolution LFM-CW radar sensor in millimeter-wave band," in *SENSORCOMM '07: Proceedings of the 2007 International Conference on Sensor Technologies and Applications*. Washington, DC, USA: IEEE Computer Society, 2007, pp. 5–9. 55, 89, 102

[48] J.-T. Gonzalez-Partida, P. Almorox-Gonzalez, M. Burgos-Garcia, and B.-P. Dorta-Naranjo, "SAR system for UAV operation with motion error compensation beyond

the resolution cell," *Sensors*, vol. 8, no. 5, pp. 3384–3405, 2008. [Online]. Available: http://www.mdpi.com/1424-8220/8/5/3384   55

[49] M. Edwards, D. Madsen, C. Stringham, A. Margulis, B. Wicks, and D. Long, "microASAR: A small, robust LFM-CW SAR for operation on UAVs and small aircraft," in *Proceedings of the IEEE International Geoscience and Remote Sensing Symposium*, vol. 5, July 2008, pp. V –514–V –517.   55, 56, 60, 133, 143, 145, 146

[50] A. Meta, P. Hoogeboom, and L. Ligthart, "Non-linear frequency scaling algorithm for FMCW SAR data," in *Proceedings of the European Radar Conference*, Sept. 2006, pp. 9–12.   55, 75, 89, 93

[51] ——, "Signal processing for FMCW SAR," *IEEE Transactions on Geoscience and Remote Sensing*, vol. 45, no. 11, pp. 3519–3532, Nov. 2007.   55, 89

[52] Z.-H. Jiang and K. Huang-Fu, "Squint LFMCW SAR data processing using doppler-centroid-dependent frequency scaling algorithm," *IEEE Transactions on Geoscience and Remote Sensing*, vol. 46, no. 11, pp. 3535–3543, Nov. 2008.   55, 75

[53] W.-Q. Wang, Q. Peng, and J. Cai, "Waveform-diversity-based millimeter-wave UAV SAR remote sensing," *IEEE Transactions on Geoscience and Remote Sensing*, vol. 47, no. 3, pp. 691–700, March 2009.   55

[54] M. C. Edwards, E. C. Zaugg, D. G. Long, R. Christiansen, and A. Margulis, "A small, manned aircraft as a testbed for radar sensor development," K. I. Ranney and A. W. Doerry, Eds., vol. 7308, no. 1.   SPIE, 2009, p. 730807. [Online]. Available: http://link.aip.org/link/?PSI/7308/730807/1   57, 60, 61, 111, 149, 150

[55] O. Frey, C. Magnard, M. Ruegg, and E. Meier, "Focusing of airborne synthetic aperture radar data from highly nonlinear flight tracks," *IEEE Transactions on Geoscience and Remote Sensing*, vol. 47, no. 6, pp. 1844–1858, June 2009.   57

[56] "CUDA Zone – the resource for CUDA developers," 2009. [Online]. Available: http://www.nvidia.com/object/cuda_home.html#state=detailsOpen;aid=057f342d-84b4-4a12-ae35-5208c51ed958   65

[57] J. Mittermayer, A. Moreira, and O. Loffeld, "Spotlight SAR data processing using the frequency scaling algorithm," *IEEE Transactions on Geoscience and Remote Sensing*, vol. 37, no. 5, pp. 2198–2214, Sep 1999.   68, 69, 75, 93, 94

[58] L. Harris, "ImSAR and Insitu introduce the one-pound nanoSAR(tm), miniature synthetic aperture radar," 2006. [Online]. Available: http://www.imsar.net   89, 103

[59] J. Nouvel, H. Jeuland, G. Bonin, S. Roques, O. Du Plessis, and J. Peyret, "A Ka band imaging radar: DRIVE on board ONERA motorglider," in *Proceedings of the IEEE International Geoscience and Remote Sensing Symposium*, July 31-Aug. 4 2006, pp. 134–136.   89, 103

[60] M. Weib and J. Ender, "A 3d imaging radar for small unmanned airplanes - ARTINO," in *Proceedings of the European Radar Conference*, Oct. 2005, pp. 209–212.   89, 103

[61] J. de Wit, A. Meta, and P. Hoogeboom, "Modified range-doppler processing for FM-CW synthetic aperture radar," *IEEE Geoscience and Remote Sensing Letters*, vol. 3, no. 1, pp. 83–87, Jan. 2006.   89, 92

[62] A. Meta, P. Hoogeboom, and L. Ligthart, "Range non-linearities correction in FMCW SAR," in *Proceedings of the IEEE International Geoscience and Remote Sensing Symposium*, July 31-Aug. 4 2006, pp. 403–406.   89, 102

[63] Z.-H. Jiang, K. Huang-Fu, and J.-W. Wan, "A chirp transform algorithm for processing squint mode FMCW SAR data," *IEEE Geoscience and Remote Sensing Letters*, vol. 4, no. 3, pp. 377–381, July 2007.   89

[64] J. Kirk, "Motion compensation for synthetic aperture radar," *IEEE Transactions on Aerospace and Electronic Systems*, vol. AES-11, no. 3, pp. 338–348, May 1975.   89

[65] D. Stevens, I. Cumming, and A. Gray, "Options for airborne interferometric SAR motion compensation," *IEEE Transactions on Geoscience and Remote Sensing*, vol. 33, no. 2, pp. 409–420, Mar 1995.   89

[66] K. de Macedo and R. Scheiber, "Precise topography- and aperture-dependent motion compensation for airborne SAR," *IEEE Geoscience and Remote Sensing Letters*, vol. 2, no. 2, pp. 172–176, April 2005.   97

[67] P. Prats, A. Reigber, and J. Mallorqui, "Topography-dependent motion compensation for repeat-pass interferometric SAR systems," *IEEE Geoscience and Remote Sensing Letters*, vol. 2, no. 2, pp. 206–210, April 2005.   97

[68] G. Fornaro, "Trajectory deviations in airborne SAR: analysis and compensation," *IEEE Transactions on Aerospace and Electronic Systems*, vol. 35, no. 3, pp. 997–1009, Jul 1999.   99

[69] P. Prats, K. Camara de Macedo, A. Reigber, R. Scheiber, and J. Mallorqui, "Comparison of topography- and aperture-dependent motion compensation algorithms for airborne SAR," *IEEE Geoscience and Remote Sensing Letters*, vol. 4, no. 3, pp. 349–353, July 2007.   99

[70] A. Meta, P. Hoogeboom, and L. Ligthart, "Correction of the effects induced by the continuous motion in airborne FMCW SAR," in *Proceedings of the IEEE Conference on Radar*, April 2006, pp. 358–365.   102

[71] E. Zaugg and D. Long, "Full motion compensation for LFM-CW synthetic aperture radar," in *Proceedings of the IEEE International Geoscience and Remote Sensing Symposium*, July 2007, pp. 5198–5201.   111, 121

[72] E. Zaugg, D. Long, and M. Wilson, "Improved SAR motion compensation without interpolation," in *Proceedings of the 7th European Conference on Synthetic Aperture Radar*, vol. 3, June 2008, pp. 347–350.   111, 143

[73] E. Zaugg and D. Long, "Along-track resolution enhancement forwide-bandwidth, low-frequency SAR by accounting for the wavelength change over the bandwidth," in *Proceedings of the IEEE International Geoscience and Remote Sensing Symposium*, vol. 4, July 2008, pp. 1272–1275.   111

[74] E. Zaugg, M. Edwards, and Y. Margulis, "The slimSAR: A small, flexible, synthetic aperture radar for UAS operation (U)," in *Proceedings of the 55th Annual MSS Tri-Service Radar Symposium*, June 2009.   111, 134

[75] E. Zaugg and D. Long, "Coherent multi-frequency-band resolution enhancement for synthetic aperture radar," in *Proceedings of the IEEE International Geoscience and Remote Sensing Symposium*, July 2009.   112

[76] E. Zaugg, M. Edwards, and Y. Margulis, "New small, flexible, synthetic aperture radars for UAS operation (U)," in *Proceedings of the MSS National Symposium*, August 2009.   112

[77] E. Zaugg, D. Long, M. Edwards, M. Fladeland, R. Kolyer, R. Crocker, J. Maslanik, and U. Herzfeld, "Environmental science combining data from a small SAR on an unmanned aircraft with satellite observations: The microASAR on the NASA SIERRA UAS for the characterization of arctic sea ice experiment (CASIE)," in *Proceedings of CEOS SAR*, November 2009.   112

[78] P. Rosen, S. Hensley, K. Wheeler, G. Sadowy, T. Miller, S. Shaffer, R. Muellerschoen, C. Jones, H. Zebker, and S. Madsen, "UAVSAR: a new NASA airborne SAR system for science and technology research," in *Proceedings of the IEEE Conference on Radar*, April 2006, pp. 22–29.   121

[79] A. Meta, J. Lorga, J. de Wit, and P. Hoogeboom, "Motion compensation for a high resolution Ka-band airborne FM-CW SAR," in *Proceedings of the European Radar Conference*, Oct. 2005, pp. 391–394.   121

[80] J. Salzman, D. Akamine, and R. Lefevre, "Optimal waveforms and processing for sparse frequency UWB operation," in *Proceedings of the IEEE Radar Conference*, 2001, pp. 105–110.   129

[81] R. Lord and M. Inggs, "High resolution SAR processing using stepped-frequencies," in *Proceedings of the IEEE International Geoscience and Remote Sensing Symposium*, vol. 1, Aug 1997, pp. 490–492.   130

[82] ——, "High range resolution radar using narrowband linear chirps offset in frequency," in *Proceedings of the South African Symposium on Communications and Signal Processing*, Sep 1997, pp. 9–12.   130

[83] A. Wilkinson, R. Lord, and M. Inggs, "Stepped-frequency processing by reconstruction of target reflectivity spectrum," in *Proceedings of the South African Symposium on Communications and Signal Processing*, Sep 1998, pp. 101–104.   130

[84] F. Ulaby, R. Moore, and A. Fung, *Microwave Remote Sensing Active and Passive, vol. 1.*   Artech House, 1981.   139

[85] M. I. Duersch, "BYU micro-SAR: A very small, low-power LFM-CW synthetic aperture radar," Master's thesis, Brigham Young University, 2004. 141

[86] M. C. Edwards, "Design of a continuous-wave synthetic aperture radar system with analog dechirp," Master's thesis, Brigham Young University, 2009. 143, 145, 150

[87] M. M. Fladeland, R. Berthold, L. Monforton, R. Kolyer, B. Lobitz, and M. Sumich, "The NASA SIERRA UAV: A new unmanned aircraft for Earth science investigations," *AGU Fall Meeting Abstracts*, p. A365, Dec. 2008. 146

APPENDIX A.   IMPROVED PULSED SAR MOTION COMPENSATION WITHOUT INTERPOLATION

Motion compensation for airborne synthetic aperture radar (SAR) has always been important for high precision image formation. With high resolution SAR systems now operating on small aircraft and Unmanned Aircraft Systems (UAS's) [45, 78], which are more susceptible to atmospheric turbulence, motion compensation is receiving renewed attention [37, 71, 79].

This appendix develops a new motion compensation scheme for pulsed SAR systems. Conventional methods treat motion compensation as a phase correction problem, applying a bulk phase correction to the raw data to correct for a reference range followed by a differential phase correction applied after range compression to account for the range dependence of the motion correction.

This method fails to account for the source of the phase errors, the range shift due to the motion. This is a significant problem when the magnitude of the translational motion is greater than a range bin [21]. Interpolation is sometimes used to address this issue; however, it adds an additional computational burden. This is not acceptable for a high resolution SAR system designed to operate from a UAS and process the data in real-time.

The Naval Research Laboratory UAS SAR (NuSAR) is such a system. The NuSAR was developed as part of the U.S. Naval Research Laboratory's (NRL) DUSTER program in a team effort with Brigham Young University (BYU), ARTEMIS Inc., Space Dynamics Laboratory (SDL), and NRL. The NuSAR is one component of an integrated Longwave Infrared (LWIR), Visible Near-Infrared (VNIR), and SAR Imaging System.

The new motion compensation method presented in this appendix uses chirp scaling principles to correct the range shift and phase variations caused by translational motion. Section A.1 presents the errors caused by translation motion and the traditional two-step motion compensation algorithm. The new compensation algorithm is developed in Section

A.2. Section A.3 presents simulation results comparing the proposed algorithm to the traditional method and also presents NuSAR data which is used to verify the new method.

A.1   Translational Motion Errors

Basic SAR processing assumes that the platform moves in a straight line. In any actual data collection this is not the case, as the platform experiences a variety of deviations from the ideal path. These deviations introduce errors in the collected data which degrade the SAR image.

Translational motion causes platform displacement from the nominal, ideal path. This results in the target scene changing in range during data collection. This range shift also causes inconsistencies in the target phase history [7]. A target at range R is measured at range $R + \Delta R$ which introduces a phase shift of

$$\phi_{\mathrm{m}} = \frac{-2\Delta R \cdot 2\pi}{\lambda} \tag{A.1}$$

in the data. Fortunately, if the motion in known (usually from an on-board INS/GPS sensor), then the motion errors can be corrected. An example of a SAR image showing the degrading effects of non-ideal motion is found in Fig. A.1, which also shows the results of applying motion compensation.

The common method for compensating for the non-ideal motion involves two steps. First, the corrections are calculated for a reference range, R_{ref}, usually in the center of the swath. The phase correction

$$H_{\mathrm{mc1}} = \exp\left(j\frac{4\pi\Delta R_{\mathrm{ref}}}{\lambda}\right) \tag{A.2}$$

is applied to the raw data.

The SAR data is range compressed. A second order correction is applied to each range according to the differential correction from the reference range. For each R, ΔR is

Figure A.1: Images created from NuSAR data. The top image shows the target scene without any motion compensation. The bottom image is after motion compensation has been applied. The improved focusing is apparent.

calculated and the correction is formed,

$$H_{\text{mc2}} = \exp\left(j\frac{4\pi\left(\Delta R - \Delta R_{\text{ref}}\right)}{\lambda}\right). \tag{A.3}$$

At this point the motion-induced range shift can be removed through a computationally taxing interpolation. This method is commonly used in range-Doppler (RDA) processing and chirp-scaling (CSA) for SAR image generation.

A.2 New Motion Compensation

To formulate a new motion compensation scheme we start with the exponential terms of the demodulated SAR signal, as defined in [8],

$$s_0(\tau, \eta) = e^{(-j4\pi f_0 R(\eta)/c)} \cdot e^{\left(j\pi K_r (\tau - 2R(\eta)/c)^2\right)} \tag{A.4}$$

where τ is fast (range) time, η is slow (along-track) time, f_0 is the center frequency, $R(\eta)$ is the range to target, c is the speed of light, and K_r is the chirp rate.

With translational motion, the range $R(\eta)$ becomes $R(\eta) + \Delta R(\eta)$. We split the motion term into range-dependent, $\Delta R_{\text{diff}}(\eta)$, and range-independent, $\Delta R_{\text{ref}}(\eta)$, terms,

$$\Delta R(\eta) = \Delta R_{\text{ref}}(\eta) + \Delta R_{\text{diff}}(\eta), \tag{A.5}$$

which changes the demodulated signal, Eq. (A.4), to

$$
\begin{aligned}
s_m(\tau, \eta) = \quad & e^{-j\left[4\pi f_0 \frac{R(\eta) + \Delta R_{\text{ref}}(\eta) + \Delta R_{\text{diff}}(\eta)}{c}\right]} \\
& \cdot e^{j\pi K_r \left[\tau - 2\frac{R(\eta) + \Delta R_{\text{ref}}(\eta) + \Delta R_{\text{diff}}(\eta)}{c}\right]^2},
\end{aligned} \tag{A.6}
$$

which expands into

$$
\begin{aligned}
s_m(\tau, \eta) = \quad & e^{(-j4\pi f_0 R(\eta)/c)} \cdot e^{\left(j\pi K_r (\tau - 2R(\eta)/c)^2\right)} \\
& \cdot e^{j\, 4\pi K_r \frac{\Delta R_{\text{ref}}(\eta)^2}{c^2}} \cdot e^{-j\left[4\pi f_0 \frac{\Delta R_{\text{ref}}(\eta)}{c}\right]} \\
& \cdot e^{(-j4\pi K_r \tau \Delta R_{\text{ref}}(\eta)/c)} \\
& \cdot e^{\left(j8\pi K_r \Delta R_{\text{ref}}(\eta)(\Delta R_{\text{diff}}(\eta) + R(\eta))/c^2\right)} \\
& \cdot e^{j\, \frac{4\pi K_r \Delta R_{\text{diff}}(\eta)^2}{c^2}} \cdot e^{j\left[\frac{8\pi K_r R(\eta) \Delta R_{\text{diff}}(\eta)}{c^2}\right]} \\
& \cdot e^{-j\left[4\pi f_0 \frac{\Delta R_{\text{diff}}(\eta)}{c}\right]} \cdot e^{-j\left[4\pi K_r \tau \frac{\Delta R_{\text{diff}}(\eta)}{c}\right]},
\end{aligned} \tag{A.7}
$$

where the first two terms are the desired signal, Eq. (A.4), the next three terms are the range-independent errors, and the last five terms are the range-dependent errors.

124

The proposed method also follows a two step scheme but eliminates the need for interpolation. The first correction is applied to the raw data.

$$M_1(\tau, \eta) = e^{\frac{-j4\pi\Delta R_{\text{ref}}(\eta)(-f_0 c - K_r \tau c + K_r \Delta R_{\text{ref}}(\eta))}{c^2}}. \tag{A.8}$$

It cancels the range-independent errors and shifts the targets in range.

The data is then range compressed with a common algorithm (RDA or CSA). We simplify the next step by assuming that the range-dependent errors do not change during range compression. This introduces additional phase errors that we ignore, with future efforts planned to track the phase errors through the processing steps. The second motion correction is applied to the range compressed data, cancelling the range-dependent error terms,

$$
\begin{aligned}
M_2(R, \eta) = \quad & e^{\left(-j8\pi K_r \Delta R_{\text{ref}}(\eta)(\Delta R_{\text{diff}}(\eta) + R(\eta))/c^2\right)} \\
& \cdot e^{-j \frac{4\pi K_r \Delta R_{\text{diff}}(\eta)^2}{c^2} - \frac{8\pi K_r R(\eta)\Delta R_{\text{diff}}(\eta)}{c^2}} \\
& \cdot e^{j\left[4\pi f_0 \frac{\Delta R_{\text{diff}}(\eta)}{c}\right]} \cdot e^{j\left[4\pi K_r \tau \frac{\Delta R_{\text{diff}}(\eta)}{c}\right]}
\end{aligned}
\tag{A.9}
$$

where $\tau = 2R/c$.

A.3   Results

SAR data, simulated with parameters matching the X-Band NuSAR (described in Appendix C), is used to verify the proposed motion compensation algorithm. In Fig. A.2 a single point target is shown to have better range and azimuth resolution after applying the proposed motion compensation algorithm. Fig. A.3 shows an array of point targets with the same motion as in Fig. A.2. The results of the proposed motion compensation algorithm are dramatically better for translational motion of larger magnitude, as is demonstrated in Fig. A.4. Fig. A.5 shows an area imaged with the NuSAR and processed with the CSA. The application of the standard and proposed motion compensation algorithms is shown. The image quality is enhanced by using the motion compensation algorithms. The improvements
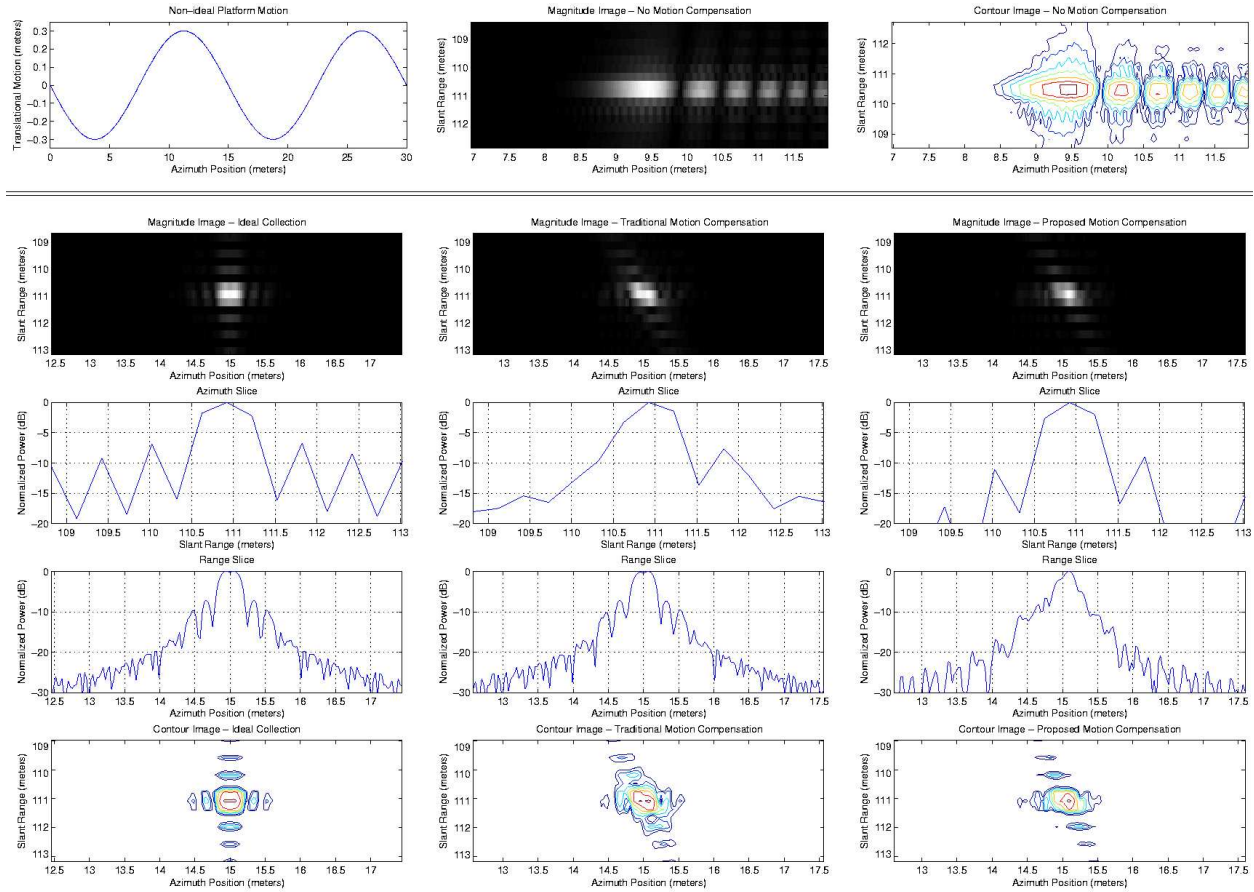
Figure A.2: Simulated SAR data of a single point target imaged with sinusoidal translational motion. The first column shows an ideal collection without non-ideal motion, the top row shows the translational motion and the image without compensation, the middle column shows the results of traditional motion compensation, and the rightmost column shows the proposed motion compensation.

are most noticeable in the increased sharpness of the fine details. The processing time is virtually identical for the two motion compensation methods.

A.4   Summary

An improved motion compensation algorithm for pulsed SAR has been proposed and tested. The results show that it properly corrects the effects of non-ideal motion while offering some advantages. The proposed method can be implemented in place of the traditional method to improve processing efficiency and accuracy.
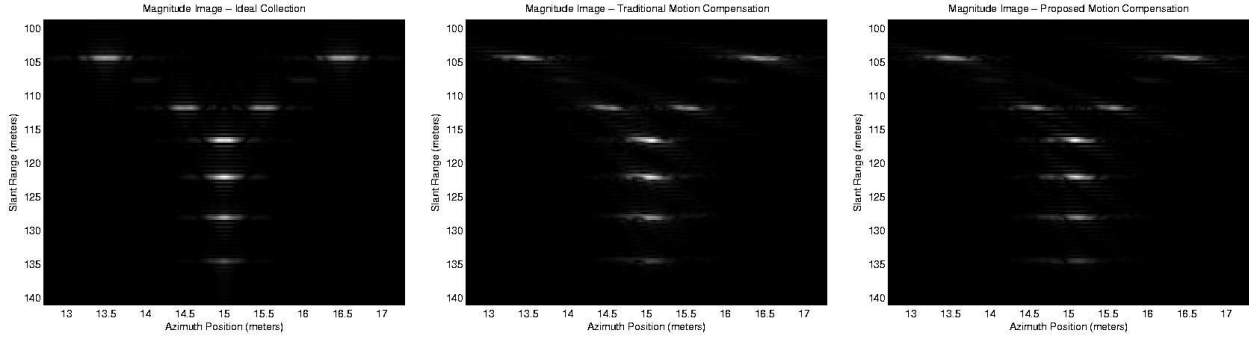
Figure A.3: A simulation of an array of point targets showing the motion compensation algorithms working on an array of point targets. The left shows an ideal collection without translational motion, the center shows the traditional motion correction algorithm, and the right shows the proposed motion correction. The non-ideal motion in this example is the same as in **Figure A.2**.
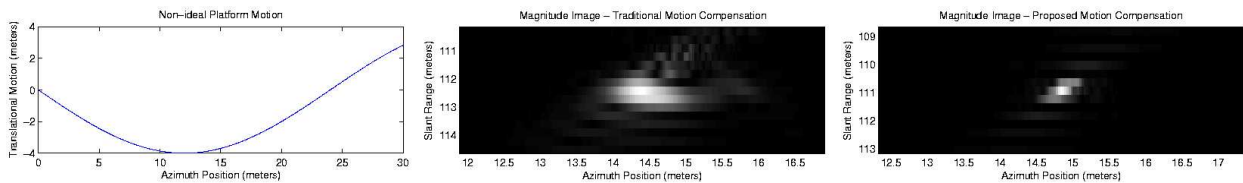

Figure A.4: Non-ideal translational motion greater than a single range bin (shown on the left) clearly demonstrates the utility of the new motion compensation algorithm as seen in this image of a point target. The center image shows the result of applying tradition motion compensation while the right image shows the proposed method.
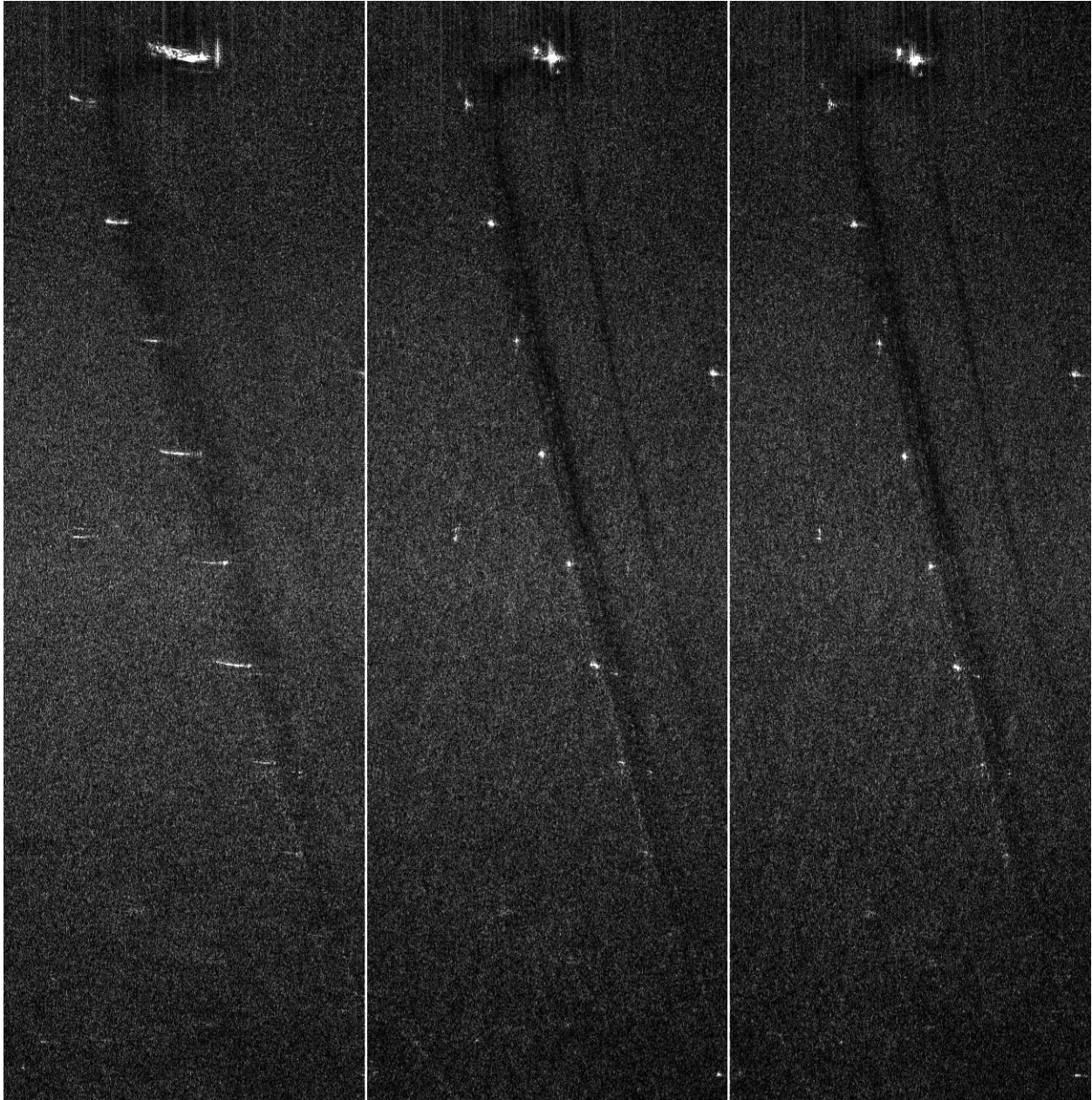
Figure A.5: Images created from NuSAR data, are presented with the results of traditional and proposed motion compensation algorithms. The leftmost image is without any motion compensation, the center image is with traditional motion compensation, and the right-side image is with the proposed motion compensation. Along a road running diagonally from the bottom right to the top left of each image are spaced a set of corner reflectors. The non-ideal motion causes the targets to smear when processed without motion compensation. Both the traditional and the proposed motion compensations methods greatly improve the focusing of the image, with the proposed method focusing the targets slightly better.

APPENDIX B.   COHERENT MULTI-FREQUENCY-BAND RESOLUTION ENHANCEMENT FOR SYNTHETIC APERTURE RADAR

Synthetic Aperture Radar (SAR) has proven useful in many applications, including reconnaissance, surveillance, mapping, change detection, and environmental studies. The use of multiple frequencies with high resolution augments the utility of SAR in each of these applications. Advances in SAR are consistently opening possibilities for more capable SAR systems, with finer resolution and multiple frequencies. Range resolution is a key performance parameter constantly being improved upon to obtain better and more useful SAR images. The resolution is dependent on the bandwidth of the radar chirp according to the equation

$$\Delta R = c / \left(2 \cdot BW \right) \tag{B.1}$$

where ΔR is the range resolution, c is the speed of light, and BW is the chirp bandwidth.

Obtaining increased bandwidth is difficult, especially at lower frequencies, due to a number of factors:

1. Many bands of the frequency spectrum are protected and SAR operation is prohibited in these bands [80].

2. Radar hardware, including power amplifiers and antennas, is designed to operate at specific frequencies, and very high bandwidth hardware is expensive.

3. Each increase in bandwidth increases the sampling and data storage requirements.

Multi-band operation offers a method to sidestep some of these issues while increasing the bandwidth, thus improving the resolution. This appendix considers an approach to coherently combine two (or more) different frequency channels into a single equivalent signal, which can be processed with slightly modified processing algorithms. Combining multiple

frequency bands to improve range resolution is not a new idea. Algorithms for stepped-frequency SAR have been in use for many years. This appendix extends the work done by Richard Lord et al. [81, 82, 83]. Many of the restrictions previously placed on combining multiple chirps are greatly relaxed in the algorithm proposed in this appendix. Notably, the requirements of overlapping bands [83], identical bandwidths, pulse widths, and chirp rates [82], and the requirement of the time shift being an integer number of samples [82] do not apply.

A system utilizing multi-band operation to provide a large bandwidth, even when traditional design limits prohibit such an arrangement, would prove extremely useful. This appendix sets forth the theory that makes such a system possible and presents a SAR system, the SlimSAR, that has been designed to be capable of demonstrating this ability.

Section B.1 presents the theory of coherent multi-band resolution enhancement, demonstrating each step with simulated SAR data. The SlimSAR is presented in Section B.2, and results from SAR data collected with a precursor system are shown in Section B.3.

B.1 The Theory of Coherent Multi-Band Resolution Enhancement

Range compression in SAR is achevied through matched filtering. A radar chirp is compressed, giving a target response with resolution measured at the 3 dB point. The resolution is determined by the bandwidth of the signal, as in Eq. B.1. This section presents a general development for how two (or more) separate, but coherent, signals spanning disjoint frequency bands, can be combined to give a resolution dependent on the sum of the bandwidths, as in Fig. B.2.

$$\Delta R_2 = c/\left(2 \cdot (BW_1 + BW_2)\right). \tag{B.2}$$

Two separate SAR signals are transmitted with center frequencies f_1 and f_2, and possibly different times, τ_1 and τ_2,

$$s_1(\tau) = w_1\left(\tau - \tau_1\right) \cdot \cos\left(2\pi f_1 \tau + \pi K_{r1}\left(\tau - \tau_1\right)^2\right), \tag{B.3}$$

$$s_2(\tau) = w_2\left(\tau - \tau_2\right) \cdot \cos\left(2\pi f_2 \tau + \pi K_{r2}\left(\tau - \tau_2\right)^2\right), \tag{B.4}$$

where τ is fast time, K_{rn} is the chirp rate for each pulse, w_n is the window that defines the chirp length, and τ_n is the delay to the transmit of each chirp. These signals are represented at the left of Fig. B.1. The goal is to shift the two signals in time and frequency, as on the right of Fig. B.1, such that when coherently combined, range compression can be performed using conventional methods, resulting in improved resolution of the target in the image.

These signals return to the radar after reflecting off a target at range R_0,

$$sr_1(\tau) = A_1 \cdot w_1 \left(\tau - \tau_1 - \frac{2R_0}{c} \right) \cdot$$
$$\cos \left(2\pi f_1 \left(\tau - \frac{2R_0}{c} \right) + \pi K_{r1} \left(\tau - \tau_1 - \frac{2R_0}{c} \right)^2 \right) \tag{B.5}$$

$$sr_2(\tau) = A_2 \cdot w_2 \left(\tau - \tau_2 - \frac{2R_0}{c} \right) \cdot$$
$$\cos \left(2\pi f_2 \left(\tau - \frac{2R_0}{c} \right) + \pi K_{r2} \left(\tau - \tau_2 - \frac{2R_0}{c} \right)^2 \right) \tag{B.6}$$

where A_n is the signal amplitude, which may vary for different frequency bands.

The signals are quadrature-demodulated by $\cos \left(2\pi f_n \tau \right)$ yielding the phases

$$\phi_1(\tau) = \frac{-4\pi f_1 R(\eta)}{c} + \pi K_{r1} \left[\tau - \tau_1 - \frac{2R(\eta)}{c} \right]^2 \quad , \tag{B.7}$$

$$\phi_2(\tau) = \frac{-4\pi f_2 R(\eta)}{c} + \pi K_{r2} \left[\tau - \tau_2 - \frac{2R(\eta)}{c} \right]^2 \quad , \tag{B.8}$$

where $R(\eta)$ is the range to target which changes with slow time η.

We take the range Fourier transform of each signal individually. This is done using the principle of stationary phase (POSP) in performing the Fourier integration, computed by subtracting $2\pi f_\tau \tau$ from Eq. (B.7) (where f_τ is range frequency),

$$\phi_{0r} = \frac{-4\pi f_1 R(\eta)}{c} + \pi K_{r1} \left[\tau - \tau_1 - \frac{2R(\eta)}{c} \right]^2 - 2\pi f_\tau \tau. \tag{B.9}$$

We then take the derivative with respect to τ

$$\frac{d\phi_{0r}}{d\tau} = 2\pi K_{r1} \left[\tau - \tau_1 - \frac{2R(\eta)}{c} \right] - 2\pi f_\tau = 0 \tag{B.10}$$

and solve for τ,

$$\tau = \tau_1 + \frac{f_\tau}{K_r} + \frac{2R(\eta)}{c}. \tag{B.11}$$

Substitute into Eq. (B.9) and simplify to obtain the signal after the range Fourier transform of the signal,

$$
\begin{aligned}
\phi_{1R} &= \frac{-4\pi f_1 R(\eta)}{c} + \frac{\pi f_\tau^2}{K_{r1}} - 2\pi f_\tau \left(\tau_1 + \frac{2R(\eta)}{c} + \frac{f_\tau}{K_{r1}} \right) \\
&= \frac{-4\pi f_1 R(\eta)}{c} - \frac{\pi f_\tau^2}{K_{r1}} + \frac{-4\pi f_\tau R(\eta)}{c} - 2\pi f_\tau \tau_1 \\
&= \frac{-4\pi (f_1 + f_\tau) R(\eta)}{c} - \frac{\pi f_\tau^2}{K_{r1}} - 2\pi f_\tau \tau_1, \tag{B.12} \\
\phi_{2R} &= \frac{-4\pi (f_2 + f_\tau) R(\eta)}{c} - \frac{\pi f_\tau^2}{K_{r2}} - 2\pi f_\tau \tau_2. \tag{B.13}
\end{aligned}
$$

The time delay difference is eliminated using a time shift, which in the frequency domain is a complex sinusoidal multiply,

$$
\begin{aligned}
H_{t1} &= e^{j2\pi f_\tau (\tau_1 + t_{p1}/2)}, \tag{B.14} \\
H_{t2} &= e^{j2\pi f_\tau (\tau_2 - t_{p2}/2)}. \tag{B.15}
\end{aligned}
$$

This leaves us with two temporally registered, standard SAR signals. In addition to the time delay, we shift each signal by half the pulse length $t_{pn}/2$ so that the zero frequency points line up after the frequency shift in the next step. If each signal is sampled at Nyquist, as in our example, we can artificially increase the fast-time sample rate by zero padding in the frequency domain.

The signals are shifted in frequency such that the bandwidths occupy non-overlapping regions of the frequency support band. This is done in the time domain, thus an inverse FFT is computed for each signal. The signals are then shifted in frequency by a complex sinusoidal multiply in the time domain, for our example this shift is

$$
\begin{aligned}
H_{f1} &= e^{-j\pi BW_1 \tau}, \tag{B.16} \\
H_{f2} &= e^{+j\pi BW_2 \tau}. \tag{B.17}
\end{aligned}
$$

The two signals are summed together into a single signal. The difficulty in processing the data now lies in the fact that the Doppler chirp used for azimuth compression is dependent on the effective mixdown frequency of each individual frequency. For our two signals, the combined azimuth chirp is the sum of the individual azimuth chirps dependent on the two effective mixdown frequencies $f_1 + BW_1$ and $f_2 - BW2$. In the Omega-K algorithm the azimuth compression is done in the two-dimensional frequency domain where the two signals have no overlap, making it easy to apply the appropriate compression to each band. Alternatively, time-domain backprojection calculates the expected phase from a given target in order to focus the image. When two signals are summed, the expected phase is calculated from the sum of the signals. These are two options available for focusing the image.

Using simulated data of two point targets, separated by 0.75 meters in slant range, the method developed in this section is tested. A comparison between images formed from a single 250 MHz bandwidth signal with a center frequency of 36 GHz, a single 500 MHz bandwidth signal at 36 GHz, and two coherently combined 250 MHz bandwidth signals at 36 GHz and 46 GHz, is shown in Fig. B.3. While the two targets are not distinguishable in the single 250 MHz bandwidth image, they are easily visible in both the 500 MHz image and the coherently combined two signal image.

This method easily lends itself to situations where the radar chirp has to skip a frequency band or when hardware constraints make large bandwidth systems impractical. Because each signal stream can be recorded separately, it sidesteps some of the sampling and storage requirements that greatly contribute to the difficultly and expense of large bandwidth systems.

B.2   The SlimSAR System

The SlimSAR (detailed in Appendix C) is a new advancement in high-performance, small, low-cost, SAR. Using a unique design methodology that extends the work from previous successful systems, such as the NuSAR-B, the flexible SlimSAR uses less power and is smaller, lighter, and more capable by use of techniques and technology developed for the MicroASAR in [49]. This compact design is facilitated by the use of a linear-frequency-modulated continuous-wave (LFM-CW) signal, which allows us to achieve a high signal-to-

noise ratio while transmitting with less power. A delayed mix-down chirp is used to sidestep the usual swath-width limitations that accompany LFM-CW operation [74].

The SlimSAR operates at multiple bandwidths. The ability to operate at L-band and two separate X-bands simultaneously makes it suitable for testing coherent multi-band resolution enhancement. The two X-bands cover frequencies just below 10 GHz and just above 10 GHz. Most targets have similar returns from both X-bands, making resolution enhancement easier. The addition of signal returns at L-band allows us to experiment with combining the returns from widely disparate frequencies, over which the targets in the scene may have quite different characteristics.

B.3   SAR Images

With multiple X-band SlimSAR data not yet available, bandwidths of disjoint frequencies are synthesized from X-band NuSAR-B data. The 500 MHz signal is decomposed into 125 MHz chunks and the outer two sub-bands (with a 250 MHz gap) are treated as separate signals. The two bandwidths are shifted and combined, as described in Section B.1, to form a single image with a bandwidth of 250 MHz. The results showing improved range resolution in the coherently combined SAR image are seen in Figs. B.6, B.4, and B.5.
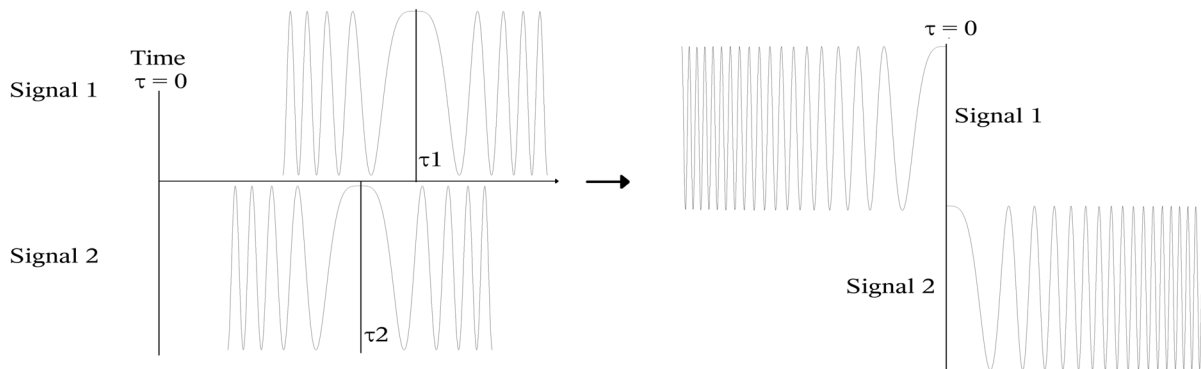

Figure B.1: Two coherent SAR pulses at different center frequencies (shown without the carrier) are transmitted at times τ_1 and τ_2 (left). In order to coherently combine the two signals to increase the total bandwidth, the signals must be shifted in time and frequency such that the timing difference is removed, the zero frequency points of the signals line up, and the signals span separate mixed-down frequency bands (right).
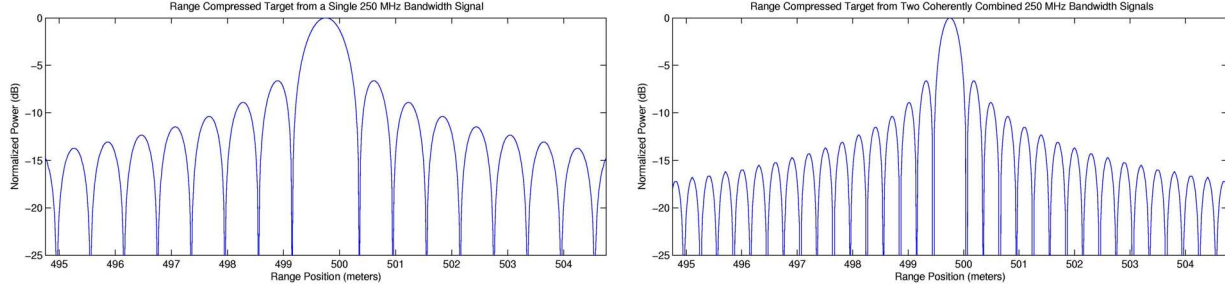
Figure B.2: A simulated point target is range-compressed with a single 250 MHz bandwidth signal (left) and two coherently combined 250 MHz bandwidth signals (right). The measured resolution of the single band image on the left is 57.15 cm while that of the double band image on the right is 28.53 cm.
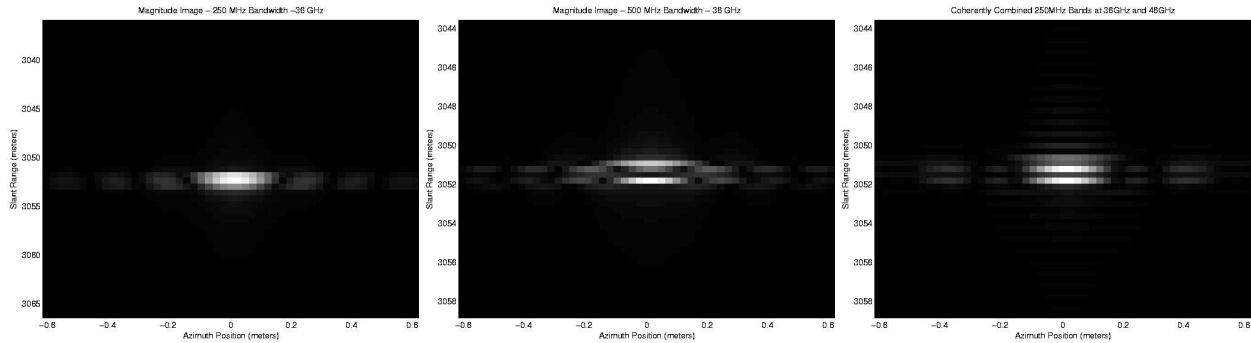

Figure B.3: Fully compressed simulated SAR images of two point targets separated by 0.75 m in slant range. The leftmost image is of single 250 MHz bandwidth data with a center frequency of 36 GHz. The resolution is 60 cm which is not sufficient to clearly separate the two targets. The center image is from single bandwidth data with a resolution of 30 cm at 36 GHz. The image at right is formed from two separate 250 MHz bandwidths, at 36 GHz and 46 GHz, which combine to give an effective bandwidth of 500 MHz. The two targets are clearly visible in the rightmost two images, showing that coherent multi-band resolution enhancement performs similarly to single band data of the same bandwidth. The data is oversampled in the azimuth direction, visually stretching the targets. The azimuth resolution is measured at 16 cm.

B.4   Summary

This appendix shows that, given certain constraints, multi-frequency-band SAR signals can be combined to improve range resolution. The signals must be coherent, though the timing between signals can be any reasonable known value where the target is temporally coherent. The resolution improvement is achieved by combining the bandwiths to form a larger single bandwidth, thus, for maximum enhancement, the frequency bands must be dis-
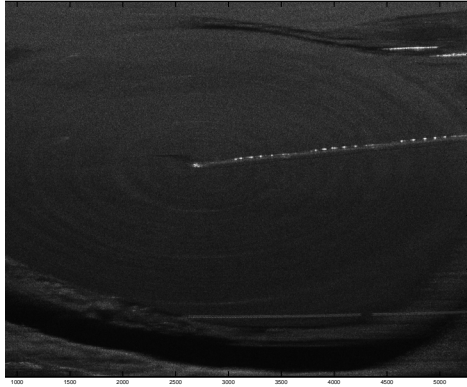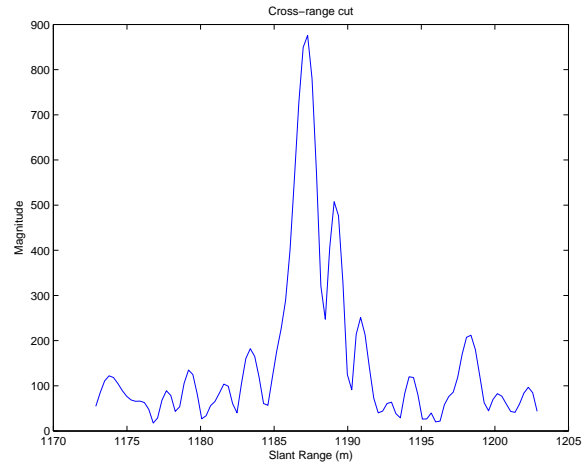
(a) Full 500 MHz (9.5-10 GHz)
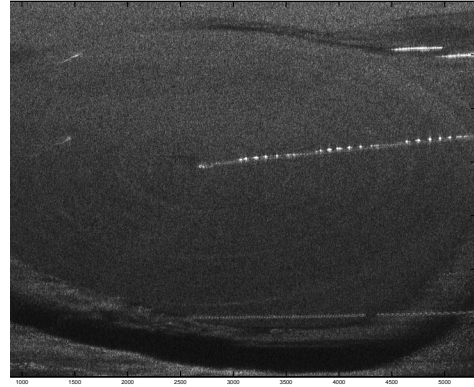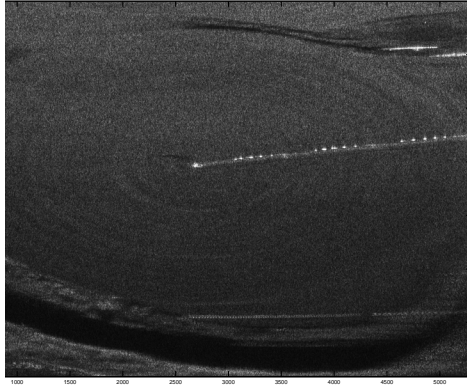

(b) 125 MHz (9.5-9.625 GHz)
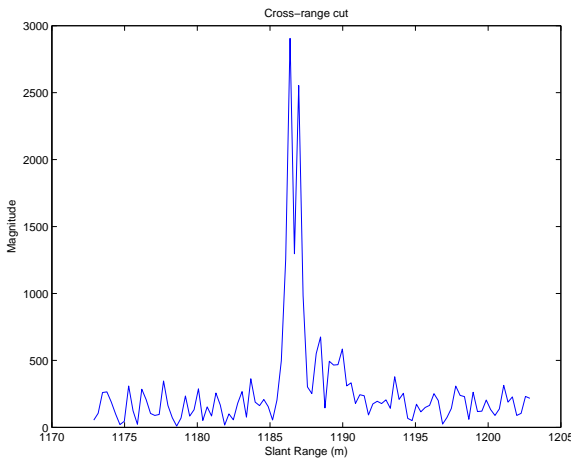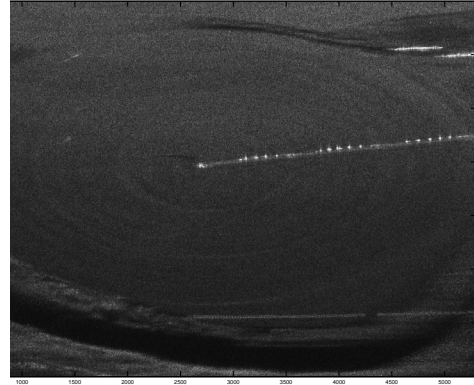

(c) Full 500 MHz (9.5-10 GHz)

(d) 125 MHz (9.5-9.625 GHz)

Figure B.4: A circular field with a rotating irrigation wheel line is shown in the top row of images. The bottom row shows a cross-range cut of the third bright point from the center of the wheel line. The first column shows the results from using the full 500 MHz signal, where (c) shows that there are actually two closely spaced point targets. In (d) we see that the range resolution is degraded such that the two targets appear as one.
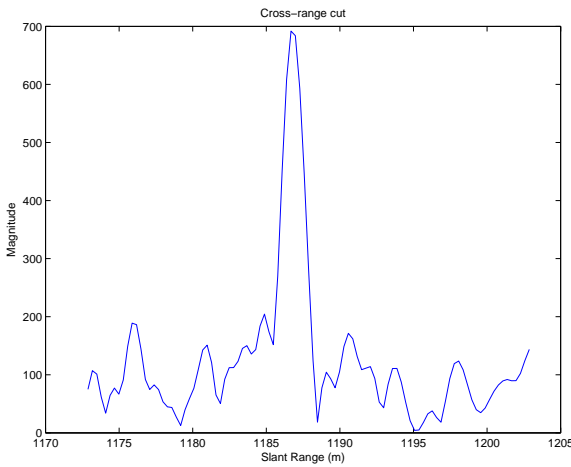
joint. It is also assumed that the target is coherent over the multiple frequency bands. This method can be used to increase the bandwidth given hardware constraints, as an alternative to common notched chirp approaches to keep-out bands, and to explore the phenomenology of combining returns at disparate frequencies.
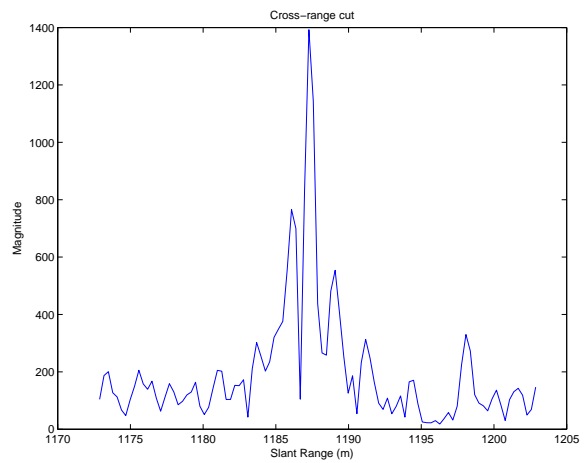
(a) 125 MHz (9.875-10 GHz)

(b) Combined 250 MHz

(c) 125 MHz (9.875-10 GHz)

(d) Combined 250 MHz

Figure B.5: A circular field with a rotating irrigation wheel line is shown in the top row of images. The bottom row shows a cross-range cut of the third bright point from the center of the wheel line. In (c) we see that the range resolution is degraded such that the two targets appear as one. The signals from B.4(d) and B.5(c) are combined using the techniques in this appendix to form the images in column (d), where we see an improvement in range resolution and we begin to differentiate between the two targets.
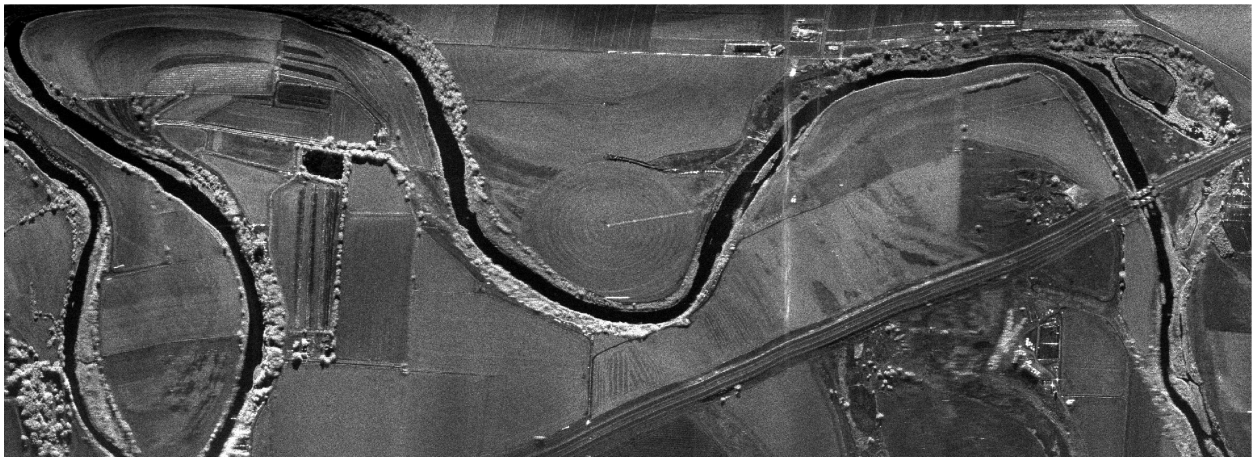
Figure B.6: A 500 MHz bandwidth NuSAR-B image of an agricultural area near Brigham City, Utah. This SAR data is separated into two data sets of 125 MHz bandwidth each, disjoint in frequency with a 250 MHz gap. These two bands are used to demonstrate the techniques set forth in this appendix. Figure B.4 focuses in on the irrigation wheel line at the center of this image.

APPENDIX C.   SAR SYSTEM DETAILS

Throughout my work as a research student at Brigham Young University, I have worked with a number of SAR systems. In this appendix, I present the basic design of each of these systems and discuss my involvement in each project and contributions to each development. The SAR systems are:

1. The BYU μSAR

2. The NuSAR

3. The MicroASAR

4. The SlimSAR

C.1   BYU microSAR

The BYU μSAR (or microSAR) meets the low power and cost requirements for flight on a UAS by employing an LFM-CW signal which maximizes the pulse length allowing the LFM-CW SAR to maintain a high SNR while transmitting with less peak power than pulsed SAR [84]. While continuously transmitting, the frequency of the transmit signal increases and decreases repeatedly at the pulse repetition frequency.

The μSAR de-chirps the received signal by mixing it with the transmitted signal. This simplifies the sampling hardware by lowering the required sampling frequency, although a higher dynamic range is needed.

A simplified block diagram of the μSAR design is shown in Fig. C.1. The BYU μSAR system is designed to minimize size and weight using a stack of custom microstrip circuit boards without any enclosure. The system measures 3"x3.4"x4" and weighs less than 2 kg including antennas and cabling. Component costs of a few thousand dollars are kept low by using off-the-shelf components as much as possible.

The UAS supplies the μSAR with either +18VDC or +12VDC. The power subsystem uses standard DC/DC converters to supply the various voltages needed in the system. Power consumption during operation is nominally 18 W, with slightly more required for initial startup. The μSAR is designed for "turn-on and forget" operation. Once powered up, the system collects data continuously for up to an hour. The data are stored on-board for post-flight analysis.

The core of the system is a 100 MHz STALO. From this single source, the frequencies for operating the system are derived, including the sample clock and the radar chirp. The LFM-CW transmit chirp is digitally created using a direct digital synthesizer (DDS)
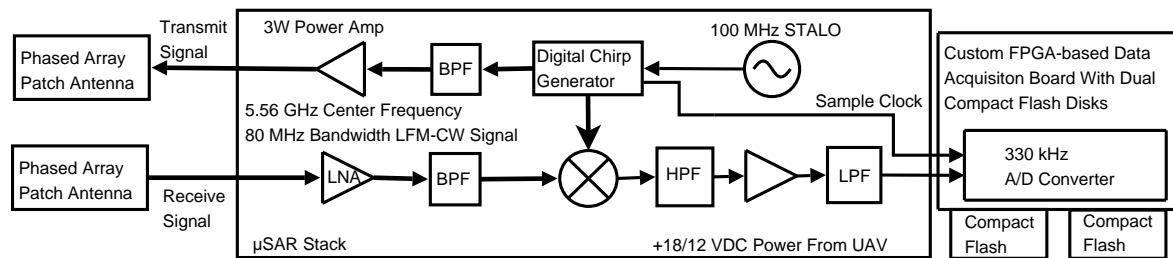

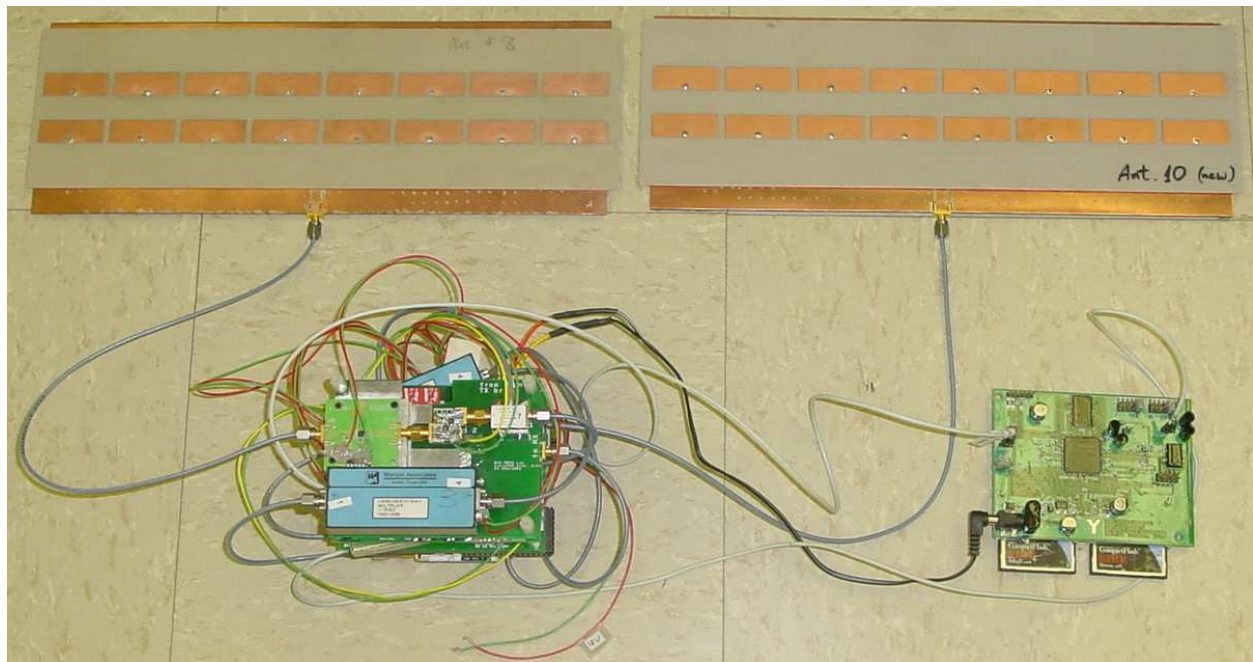Figure C.1: Simplified BYU μSAR Block Diagram.

Figure C.2: Photograph of complete BYU μSAR system ready for flight on a small UAS.

which is controlled by a programmable IC microcontroller. Switches control the PRF settings, allowing it to be varied (128-2886 Hz) for flying at different heights and speeds. The programmable DDS also generates the sample clock coherent with the LFM signal.

The μSAR signal is transmitted with a power of 28 dBmW at a center frequency of 5.56 GHz or 1.72 GHz and a bandwidth of 80-160 MHz. The range resolution of an LFM chirp is inversely proportional to the bandwidth of the chirp, thus the μSAR has a range resolution of 1.875 meters at 80 MHz, and 0.9375 meters at 160 MHz.

At C-band two, identical custom microstrip antennas, each consisting of a 2x8 patch array, are used in a bi-static configuration. The antennas are constructed from two printed circuit boards sandwiched together, a symmetric feed structure on the back of one board and a microstirp patch array on the front of another, with pins feeding the signal through the boards. The antennas are approximately 4"x12" and have an azimuth 3dB beamwidth of 8.8° and an elevation 3dB beamwidth of 50°. The azimuth resolution is approximately equal to half the antenna length (0.15 meters) in azimuth. Muti-look averaging is used for creating images with azimuth resolution equal to the range resolution. The L-band system uses antennas consisting of a 2x4 array of fat dipoles.

The return signal is amplified and mixed with the transmit signal. This de-chirped signal is filtered and then sampled with a 16 bit A/D at 328.947 kHz. A custom FPGA board was designed to sample the signal and store the data on a pair of 1GB Compact Flash disks. The data is collected continuously at a rate of 0.63 MB/second and either stored on-board or transmitted to a ground station.

Data processing for the BYU μSAR [85] follows methods detailed in Chapters 4 and 5 in this dissertation. Examples of μSAR imagery can be found in Fig. C.3.

For some flights, the Systron Donner Inertial MMQ-G INS/GPS unit is used with the BYU μSAR because of its small size (9.4 in^3) and weight (< 0.5 lbs). It provides position and attitude solutions at a rate of 10 Hz. The solution messages are transmitted to the μSAR using RS-232 and stored with the SAR data.

I began working on the μSAR project after the designs were complete and a prototype was functioning. I completed the assembly of numerous additional units including a new digital board for recording the data. I also built a second receive channel and conducted
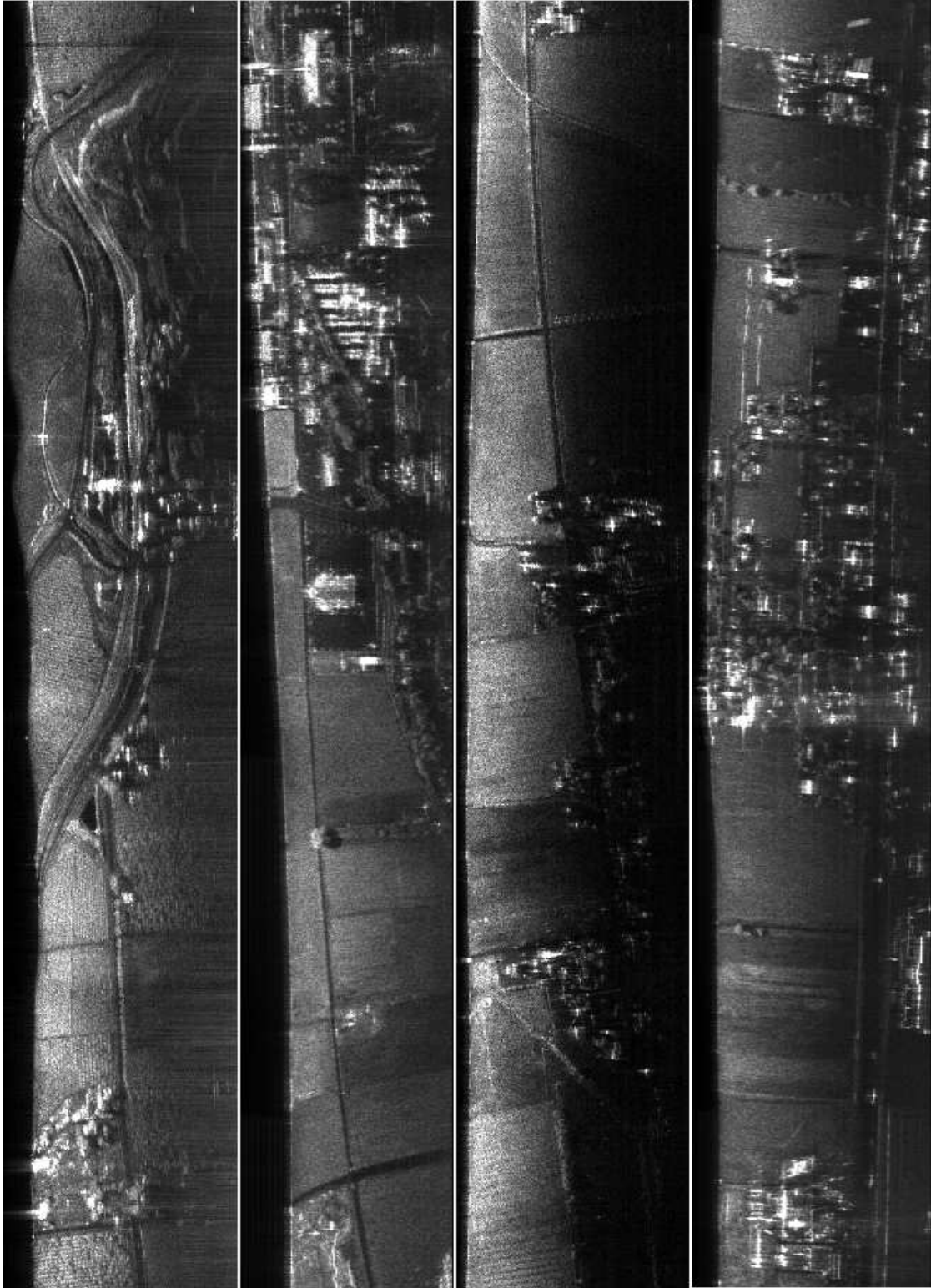
Figure C.3: Example C-band μSAR imagery showing agricultural, industrial, and residential areas.

interferometric experiments, including developing the processing software. I redesigned the μSAR to work at L-band, and the C-band version to work with a bandwidth up to 160 MHz, and oversaw the assembly and testing of these new designs. The μSAR has flown experimentally on a number of manned and unmanned aircraft and has imaged areas of Utah, Idaho, Alaska, Australia, and New Foundland.

C.2   The NuSAR

The Naval Research Laboratory (NRL) Unmanned Aircraft System (UAS) SAR (NuSAR) was developed as part of NRL's DUSTER (Deployable UAV System for Targeting, Exploitation, and Reconnaissance) program in a team effort with BYU, ARTEMIS, Inc., Space Dynamics Laboratory (SDL), and NRL [72]. The NuSAR is a small, multi-frequency, low-power, pulsed SAR system designed for UAS flight. It operates with a variable bandwidth of 500 MHz maximum (resulting in a resolution as fine as 30 cm), a peak transmit power of 25 W, and is designed to operate at 2500-6000 ft above ground level (AGL). The system has a VME form factor, with slices that include the digital signal generation and data sampling, the core L-band RF (see Fig. C.4), and a block up/down converter which extends operation to other frequency bands (the system is currently outfitted with an X-band block converter). BYU has a version known as the NuSAR-B.

My contributions to the NuSAR project include processing software development (including theoretical developments) and hardware testing and troubleshooting. I programed processing code in C++ implementing the RDA, the CSA, and the ωKA. I also implemented a MATLAB version of the backprojection algorithm. The NuSAR has been used by SDL and NRL to demonstrate SAR capabilities in detecting military targets of interest. The NuSAR-B has been used for some interferometry experiments for BYU. An example NuSAR-B image is found in Fig. B.6.

C.3   The MicroASAR

The MicroASAR is based on licensed BYU μSAR [45] technology. It is professionally built by ARTEMIS, Inc., making it a much more robust and flexible system [49, 86]. The
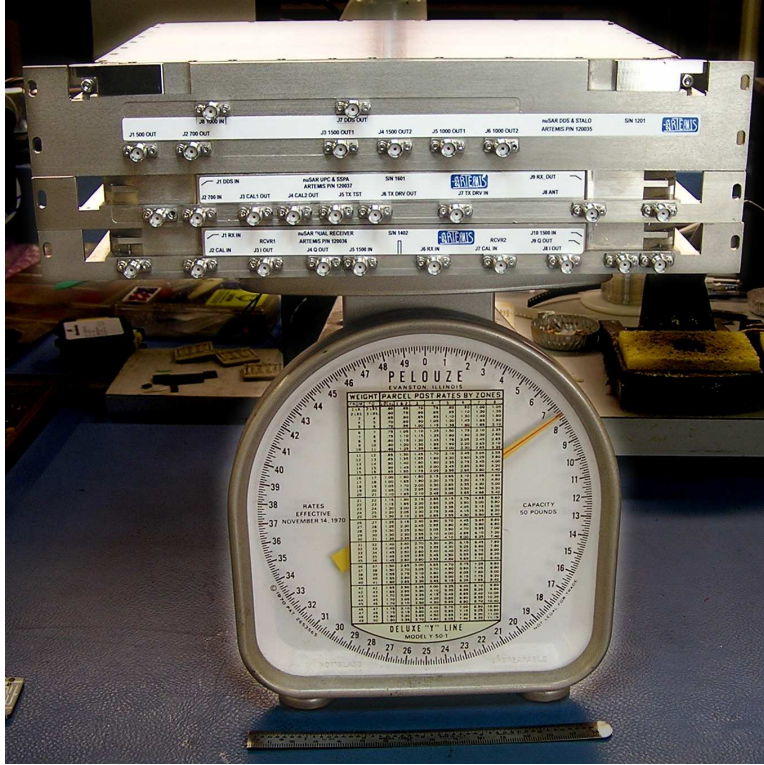
Figure C.4: Photograph of the NuSAR hardware including, from top to bottom, the STALO and DDS, the L-band RF hardware and SSPA, and the dual channel L-band receiver.

Figure C.5: Photograph of the *Surf Angel* test aircraft

MicroASAR is a complete, self-contained SAR system that has been designed specifically to be small and lightweight while still being robust and capable. These characteristics make it an ideal SAR system for use on unmanned aircraft systems (UAS) and other small aircraft.

Rather than transmitting pulses, the MicroASAR is a continuous wave (CW) SAR system [49, 86]. A CW system is constantly transmitting and receiving and is thus capable of maintaining a high SNR while transmitting much less peak power than a comparable pulsed system. The MicroASAR transmits at 1 W and operates at altitudes 1000-3000 ft AGL. It operates at C-band with a variable bandwidth up to 200 MHz. An analog de-chirp on receive reduces the sampling requirements to keep the data rate low.

For the MicroASAR project I advised on the system design, developed backprojection processing software, and worked with NASA for deploying the MicroASAR on a small UAS over the Arctic Ocean. The MicroASAR has been flown onboard the *Surf Angel* (see Fig. C.5) and the NASA SIERRA UAS. It has imaged areas of Utah, Washington, Nevada, California, Svalbard, and the Arctic Ocean. Imaging arctic sea ice from onboard the SIERRA was a significant accomplishment. This mission is further described in Section C.3.2. Example MicroASAR imagery can be found in Figs. C.7, C.8, and C.11.

C.3.1 MicroASAR Design

The MicroASAR uses a linear frequency-modulated continuous-wave (LFM-CW) chirp generated by a direct digital synthesizer (DDS) chip. By maximizing the pulse length, an LFM-CW system is able to maintain a high SNR while transmitting with a lower peak power than a comparable pulsed SAR. The return signal is mixed with a copy of the transmitted signal giving the difference in frequency. The frequency difference corresponds directly to the slant-range to a target.

The CW scheme does have the side effect of limiting the swath width that can be imaged by the sensor, and thus the altitude at which the aircraft can fly. Since the MicroASAR is designed for small, low-flying aircraft, this is not a severe restriction.

Because a CW SAR system is constantly transmitting, a bistatic configuration with a separate antenna for the receive channel is used to maximize transmit-receive isolation. An undesirable side effect of bistatic, LFM-CW SAR is feedthrough between the transmit and receive antennas. This relatively strong feedthrough component dominates the low end of the dechirped spectrum and must be removed before final processing. In the MicroASAR
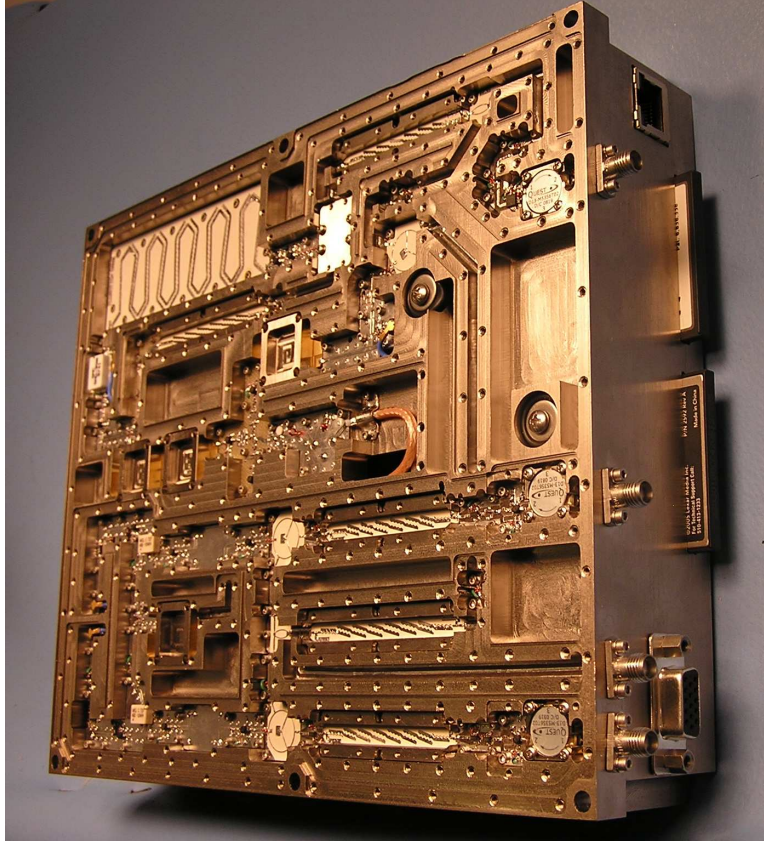
Figure C.6: Photograph of the MicroASAR hardware

this is done in hardware with the help of a bandpass filter with high out of band rejection, as described in [49].

A summary of the MicroASAR specifications can be found in Table C.1.

C.3.2 Imaging from the SIERRA

The NASA SIERRA (Sensor Integrated Environmental Remote Research Aircraft) UAS [87] is a medium class, medium duration aircraft designed by the Navel Research Laboratory to test new instruments and support NASA earth science flight experiments. Its value is apparent when long duration flights are conducted in remote, harsh environments which are too dangerous for pilots and manned aircraft. With capacity to carry multiple payloads, efficient mission planning software, and in-flight programmable autopilot, the SIERRA is suitable for a variety of missions, and is an ideal platform for the MicroASAR.

Table C.1: **MicroASAR System Specifications**

Physical Specifications	
Transmit Power	30 dBm
Supply Power	< 35 W
Supply Voltage	+15 to +26 VDC
Dimensions	22.1x18.5x4.6 cm
Weight	2.5 kg
Radar Parameters	
Modulation Type	LFM-CW
Operating Frequency Band	C-band
Transmit Center Frequency	5428.76 MHz
Signal Bandwidth	80-200 MHz (variable)
PRF	7-14 kHz (variable)
Radar Operating Specifications	
Theoretical Resolution	0.75 m (@ 200 MHz BW)
Operating Altitude	500-3000 ft
Max. Swath Width	300-2500 m (alt. dependent)
Operating Velocity	10-150 m/s
Collection Time (for 10GB)	30-60 min (PRF dependent)
Antennas (2 required)	
Type	2 x 8 Patch Array
Gain	15.5 dB
Beamwidth	8.5°x50°
Size	35x12x0.25 cm

The Characterization of Arctic Sea Ice Experiment 2009 (CASIE-09) uses a variety of remote sensing methods, including satellite observations and UAS, to provide insights into ice roughness on the scale of meters to tens of meters. The mission also offers a testbed to demonstrate the value of UAS for long-range, long-duration remote sensing science. Five science flights covering 2923 km of sea ice were flown in July 2009.

For the CASIE mission, the SIERRA payload consisted of

- Laser altimeter/surface height profiler (non-scanning) system consisting of two lasers acquiring simultaneous but laterally offset laser tracks, GPS, inertial measurement unit, and payload computer.

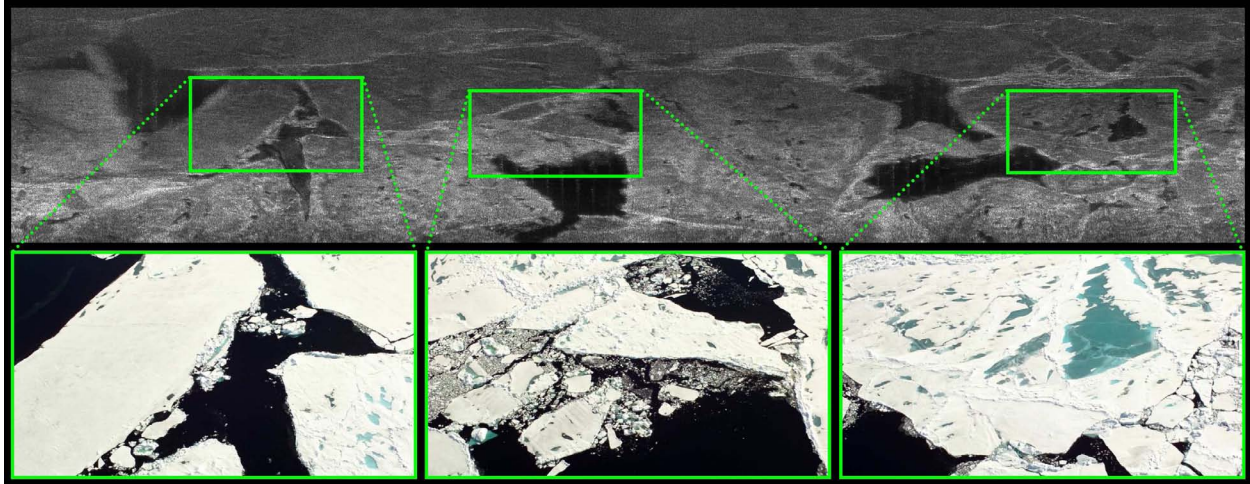- Imaging synthetic aperture radar (the MicroASAR) with video camera.

Figure C.7: A series of images collected during the CASIE mission showing agreement between the MicroASAR sensor (top) and the on board video camera (bottom).

- Three digital cameras.

- Up-looking and down-looking broadband shortwave radiation pyranometers.

- Up-looking and down-looking shortwave spectrometers.

- Down-looking temperature sensors (pyrometers).

- Temperature/Rh Sensors

For CASIE, the SIERRA flew out of Ny-Alesund, Svalbard, a location which provides access to ice with a range of thicknesses, age, and ridging characteristics. The SIERRA typically flew to the north and northwest, passing over open ocean and marginal sea ice to target thick, old ice within the Fram Strait ice outflow region. The flight patterns over the target area involved closely spaced, adjacent flight tracks to provide mapping coverage with the MicroASAR and the other sensors. Examples of images from CASIE can be found in Figs. C.7 and C.8.

C.4 The SlimSAR

The SlimSAR is a new advancement in high-performance, small, low-cost, SAR, suitable for operation on small UAS. This multi-frequency SAR was designed by exploiting the
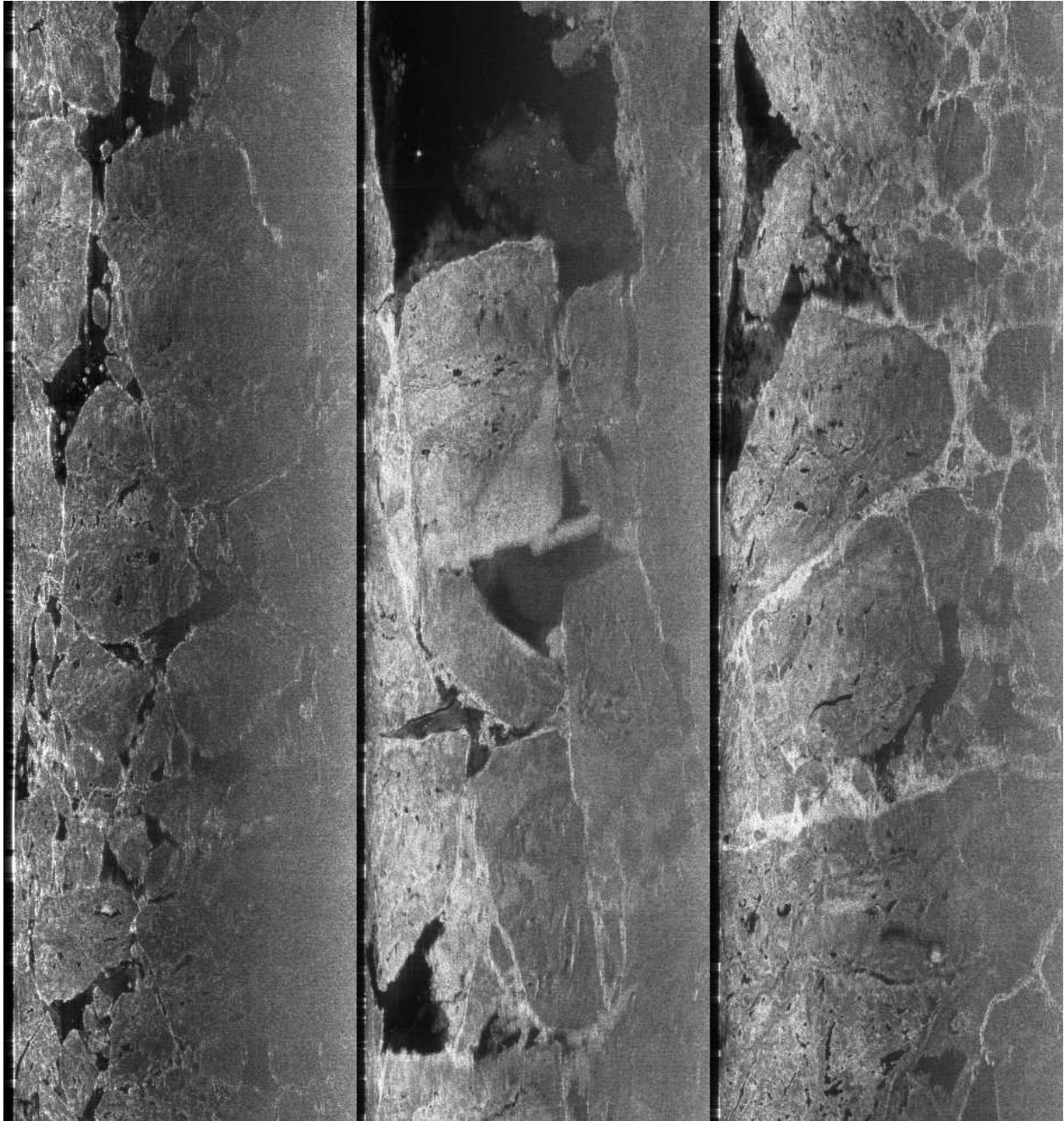
Figure C.8: A series of MicroASAR images collected during the CASIE mission. The imagery is displayed in slant-range which results in a geometric distortion of the image especially noticeable near nadir (the left side of the image). Visible in the images are common sea ice formations including rafting and ridging.

techniques and technologies developed for previous systems, resulting in increased capability and flexibility, all in a small package [54]. The SlimSAR is being developed by ARTEMIS,

Inc. For this project, I have contributed with system design, hardware testing, and processing software development.

C.4.1 System Design Methodology

The SlimSAR was designed using an innovative methodology [54, 86]. The goal is to find the quickest path from system requirements specification to deployment of a successful solution. The SlimSAR design is based on the tested SAR systems, the MicroASAR and NuSAR. The existing designs were exploited to keep much of the design heritage while best meeting the requirements for the SlimSAR system. The risks associated with new, untested technologies are thus minimized.

Basing the design on an existing SAR system provided benefits for the integration and system testing process. The MicroASAR has been operating during the SlimSAR development period on the *Surf Angel*. Using the MicroASAR data from these flights, the data collection, handling, and processing methods were refined then used with very little modification for SlimSAR. The system was therefore ready for initial flight testing as soon as the hardware was completed. Immediate flight testing on the test bed aircraft reveals necessary changes in the SAR system, the processing algorithms, and other supporting systems.

For the SlimSAR, the preliminary design was done in October 2008 with the first test flight of the L-band hardware conducted the week of June 15, 2009. Over the next couple of weeks the system was refined in a very quick loop, with feedback from test flights prompting changes in hardware and software with immediate flight testing to verify the improved operation and provide feedback for further improvement.

C.4.2 The System Design of the SlimSAR

The SlimSAR is designed as a compact pod-mount unit consisting of the radar, a motion measurement system, GPS, miniature data link, conformal wide-beam L-band antenna and a gimbaled X-band antenna. This entire system weighs less than 20 lbs and consumes less than 150 Watts.
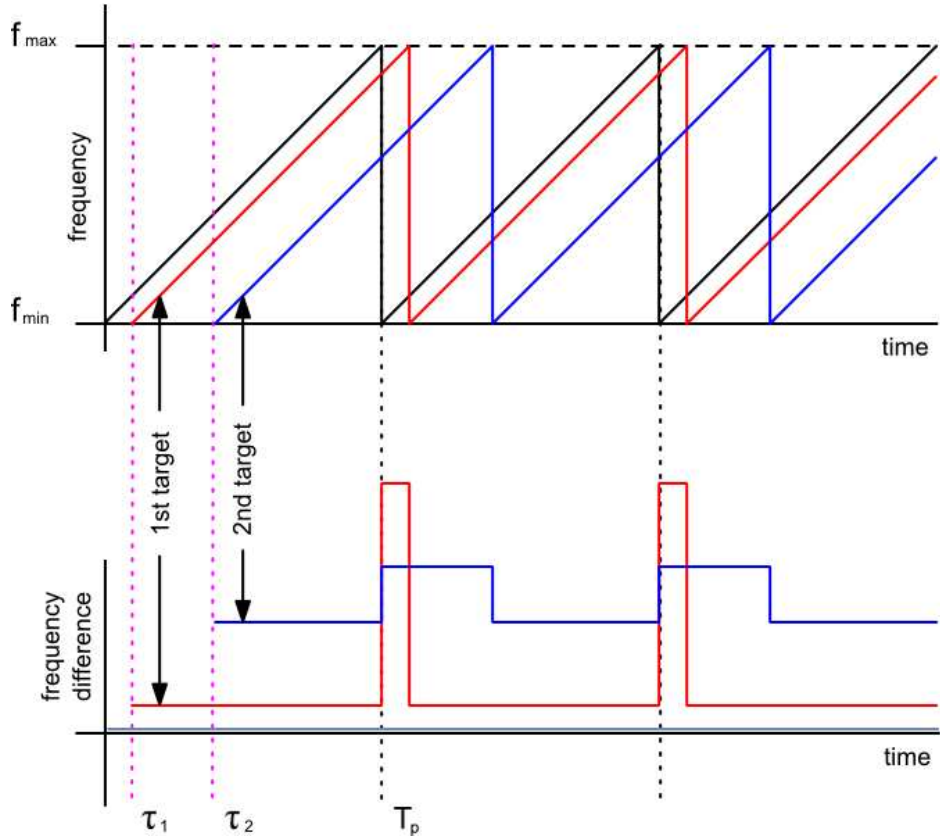
Figure C.9: A line diagram showing the idealized (exaggerated) spectrogram of the received signal before (top) and after (bottom) de-chirping. Note that a delay in time translates directly to a difference in frequency.

LFM-CW SAR Signal

The use of a linear frequency-modulated continuous-wave (LFM-CW) signal facilitates compact design, allowing us to achieve a high signal-to-noise ratio while transmitting with less peak power. For LFM-CW SAR, the received signal is mixed with the transmit signal, resulting the difference between the signal frequencies. This is illustrated in Figure C.9. Near range targets have a lower frequency than far range targets. The bandwidth of this signal is much less than the transmit signal bandwidth, thus the digital sampling requirements are relaxed.

Transmitting with less power and sampling the data at a slower rate can be done with hardware that is smaller, lighter, and consumes less power than traditional pulsed systems.

The disadvantages are that the transmit and receive channels require separate antennas and feed-through between the antennas must be controlled.

Delayed Mix-Down Chirp

The system has two direct digital synthesizers (DDS) which generate identical SAR signals, with one delayed by the time of flight to the closest range of the desired imaging area. When the received signal is mixed with this second chirp, the bandwidth is reduced, lowering our sampling requirements.

In LFM-CW SAR, the swath width is usually very limited, but with our delayed mixdown chirp we can increase the width of the imaged area. This swath width is constrained by a number of inter-related factors:

1. The width of the intermediate frequency filter

2. The chirp rate and chirp bandwidth

3. The pulse-repetition frequency and antenna beamwidth

4. The platform altitude (AGL)

5. The maximum data rate

6. The mix-down chirp delay

Overall System Design Walk-Through

The core of the system is the L-band portion. An FPGA controls the variable system parameters making sure the DDS's, the ADC, and the data storage are all working together. The DDS's generate the SAR signals which are up-converted to L-band (at different frequencies). The signal is either transmitted through the L-band antenna or up-converted to X-band in the X-band block converter, amplified, and transmitted through the X-band antenna.
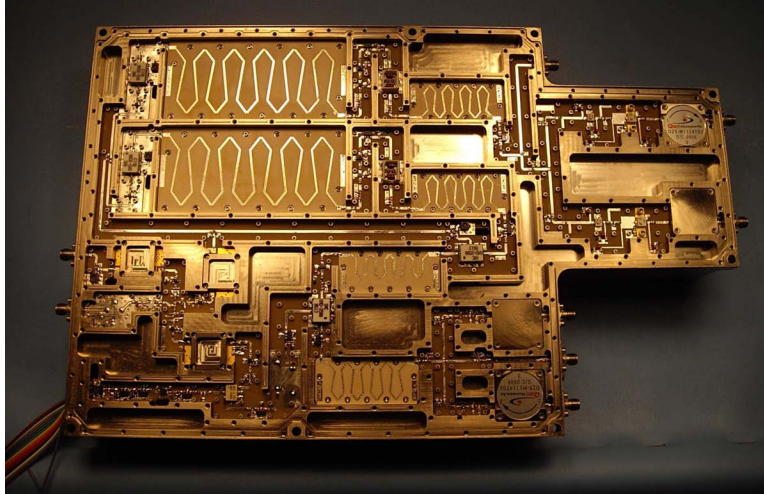
Figure C.10: Photograph of SlimSAR hardware

The receive signal is amplified, and in the case of the X-band signal, down-converted to L-band. The signal is mixed with the delayed second chirp, offset in frequency, which de-chirps the signal at an intermediate frequency. A SAW band-pass filter with large out-of-band rejection removes the antenna feed-through and signal returns from outside the target area. The reduced bandwidth signal is mixed-down and digitized. The digital signal is streamed via Ethernet to on-board storage, the tactical data-link, and/or and on-board processor. Range-Doppler, frequency-scaling, and backprojection algorithms have been developed for processing the data. The backprojection algorithm allows for non-linear flight paths (i.e. circular).

System specifications

The SlimSAR is designed to support a contiguous signal bandwidth of up to 660 MHz. Because the spectrum at L-band is very heavily utilized, however, the bandwidth and center frequency can be modified to accommodate restrictions in this band. For example, a configuration that we have FCC permission to use has a center frequency of 1257.5 MHz with an 85 MHz bandwidth. The L-band transmitter is capable of alternating pulses between horizontal and vertical polarization for polarimetric operation.

The X-band up/down converter translates the 660 MHz L-band signal up to two separate sub-bands, one just below 10 GHz, the other just above. These two sub-bands are

operated simultaneously by alternating each transmitted pulse between the two. The resulting data can be combined through coherent multi-band processing techniques to increase the resolution of the final image.

The built in solid-state power amplifier is designed to output 4 Watts continuous peak power. This power level is sufficient for the current targeted operational altitude of 5000-8000 feet above ground level (AGL). It is possible to add an external power amplifier in order to obtain a better SNR at higher altitudes.

Supporting subcomponents

There are several important subsystems which support the generation and exploitation of high-quality SAR imagery. The SlimSAR includes a motion measurement system, and a gimbaled X-band antenna. It also includes a gigabit Ethernet interface which allows for the integration of a tactical data-link for transferring the raw data to a ground station where it can be processed in near real time.

The motion measurement subsystem includes high-precision GPS and inertial measurement unit (IMU). In order to obtain high-precision inertial measurements while minimizing the necessary payload weight, 3-axis accelerometers and fiber-optic gyroscopes are integrated into the SlimSAR enclosure. This arrangement eliminates the need for an extra enclosure while enabling tight correlation of the motion data and SAR data. Additionally, the X-band antennas require an adaptive positioning system because they have a very narrow beamwidth. Data from the GPS/IMU system is fed in real time to a two-axis gimbal which controls the elevation and azimuth pointing angles of the antennas. The system thus keeps the antennas pointing perpendicular to the flight path even when the aircraft may be flying at an angle to account for wind or turbulence. The gimbal allows the X-band antennas to rotate 270°, allowing for the use of SlimSAR in spotlight mode and ground moving target indicator (GMTI) mode.

C.4.3 System Performance Trade-offs and Flexibility

Every radar system has inherent performance tradeoffs, and SlimSAR is no exception. The unique design of the SlimSAR, however, makes it very flexible. By simply adjusting some of its operational parameters, the SlimSAR can be made to operate in a wide variety of imaging situations.

The width of the intermediate frequency filter

As explained in Section C.4.2, the received signal in the SlimSAR is mixed with a copy of the transmitted signal. Through this process, time-of-flight delays are translated directly to single frequencies in the spectrum of the resulting signal. The procedure is generally referred to as de-ramping or de-chirping of the received signal because the frequency modulated chirps are converted to single tones. When a transmitted pulse scatters off a target at range R it returns to the receiver after a time-of-flight delay of $\tau = 2R/c_0$. A target at this range is represented in the dechirped signal as the single frequency

$$\Delta f = k_r \tau \tag{C.1}$$

where k_r is the chirp rate of the transmitted signal. The chirp rate is defined in terms of the signal bandwidth B_T and the pulse length t_p as $k_r = B_T/t_p$. In the special case of CW SAR, the pulse length is equal to the pulse repetition interval (PRI) so that the chirp rate is directly proportional to the inverse of the PRI, which is the pulse repetition frequency (PRF). The chirp rate is therefore rewritten as $k_r = B_T f_p$ where f_p is the PRF.

The SlimSAR adds an additional wrinkle to this relationship by allowing an arbitrary delay between the beginning of the transmitted signal and the beginning of the signal which is mixed with the received signal during the dechirp process. Eq. (C.1) is rewritten to account for this delay as

$$\Delta f = k_r \left(\tau - d \right). \tag{C.2}$$

The bandpass filter employed in the receiver's IF chain after the dechirp mixer selects a range of frequencies in the dechirped signal and thus effectively functions as a range-gate.

Time-domain range-gating is not possible because the radar must be constantly transmitting and receiving. The range-gate function is therefore performed in the frequency domain after the dechirp process.

In order to calculate the IF filter's effect on the width of the imaged swath, we must define the width of the filter. We assume that signals which fall outside of the 3 dB bandwidth of the filter's passband are suppressed. It is also necessary to know the point in the dechirped spectrum to which signals with a zero time-of-flight delay are mapped to. A target with zero time-of-flight delay is equivalent to feeding the transmitted signal directly into the receiver. In other words, we must know the frequency in the spectrum which corresponds to $\tau = 0$ and $d = 0$. This frequency is either DC for a baseband de-chirping scheme, or it is equal to the IF used in the de-chirping process. The difference between the zero time-of-flight frequency and the upper 3 dB point of the filter's passband is defined as Δf_{max}) and the difference between the zero time-of-flight frequency and the lower 3 dB point of the filter's passband, if any, is defined as Δf_{min}.

With these definitions in place, a simple rewriting of Eq. (C.2) gives an expression for maximum time-of-flight delay that is present in the filtered signal,

$$\tau_{max} = \frac{\Delta f_{max}}{k_r} + d. \tag{C.3}$$

Replacing Δf_{max} with Δf_{min} results in the minimum time-of-flight delay present in the filtered signal. These results are then converted to slant-range using the relation $R = c_0 \tau / 2$. The IF filter, therefore, directly affects the width of the imageable swath for an LFM-CW system such as the SlimSAR. The swath width is also affected by the chirp rate k_r, which is a function of the transmitted bandwidth and the PRF. The dechirp delay d does not affect the width of the swath, but rather where it physically begins and ends.

The chirp rate and chirp bandwidth

As described above, the chirp rate in an LFM-CW SAR is a function of the signal bandwidth and the PRF. The definition is reprinted here for convenience

$$k_r = B_T f_p. \tag{C.4}$$

The bandwidth of the transmitted signal is generally made to be as wide as possible because the resolution of the final image is inversely proportional to this value. Thus the chirp rate is modified mainly by changing the PRF at which the radar operates. A lower PRF results in a lower chirp rate, which in turn results in a more compact dechirped spectrum as per Eq. (C.1).

The pulse-repetition-frequency and antenna beamwidth

A SAR system relies on the Doppler shift created while moving past a target to focus in the along-track direction. The Doppler signal is sampled in the along-track by the PRF, which must therefore be high enough to properly record the entire Doppler bandwidth. The Doppler bandwidth is dependent on the velocity of the platform, v, as well as the wavelength of the transmitted signal, λ. Because the Doppler shift increases as the azimuth angle in the along-track direction is increased, the maximum Doppler bandwidth is calculated at the edges of the antenna's azimuth beamwidth, θ_a. A good approximation for the Doppler bandwidth is

$$f_D = \frac{2v\theta_a}{\lambda}. \tag{C.5}$$

Eq. (C.5) gives a lower bound on the operational PRF of the SAR system. The chirp rate and swath width can then be calculated for this lower bound.

The platform altitude (AGL) and dechirp delay

Platform altitude in a traditional pulsed SAR system is governed mainly by the system's transmit power. The radar signal must be transmitted with enough power to obtain a signal-to-noise ratio (SNR) which is sufficient to image intended targets. For an LFM-CW

system, it is also necessary to ensure that the maximum imageable slant-range, as calculated in Eq. (C.3), produces the desired swath width at the given altitude. A traditional LFM-CW SAR, in which the dechirp delay d is zero, experiences a fundamental limit on platform altitude because the dechirped spectrum has a finite bandwidth and the PRF (and thus the chirp rate) is limited by the Doppler sampling requirement. With the dechirp delay equal to zero, a typical LFM-CW SAR is forced to image the space between the platform and the ground along with the desired swath. If the platform operates too high, the entire sampled slant range may be composed of space between the platform and the ground.

SlimSAR overcomes this limitation by introducing the delay d between the beginning of the transmitted pulse and the beginning of the pulse used for dechirp mixdown. This arbitrary delay does not change the width of the imageable swath, but rather changes its location relative to the platform. Increasing the dechirp delay shifts the spectrum of the dechirped signal down. Since frequency in the dechirped signal translates directly to slant range, this means that targets at a higher slant range will fall within the passband of the IF filter. Thus the SlimSAR can be configured to image a swath of a certain width from almost any altitude simply by increasing the dechirp delay and transmit power.

The maximum data rate

The SlimSAR uses an analog dechirp process to partially compress the SAR data before sampling and storage. It is therefore only necessary to store samples at a rate which is high enough to reliably digitize the bandwidth of the dechirped signal instead of the bandwidth of the transmitted signal. Much in the same way that the data rate of a pulsed SAR can be reduced by employing a range-gate to narrow the imaged swath, the data rate of the SlimSAR may be reduced by decreasing the bandwidth of the dechirped signal and sampling at a lower rate. The same effect can be achieved by increasing the operation PRF, which stretches the dechirped spectrum, and then averaging adjacent received pulses in order to reduce the effective PRF.

The SlimSAR contains a relatively wide IF filter and samples at an offset video frequency so that filtering, downsampling, and presumming operations can be performed

digitally. This gives the device a great deal of flexibility when making the tradeoff between wide swath images and low data rate.

Example Operating Configurations

In order to illustrate the flexibility of the SlimSAR, examples of possible operating configurations are given here. The system parameters can be tailored to meet varying requirements for swath width, altitude, data rate and other constraints.

Assume the radar is operating at L-band with 185 MHz bandwidth. The L-band antennas in this case are quite small, and so have an azimuth beamwidth of 50 degrees. The platform is at 5000 ft. AGL and flying at a speed of 100 knots. Eq. (C.5) is used to calculate the minimum PRF which prevents aliasing in the Doppler domain. The dechirped spectrum is filtered to 12 MHz. Using Eqs. (C.3) and (C.4), the maximum possible swath width is calculated to be approximately 11 km in slant range. This result assumes that all 12 MHz of the dechirped spectrum is sampled at slightly more than Nyquist, which results in slightly over 24 Msamp/sec. If samples are stored with a precision of two bytes, the resulting data rate is nearly 50 Mbytes/sec.

In order to reduce the data rate, the bandwidth of the dechirped signal may be narrowed. This results in a narrower swath, which is the obvious tradeoff. A swath that is 2 km in slant range, for instance can be obtained with a data rate of close to 7 Mbytes/sec. Even lower data rates may be obtained by narrowing the Doppler bandwidth by slowing the platform, lengthening the antenna, or filtering the data after sampling. In this way, data rates significantly lower than 5 Mbytes/sec may be obtained. It is important to note that with the delayed dechirp the 2 km slant range need not extend from the aircraft toward the ground, but can be made to begin at any arbitrary point on the ground and extend for 2 km. For this reason, the SlimSAR is limited in altitude only by its transmit power and can be configured to operate at a much wider range of altitudes than a previous LFM-CW system.
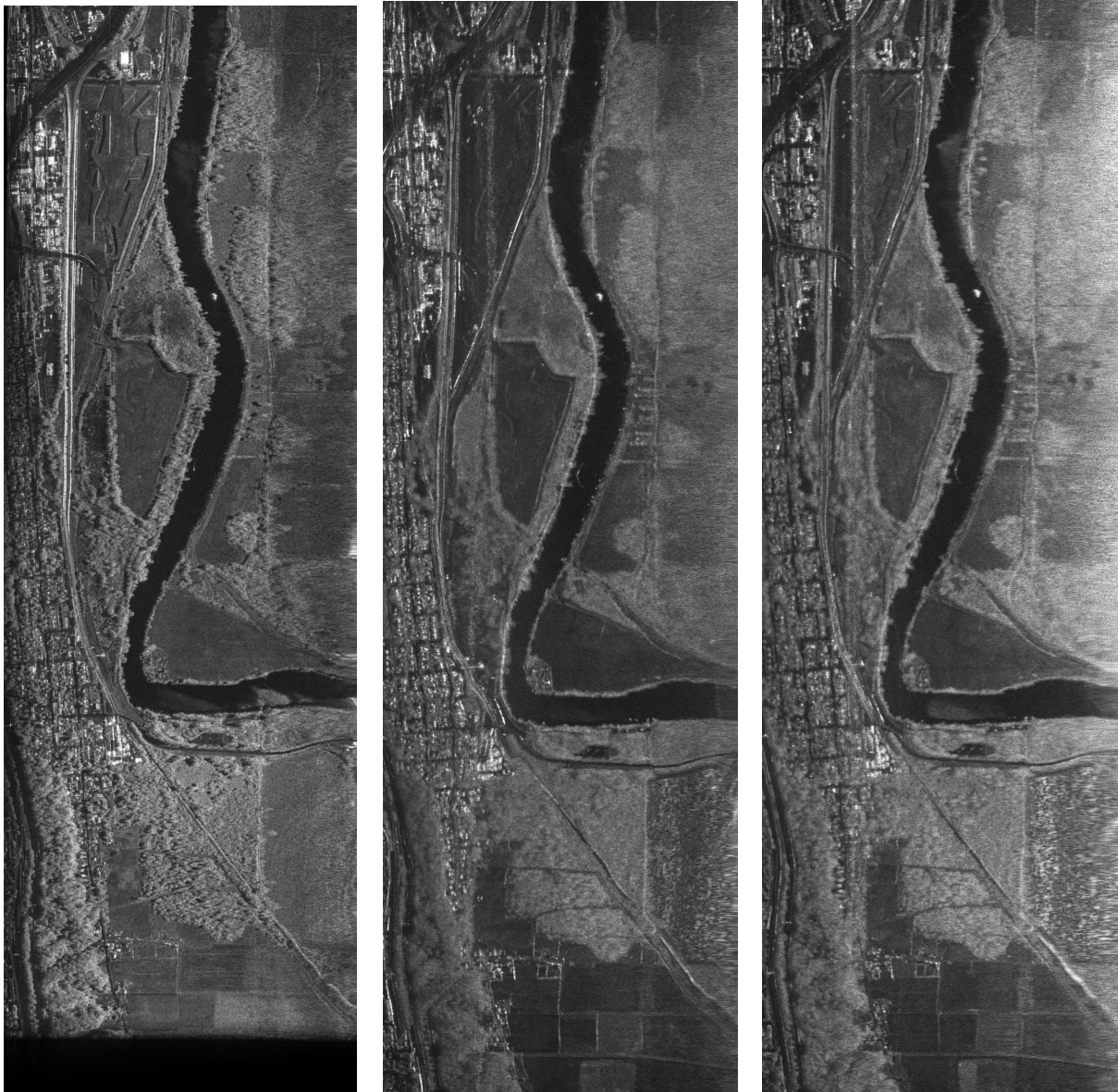
Figure C.11: Simultaneously collected SAR images of an area south of Everett, Washington, processed with the LFM-CW backprojection algorithm from Chapter 4. The leftmost image is a C-band MicroASAR image with a range resolution of 88 cm. The center image is an L-band HH-pol SlimSAR image with the rightmost being L-band VV-pol SlimSAR. The SlimSAR L-band images have a range resolution of 1.76 m, corresponding to the 85 MHz bandwidth.

C.4.4   Sample SAR Imagery

The SlimSAR has been flown in a variety of locations. This appendix includes sample imagery from the SlimSAR and the MicroASAR collected near Everett, WA (see Fig. C.11).

C.5 Summary

The stepped development of the SAR systems described in this appendix show the advantages of a strong design heritage combined with rapid testing and integration. Continued flight tests are aimed at proving and improving the SAR systems and preparing them for integration onto small unmanned aircraft. The flexible designs allow for future modifications such as alternative frequencies, higher bandwidths, and specific applications such as GMTI, interferometry, littoral and maritime modes, and polarimetry.